Reaching Kinetic Selectivities

In Pursuing Novel Ternary Oxide Coatings, and Beyond

SEBASTIAN ÖHMAN

Abstract

Öhman, S. 2023. Reaching Kinetic Selectivities. *In Pursuing Novel Ternary Oxide Coatings, and Beyond*. *Digital Comprehensive Summaries of Uppsala Dissertations from the Faculty of Science and Technology* 2242. 127 pp. Uppsala: Acta Universitatis Upsaliensis. ISBN 978-91-513-1721-2.

Kinetically driven synthesis pathways have the potential to allow new ways to develop materials and phases with much-improved properties. This particularly concerns metastable and multicomponent phases that require a selective kinetic targeting during the synthesis to circumvent the formation of thermodynamically stable products. Thin film deposition techniques, including chemical vapour deposition (CVD), can offer this selectivity. However, conventional CVD relies heavily on halide-based precursors, which are corrosive, toxic, and typically require high deposition temperatures. Moreover, the significant variations in their displayed vapour pressures, reaction routes, and reaction rates impede their chemical compatibilities, thus limiting the prospects of making novel multicomponent coatings, especially mixed-metal ones. Therefore, there is a need to find new types of precursors that may mitigate the drawbacks of halides, which also can strengthen CVD as a technique for both existing and future-emerging technologies.

In light of this, this thesis explores the simultaneous use of metal-organic precursors in synthesising and designing novel chemically vapour-deposited coatings. The ternary Al_2TiO_5 phase, renowned for its good refractory properties and low-to-negative thermal expansion, has been synthesised, which is typically challenging by other approaches. By combining aluminium and titanium isopropoxide in an in-house built CVD reactor, a selective targeting of the phase can be made that avoids stable binary phase formations. The role of local coordination in the phase formations is expressed by discovering unconventional phases in the Al–Ti–O system, such as $Al_6Ti_2O_{13}$ and $Al_{16}Ti_5O_{34}$. All coatings were amorphous as-deposited and readily crystallised at lower temperatures than those typically suggested by pseudobinary phase diagrams. *In situ* X-ray diffraction studies revealed that the crystallisation process was predominantly nucleation-controlled rather than governed by diffusion. The diminishing role of diffusion was also corroborated by subsequent studies using additional *in situ* analytical techniques, including hard X-ray photoelectron spectroscopy (HAXPES), Rutherford backscattering spectrometry (RBS), and heating in a transmission electron microscope (TEM). Combined, these techniques show that the amorphous-to-crystalline transformation occurs through a displacive (diffusionless) transformation. Based on the results, it can be inferred that short-range structural displacements by oxygen are essentially required to spur nucleation and subsequent crystallisation. Performed theoretical calculations and molecular dynamics simulations support this notion, which also highlights the potential involvement of oxygen vacancies during the crystallisation and co-formation of $Al_6Ti_2O_{13}$ and $Al_{16}Ti_5O_{34}$ beyond Al_2TiO_5.

The coherent results of this thesis emphasise situations where kinetics – rather than thermodynamics – may control the phase selection and microstructural evolution of CVD coatings. It is proposed that the findings of this doctoral work may contribute to expanding the capabilities of CVD as a technique and the rational synthesis of inorganic materials in general, especially in terms of new functional oxides.

Keywords: CVD, coatings, kinetics, crystallization, nucleation, diffusionless, Al2TiO5, oxides

Sebastian Öhman, Department of Chemistry - Ångström, Inorganic Chemistry, Box 538, Uppsala University, SE-751 21 Uppsala, Sweden.

In Memoriam of Kjell Öhman, my grandfather.

List of Papers

This thesis is based on the following papers, which are referred to in the text by their Roman numerals.

I.   Öhman, S.; Qiu, R.; Edvinsson, T.; Bäcke, O.; Törndahl, T.; Boman, M. (2021) **Selective kinetic growth and role of local coordination in forming Al$_2$TiO$_5$-based coatings at lower temperatures**. *Materials Advances*, 2(17):5737–51. Royal Society of Chemistry. DOI: 10.1039/D1MA00428J

II.   Öhman, S.; Ek, G.; Törndahl T.; Primetzhofer, D.; Boman, M. (2022) **Circumventing Thermodynamic Constraints in Nucleation-Controlled Crystallization of Al$_2$TiO$_5$-Based Chemical Vapor Deposition Coatings**. *Chemistry of Materials,* 34(11):5151–64. American Chemical Society. DOI: 10.1021/acs.chemmater.2c00615

III.   Öhman, S.; Forslund, A.; Lindblad, R.; Nagy, G.; Broqvist, P.; Berggren, E.; O.L. Johansson, F.; Törndahl, T.; Primetzhofer, D.; Boman, M. **The Role of Oxygen in Vacancy-Induced Phase Formation and Crystallization of Al$_2$TiO$_5$-Based Chemically Vapor Deposited Coatings.**
       Submitted.

IV.   Öhman, S.; Donzel-Gargand, O.; Törndahl, T.; Boman, M. **Exploring Crystallization Phenomena in Al$_2$TiO$_5$-Based Chemically Vapor Deposited Coatings by *in situ* Transmission Electron Microscopy.**
       Submitted.

Reprints were made with permission from the respective publishers.

My Contributions to the Papers

I. I constructed a CVD reactor, conceptualised and planned the study, carried out all experimental depositions and performed all analyses except for the TEM results. I wrote the main part of the manuscript and made revisions based on the co-authors' feedback.

II. I conceptualised and planned the study, carried out all experimental depositions and performed all *in situ* XRD examinations. I performed all analyses except for the data refinements. I wrote the main part of the manuscript and made revisions based on the co-authors' feedback.

III. I conceptualised, planned, and sought external collaborations for the study. I carried out all experimental depositions and took part in the analytical examinations except for the DFT calculations. I participated in all discussions and analyses regarding the results and wrote the main part of the manuscript based on feedback and input from the co-authors.

IV. I conceptualised, planned, and sought external collaborations for the study. I participated in the *in situ* TEM examinations, discussions, and analyses regarding the results. I wrote the main part of the manuscript based on feedback and input from the co-authors.

Table of Contents

Abbreviations & Acronyms

AIP	Aluminium Isopropoxide
BE	Binding Energy
BF	Bright-Field
CF	ConFlat®
CNT	Classical Nucleation Theory
CVD	Chemical Vapour Deposition
DF	Dark-Field
DFT	Density Functional Theory
EBS	Elastic Backscattering Spectrometry
EDS	Energy-Dispersive Spectroscopy
ESCA	Electron Spectroscopy for Chemical Analysis
eV	Electron Volt(s)
FFT	Fast-Fourier Transform
FIB	Focused Ion Beam
HAADF	Annular Dark-Field Imaging
HAXPES	Hard X-ray Photoelectron Spectroscopy
HRTEM	High-Resolution Transmission Electron Microscopy
IBA	Ion Beam Analyses
JMAK	Johnson–Mehl–Avrami–Kolmogorov (Equation)
MD	Molecular Dynamics
MFC	Mass flow Controller
MOCVD	Metalorganic Chemical Vapour Deposition
MSD	Mean Squared Displacement
PID	Proportional–Integral–Derivative (Controller)
PVD	Physical Vapour Deposition
RBS	Rutherford Backscattering Spectrometry
SAED	Selected area electron diffraction
Sccm	Standard Cubic Centimetres per Minute
STEM	Scanning Mode in TEM
TEM	Transmission Electron Microscopy
TIP	Titanium Isopropoxide
ToF-ERDA	Time-of-Flight Elastic Recoil Detection Analysis
T–T–T	Time-Temperature-Transformation (Diagram)
VCR	Vacuum Coupling Radiation
XPS	X-Ray Photoelectron Spectroscopy
XRD	X-Ray Diffraction

1 Introduction

The synthesis and discovery of inorganic materials have historically relied on seren-dipitous approaches involving trial-and-error methods. From a modern perspective, this is not only time-consuming but also a resource-inefficient way to discover new materials. Despite this, many such approaches remain in use today, as a rational framework encompassing the theoretical prediction, design, and synthesis of inor-ganics with desirable properties is still missing. One reason is that many synthesis methods rely heavily on thermodynamic control and equilibrium conditions, where diffusion is a common rate-limiting step. Within the free-energy landscape of possi-ble phases, this typically favours the formation of the most energetically stable prod-ucts. While explorations of such phases arguably constitute a paradigm in materials science since 1878,[1] when Gibbs first formulated the ideas of modern thermody-namics, there is an increasing need to find new ways to reach more complex phases incorporating several different elements. In other words, metastable, ternary, and multicomponent phases, which may possess superior properties compared to their thermodynamically-stable counterparts. In particular, this concerns the develop-ment of many oxides, which can show a wide range of properties not solely depend-ing on their chemical compositions but also their local short-range features.[2,3] Ac-cessing these features, however, requires an additional component not readily of-fered in many conventional synthesis methods, namely, the kinetic selectivity of the synthesis.

In light of this, significant research has been made in the past decades to develop more efficient synthesis routes for inorganic materials. Besides so-called *chimie douce* (*i.e.* "soft-chemistry") approaches,[4] this also concerns thin-film and coating deposition technologies. Using micrometre- or even nanometre-thick layers offers a vastly more resource-efficient use of elemental constituents than any bulk pro-cessing. Thin-film depositions can also bypass many of the constraints induced by slow diffusion by allowing for increased diffusion rates, decreased diffusion dis-tances, or both, in the formation of novel phases. Additionally, thin film depositions may favour situations where nucleation, a kinetic phenomenon – may control the material syntheses. For example, the concept of phase selection through nucleation

has increasingly been deemed a key component in enabling the design and rational synthesis routes for inorganics,[5,6] which is an accomplishment already reached within organic chemistry.[6–8]

Among the various deposition techniques available, chemical vapour deposition (CVD) marks a capable thin-film deposition technique wherein volatile precursors react to form coatings comprising various phases, compositions, structures, and morphologies. Hence, the great flexibility allowed by this technique readily allows one to control the structure-property relationship of the growing coating. Moreover, mixing reactants in their gaseous state, along with the fact that most CVD processes operate far from any equilibrium conditions, entails that many phases not predicted by thermodynamics can be synthesised through kinetic control.

However, CVD frequently employs halide-based precursors, which has several drawbacks in the ambition of making ternary or multicomponent coatings incorporating many mixed metals. Most strikingly, the generally low volatilities of metal halides, along with their large variations in displayed vapour pressures, reaction pathways and reaction rates, limit their chemical compatibilities. Accordingly, this restricts the possibility of finding overlapping process windows for their combined usage. Furthermore, metal halides form corrosive and toxic by-products, which may negatively impact the deposition process.

Alternatively, new types of metal-organic precursors have emerged with the potential to circumvent many of the issues found for metal halides, thereby allowing new and unexplored chemical routes to attain desirable ternary and multicomponent phases. These precursors may not only react more cleanly and at lower deposition temperatures, but they may also offer greater flexibility in their (molecular) designs and better compatibilities for their combined usage. Thus, these types of precursors carry the prospect of allowing multicomponent mixed-metal coatings to be synthesised by CVD. This general concept is examined in this thesis.

2   Scope of the Thesis & Synopsis

This thesis explores the simultaneous use of metalorganic precursors in synthesising and designing chemically vapour deposited oxide coatings. Specifically, the Al–Ti–O system has been examined to produce aluminium titanate (Al_2TiO_5) based coatings – a phase renowned for its thermal properties, including a low-to-negative thermal expansion. For this purpose, a new type of reactor has been constructed, allowing thin film depositions from various alkoxide-based precursors to be made.

Detailed examinations of the deposition process are made in **Paper I**. The results of this study emphasise that the similarities between the used precursors enable a kinetic selectivity to reach ternary phases and bypass stable binary ones. Also, the paper describes the role of local coordination in oxide-materials as part of finding unconventional ternary oxide phases, including $Al_6Ti_2O_{13}$ and $Al_{16}Ti_5O_{34}$.

The role of kinetics in the phase formations is also further examined in **Paper II**, where crystallisation of the as-deposited coatings is investigated by *in situ* X-ray diffraction. The coherent results of this study indicate that the crystallisation process is nucleation-controlled, rather than being limited by diffusion. This observation, along with the strong influence of the short-range ordering, forms the scientific incentive for the subsequent examinations made in **Papers III** and **IV**.

In **Paper III**, the combined usage of several *in situ* techniques and theoretical calculations highlights the role of oxygen in the amorphous-to-crystalline phase transformation. It is shown that the short-range migration of oxygen and its vacancies are likely responsible for the crystallisation process on an atomistic level. Furthermore, it is shown that these vacancies are likely the reason for forming the $Al_6Ti_2O_{13}$ and $Al_{16}Ti_5O_{34}$ phases.

Lastly, **Paper IV** explores the nucleation and crystallisation process through *in situ* TEM, which corroborates many of the notions and deductions made throughout the previous studies. Notably, the results of **Paper IV** also support that the crystallisation process proceeds through a diffusionless (displacive) transformation route.

In essence, this thesis provides new fundamental understandings about nucleation and crystallisation phenomena occurring in oxide-based materials. It is illustrated that the combined usage of CVD and a subsequent annealing step may allow the formation of ternary – and possibly multicomponent – phases at lower temperatures than predicted from available phase diagrams. The favourable kinetics induced by the gaseous mixing of precursors, along with their similar reaction routes, may also enable the synthesis of oxide phases with significantly shorter processing times than comparable synthesis routes.

In addition, the results of this thesis highlight situations where nucleation – rather than diffusion – may control the phase selection and microstructural evolution during the annealing and crystallisation of CVD coatings. Consequently, the findings presented herein may contribute to expanding the capabilities of CVD as a technique and the possibilities for the rational synthesis of inorganic materials in general, particularly in terms of oxides.

3 The Al–Ti–O System

3.1 General Features

The Al–Ti–O system has high technological and industrial importance; therefore, several experimental and thermodynamic evaluations have been made to determine its constituting phases and their properties.[9–11] Most commonly, the system is thermodynamically represented based on its most stable binary constituents, Al_2O_3 and TiO_2, with markedly different characteristics. Al_2O_3 is known for its chemical inertness and good mechanical properties, and has typical applications for wear-resistance and electrical insulation.[12] Contrastingly, TiO_2 has interesting electronic and photocatalytic properties and is therefore used in microelectronics.[13] The variances between the displayed properties of Al_2O_3 and TiO_2 can also be considered on an atomistic level, with differences in generally displayed crystal structures, cation radii and valence states. Nonetheless, aluminium and titanium have comparable electronegativity, and both elements possess a strong affinity to oxygen.[14,15] Interestingly, when all three elements are combined, a repulsion has been shown to occur between aluminium and oxygen, which influences these elements' mutual solubilities.[16] This is also reflected in their pseudo-binary phase diagram, where the solubility of Al_2O_3 and TiO_2 in each other is practically negligible, as experimentally validated.[10,17] The pseudo-binary phase diagram of Al_2O_3 and TiO_2 is shown in *Figure 1*, based on Goldberg *et al.'s* original proposition and Hoffmann *et al.'s* publication.[18,19]

However, a single intermediate compound, known as aluminium titanate (Al_2TiO_5), can be found in this phase diagram at equimolar ratios. This particular phase has spurred increased research attention in recent years due to its many favourable thermal properties, which are described in the following chapter sections.
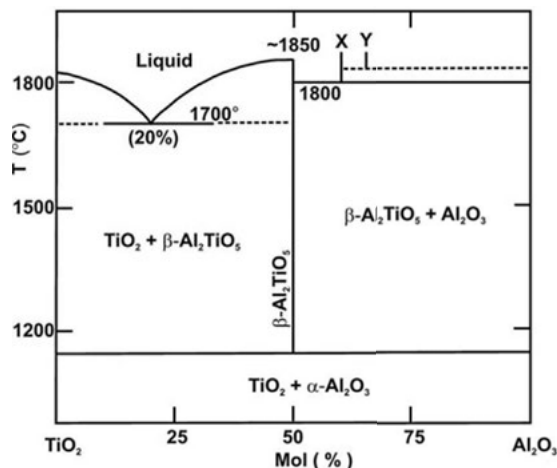
Figure 1. Pseudobinary TiO_2-Al_2O_3 phase diagram, as initially proposed by Goldberg and presented in the article *"Melt synthesis of Al_2TiO_5 containing composites and reinvestigation of the phase diagram Al_2O_3–TiO_2 by powder X-ray diffraction"* by S. Hoffmann, S. T. Norberg and M. Yoshimura, Journal of Electroceramics, 2006, vol. 16(**4**), pp. 327-330, DOI: 10.1007/s10832-006-9873-5. X and Y denote possible new compounds in the system. Reproduced with permission from Springer Nature.

3.2 Aluminium Titanate (Al_2TiO_5)

3.2.1 Structure and Properties

Al_2TiO_5 is isomorphous to a class of oxide compounds known as pseudobrookites, with the general formula $A_2^{3+}B^{4+}O_5$,[20] which Linus Pauling initially studied in 1930.[21] In the literature, the phase has been suggested to exist in two different polymorphic forms: an α-phase stable at temperatures above 1820 °C, and a β-form at lower temperatures.[22] The latter configuration crystallises in a base-centred orthorhombic system with space group *Cmcm*,[†] and its unit-cell and different axis projections are outlined in *Figure 2*.

[†] In older literature, the *Bbmm* designation is frequently used, which is identical to *Cmcm* except for an interchange of the *a*, *b*, and *c*-axes. For clarity, the *Cmcm* setting is adopted throughout this thesis.
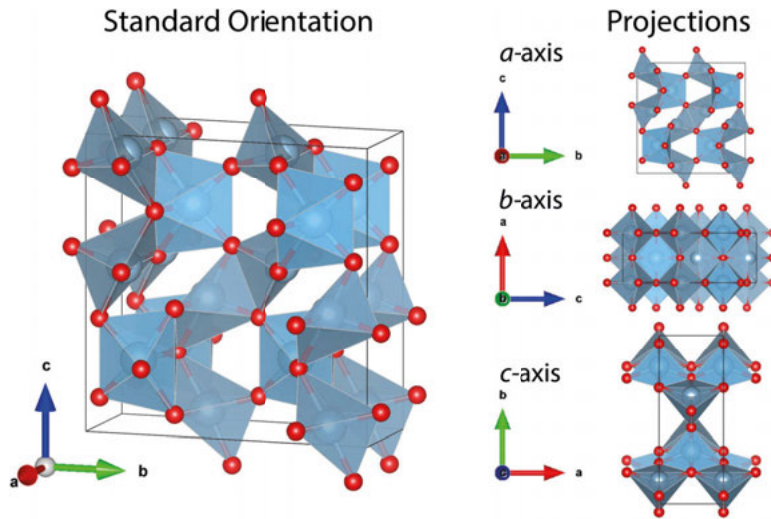
Figure 2. (Left) Unit cell of β-Al_2TiO_5, where red spheres represent the oxygen lattice. **(Right)** Axis projections of the cell.

The crystal structure comprises two octahedrally coordinated sites for the cations, denoted with Wycoff notation as *4c* (M1); *8f* (M2).[20,23,24] These sites form double-chained polyhedrons running parallel with the *c*-axis and are connected by apex-sharing oxygen atoms in the *a*-axis. Along the *b*-axis, edge-sharing occurs between the polyhedra. For these reasons, different bonding characteristics are present in Al_2TiO_5 depending on the crystallographic axes, giving rise to anisotropic material behaviours. This is particularly the case in terms of the phase's thermal expansion.[25] Upon heating, the structure tends to contract in the direction of its stronger apex-bonding oxygen atoms (*i.e.* the *a*-axis),[24] whereas the other two axes expand, albeit relatively marginally.[23] As a result, Al_2TiO_5 displays a low-to-negative thermal expansion, a property which, together with a high melting point (1860 °C),[26] thermal shock resistance (1544 W m^{-1}),[27] and low thermal conductivity (1.5 W m^{-1} K^{-1}),[27] characterise this phase's excellent refractory properties. Also, Al_2TiO_5 displays insufficient wetting for many non-ferrous metals and high corrosion resistance.[28,29] Therefore, the phase is a good candidate for many metallurgical applications.

However, the anisotropic bonding characteristics also give rise to microcracking phenomena during cooling,[30] which impairs the phase's mechanical properties. Notwithstanding this, Al_2TiO_5 displays a remarkable self-healing capability at elevated temperatures.[25,31] Also, its strength has been shown to increase significantly with temperature,[32,33] a behaviour that is uncommon among ceramic materials in general.[22]

Previous structural characterisations of Al_2TiO_5 by neutron diffraction,[23,34] X-ray diffraction,[24,35] and high-resolution TEM[36] have shown that Al_2TiO_5 readily displays

cationic disordering, meaning that aluminium and titanium may interchangeably reside in the available metal interstices. The cationic mixing on both sites causes local distortions to the oxygen octahedrons surrounding the cations.[37] This also contributes to the phase's configurational entropy and thermal stability at elevated temperatures.[38]

3.2.2 Routes of Synthesis

Conventional synthesis routes for Al_2TiO_5 involve solid-state reaction sintering by combining equimolar mixtures of Al_2O_3 and TiO_2. Owing to the low solubility between these phases and their strong stabilities, the thermodynamic driving force for this reaction is exceedingly low, being less than 600 J/mol below 1600 K.[39] This is several orders of magnitude lower than the synthesis of other ceramics.[39] For these reasons, high temperatures and long sintering times are typically required to synthesise Al_2TiO_5 with good purity.[10] Even so, the formation of Al_2TiO_5 without any remaining unreacted residues is challenging by this route.

Additional routes of synthesis include many soft-chemistry-based techniques such as sol-gel.[30,40–42] These routes allow Al_2TiO_5 to be synthesised at much lower temperatures and shorter processing times. The phase readily crystallises upon annealing at temperatures above 800 °C;[40] however, TiO_2 co-formation is a general problem described for these synthesis approaches.[40,42] This is also valid for many previous thin-film depositions attempts to attain this phase.[29,43]

3.2.3 Metastability and Thermal Stability

Al_2TiO_5 is a metastable compound at lower temperatures, and has frequently been reported to decompose into its binary constituents through a eutectoid reaction below 1280 °C. The reaction can be expressed as[44,45]

$$Al_2TiO_5 \Leftrightarrow Al_2O_3 + TiO_2 \text{ (rutile)}$$
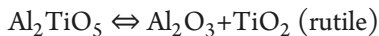
Which, notably, is completely reversible.[22] The reaction is sluggish, however, and typically deemed as kinetically impeded at temperatures below 800 °C.[45] This implies that a stability window exists between approximately 800 – 1280 °C where the phase is suggested to decompose. Therefore, significant research has been devoted in the past literature to understand the decomposition mechanism and further improve Al_2TiO_5's thermal stability.[23,34,45–47] As a general approach, it has been found that doping with certain elements, particularly magnesium, can significantly enhance the phase's thermal stability.[44]

3.3   New, Unconventional Phases in the Al–Ti–O System

Initial explorations by Lang *et al.* in 1952,[48] and also later by Goldberg,[18] have indicated the possible existence of additional phases in the Al–Ti–O system beyond Al_2TiO_5, particularly on the Al-enriched side. Much later, Norberg *et al.* successfully extracted a single crystal by rapidly melting Al_2O_3 and TiO_2 powders in an arc-imaging furnace. The stoichiometry of the crystal was determined as $Al_6Ti_2O_{13}$.[49] The phase shares many structural similarities with Al_2TiO_5, where the main difference being the presence of lower coordinating sites in $Al_6Ti_2O_{13}$ in the form of trigonal bipyramids. Besides the octahedra that may randomly host titanium or aluminium, these lower coordinating sites were suggested to be exclusively occupied by aluminium ions. The lower coordinating sites entail a point symmetry loss, leading to an elongation of the *c*-axis in $Al_6Ti_2O_{13}$ compared to Al_2TiO_5. The unit cell of $Al_6Ti_2O_{13}$ can be viewed in *Figure 3*.

Subsequent investigations by Hoffmann *et al.* also led to the discovery of another phase in the Al–Ti–O system.[50] This phase is described as an intergrowth between Al_2TiO_5 and $Al_6Ti_2O_{13}$. Therefore, this phase also shares many structural similarities with these two phases. Based on structural modelling, Hoffmann *et al.* determined the phase's stoichiometry to $Al_{16}Ti_5O_{34}$. Analogous to $Al_6Ti_2O_{13}$, the *c*-axis is significantly extended in $Al_{16}Ti_5O_{34}$ compared to Al_2TiO_5, and its lower coordinating sites are also solely occupied by aluminium ions (similar to $Al_6Ti_2O_{13}$). Besides this, Hoffmann *et al.* also suggested that stacking faults were a characteristic feature of this intergrowth phase.[50] The unit cell structure of $Al_{16}Ti_5O_{34}$ can be seen alongside $Al_6Ti_2O_{13}$ in *Figure 3*. Moreover, a list of unit cell characteristics for Al_2TiO_5, $Al_6Ti_2O_{13}$, and $Al_{16}Ti_5O_{34}$ is given in *Table 1*.

The synthesis and findings of these unconventional phases in the $Al_xTi_yO_z$ coatings made within this thesis are described in **Paper I**. Moreover, **Paper III** illustrates that the presence and migration of oxygen vacancies are likely responsible for forming these phases.
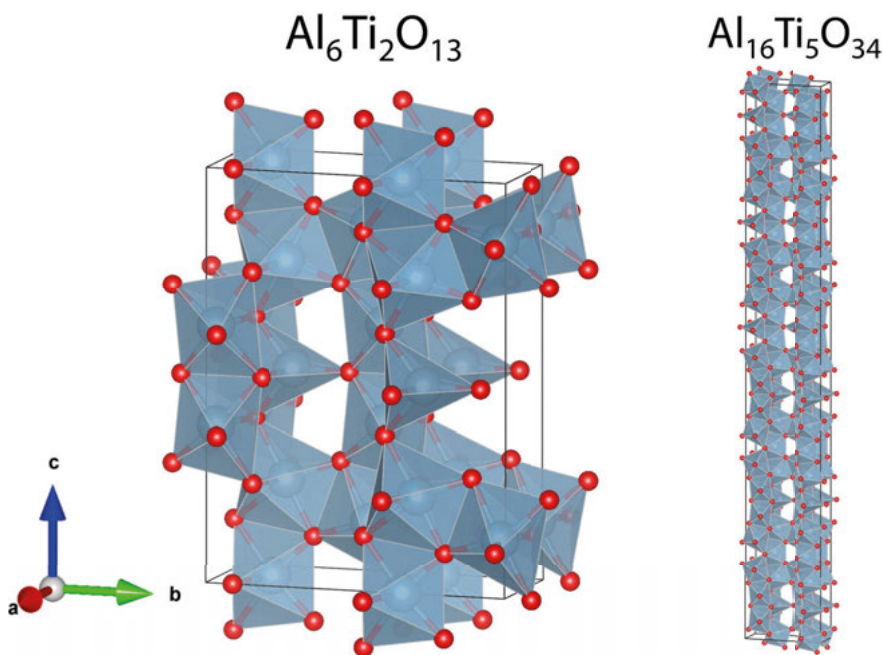
Figure 3. Unit cells of $Al_6Ti_2O_{13}$ and $Al_{16}Ti_5O_{34}$, viewed with the same axis orientations.

Table 1. Unit cell characteristics listed for Al_2TiO_5, $Al_6Ti_2O_{13}$, and $Al_{16}Ti_5O_{34}$.

	Al_2TiO_5	$Al_6Ti_2O_{13}$	$Al_{16}Ti_5O_{34}$
Crystal System	Orthorhombic	Orthorhombic	Orthorhombic
Space Group	Cmcm	Cm2m	Cmcm
a-axis (Å)	3.59100	3.65090	3.63995
b-axis (Å)	9.42900	9.36800	9.31070
c-axis (Å)	9.63600	12.55400	65.32100
Cell volume (Å³)	326.2705	429.3673	2213.7603
Reference #.	24	49	50

4   The CVD process

4.1   Fundamental Background

Chemical vapour deposition (CVD) denotes a synthesis technique wherein gaseous precursors react in the vicinity of a target surface, thus allowing the formation of a solid film. The 'chemical' aspects of the technique revolve around the many intricate gas-phase and surface reactions, which may (or may not) occur during depositions. Combined with many process parameters that may influence these reactions' overall behaviour, CVD marks for a highly versatile – but also complex – technique.[51] Versatile, in the sense that CVD can make a broad range of different materials, phases and film morphologies. Yet complex, in that an accurate control and balance of these parameters are required to obtain a stable and reproducible deposition process. Thus, an optimal CVD process requires careful consideration of the coating parameters, the used precursors, and the substrate material to be coated, which is graphically illustrated in the Venn diagram below (*Figure 4*).
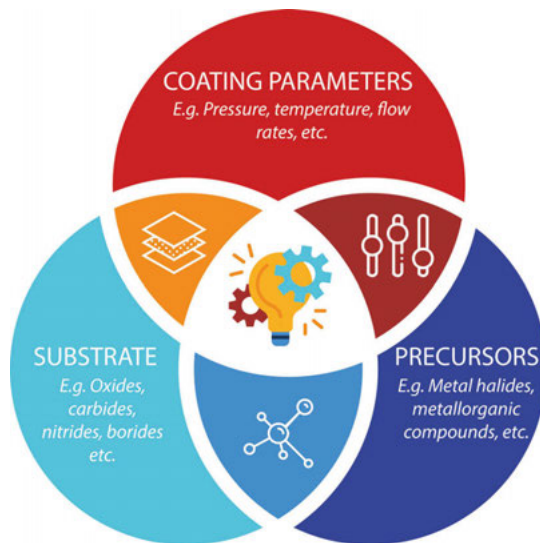
Figure 4. Venn diagram representing the three key factors involved in the process optimisation of a CVD process.

4.1.1 Thermodynamic Aspects

From a thermodynamic perspective, most reactions occurring in CVD are endothermic;[51] that is, energy must be supplied to the system to drive these. This can be done in numerous ways, leading to various versions of CVD known by their different acronyms.[51] Typically, the reactions are activated from thermal heating, whereby conventional CVD – using metal halide-based precursors – typically operates above 900 ° C.[52] The introduction of other, more labile precursors, like metal-organic ones, has enabled CVD to also operate at more reduced temperatures, typically in the range of 200–600 °C.

Thermodynamics is an integral part of any CVD process, which dictates the possible phase outcome given a particular set of experimental conditions, including temperature, pressure, the type of precursors, and their relative compositions/amounts. In theory, the possible phase outcomes can be predicted based on a minimisation of the Gibbs free energy; however, as it turns out with CVD, such predictions are rarely easily done. First of all, thermodynamic calculations require the accurate determination of many basic thermodynamic parameters for the involved reactants, which are not always available.[53] Secondly, even in best-case scenarios where calculations can be made, they are usually made based on the assumption of chemical equilibrium. Nevertheless, CVD is frequently a non-equilibrium process[52,53] due to its open-type design and lack of mass conservation; that is, there is a continuous stream of gases and precursors during its operation. The latter aspect not only constitutes a limitation of the technique from a thermodynamic perspective but also marks one of the technique's greatest advantages. Because CVD can operate far from any equilibrium conditions, and because of the high entropic contribution ascribed to the mixing of gaseous reactants,[54] the technique can produce many non-equilibrium (metastable) phases that are not easily attainable by other techniques, like solid-state syntheses. This advantage is exploited throughout this thesis in synthesising aluminium titanate, and also constitutes the scientific basis for **Paper I**.

4.1.2 Kinetic Aspects

Kinetics also plays a significant role in CVD, influencing the possible phase outcomes and the overall morphologies and microstructures of the deposited coatings.[52] While it is generally challenging to extract exact reaction mechanisms for the involved precursors, they can roughly be divided into some key kinetic steps, where the precursors are typically:[51–53]

1. Evaporated and transported into the reaction chamber.
2. Undergoes *homogenous* gas-phase reactions to produce reactive intermediates and by-products.
3. Transported, along with the reaction intermediates, to the substrate surface.
4. Adsorbed on the substrate surface, either through chemisorption or physisorption.
5. Undergoes *heterogeneous* surface reactions, nucleation, growth, and surface diffusion to various growth sites.
6. Desorbed, along with any formed by-products, from the substrate surface.
7. Transported away from the substrate surface back into the gas phase.
8. Transported and exhausted away from the main reactor zone.

Notably, all of these steps carry their own kinetic rate constant, and the slowest reaction step determines the overall deposition rate. In general, it is recognised that the slowest step in a CVD process is determined either by the mass transport to and from the substrate surface, or the gaseous/surface reactions that may occur during depositions. Typically, this is represented by three different kinetic regimes that influence not only the actual growth rates during deposition but also the nature of the deposited film. Hence, it is typically essential to determine what regime a CVD process operates in to acquire the best possible film outcome. This can be done by evaluating the growth rate $\dot{G}_r$ as a function of deposition temperature, which frequently follows an exponential relationship according to an Arrhenius expression:[51]

$$\dot{G}_r \propto \exp\left(-\frac{E_A}{RT}\right) \qquad \textbf{(Eq. 1.)}$$

where E_a denotes the apparent activation energy of deposition, R is the gas constant, and T is the temperature in Kelvin. Thus, taking the logarithm of the aforementioned expression and plotting this versus the reciprocal temperature T^{-1}, linear relationships are usually found where the slopes relate to the apparent activation

energy for given temperature ranges. A compilation of the various slopes then reveals the kinetic regimes at different temperatures, as outlined in *Figure 5* below.
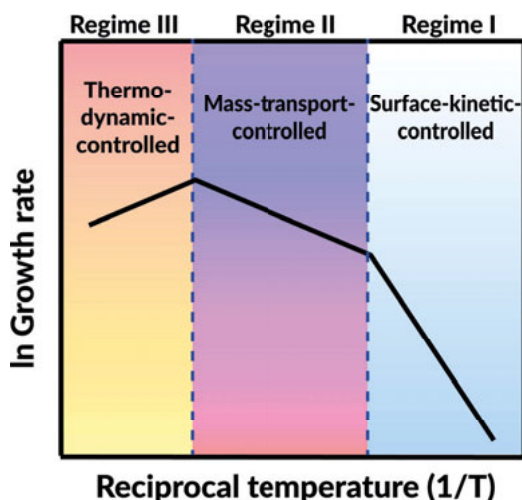
Figure 5. Schematic plot of growth rate as a function of reciprocal temperature, outlining three different linear slopes that mark the possible kinetic regimes in a CVD process. Each zone's characteristics are explained in the text.

4.1.2.1 Surface-Kinetic-Controlled Regime

In the first regime, the growth rate is kinetically impeded by the reactions occurring close to the substrate surface. The supply of precursors to the substrate is sufficient and is not depleted during the depositions.[51] Operating the CVD process in this regime is generally beneficial, as it allows for the greatest process control and regularly yields dense and uniform coating morphologies.[53]

4.1.2.2 Mass-Transport-Controlled Regime

For the second regime, the growth rate is limited by the mass supply of precursors to and from the substrate surface. The surface or gas-phase reactions in this regime occur faster than the supply of precursors, leading to a depletion of precursors closest to the substrate.[51] Noteworthy, this depletion may sometimes cause detrimental effects on the film morphology by lowering its overall density and making the film more porous. For these reasons, operation in this kinetic regime is usually unwanted, depending on the intended application of the growing coating.

4.1.2.3 Thermodynamic-Controlled Regime

In some depositions, a third kinetic regime can exist at even more elevated temperatures or low gas-flow rates, characterised by a non-Arrhenius behaviour and negative slope (*i.e.* decreasing growth rate with temperature). In this regime, the gaseous precursors have sufficient thermal energy so that they will not readily adsorb onto the surface.[51] Instead, they are reacting in the gas phase, thus becoming the rate-limiting step of the deposition.

4.1.3 Boundary Layer Formation

It is essential to notice that in the previous descriptions, the supply of precursors to the surface is also determined by fluid dynamics.[53] In terms of laminar flow, which is the most common type of flow in a CVD process, the movement of the gases is influenced by the viscous drag caused by the walls of the reactor and the substrate surface. This results in a boundary layer formation, where the mass flow and gas velocity differ from the rest of the reactor and gradually decrease towards the reactor walls/substrate surface.[54] Transportation of gases across the boundary layer typically occurs through gaseous diffusion, whose characteristic distance $\delta(x)$ can be expressed as[54]

$$\delta(x) = \sqrt{Dt} = \sqrt{v(x/U_\infty)} \qquad \textbf{(Eq. 2.)}$$

where D is a diffusion coefficient, t is the time, v is the kinematic viscosity (*i.e.* the ratio between the viscosity and density of the flowing gas), *x is* the distance from the reactor inlet, and U_∞ the total gas flow velocity found in the reactor.

The existence of a boundary layer has several important consequences regarding the overall reaction kinetics of the CVD process. Because the supply (and access of) gaseous precursors to the substrate dictate the operating kinetic regime, a thicker layer would naturally lead to a greater depletion of the precursor concentration. This would favour a mass-transport-controlled (or even a thermodynamic-controlled regime). Likewise, a slim boundary layer would lead to an insignificant concentration drop of the precursor, favouring a surface-kinetic-controlled regime instead.

As evident from *Equation 2*, the thickness of the boundary layer depends not only on the diffusion coefficient but also on the flow rates and partial pressures of the involved gases. This means that beyond the influence of the growth temperature, these parameters can also be adjusted to steer the CVD process into the most desired kinetic regime, which is further emphasised in the next section.

4.1.4   Process Parameter Considerations

In depositing Al_2TiO_5-based coatings, various considerations of the possible process parameters have been made to acquire the most favourable deposition conditions. For reasons explained in the previous section, a surface-kinetic-controlled regime is generally desired. Therefore, to facilitate the overall CVD process and promote this reaction regime, the following process measures have been taken:

1) **Intermediate deposition temperatures**. Seen in *Figure 5*, a lower deposition temperature typically favours a surface-kinetic-controlled deposition process since the overall reaction rate scales with the temperature. However, a too-low temperature is unwanted, as this leads to incomplete reactions of the precursors and also hydroxylation of the surface, rather than oxide formations. Similarly, too-high deposition temperatures would lead to the thermal degradation of the used aluminium source precursor (see also *Section 7.1.1*) through *homogenous* reactions in the gas phase, resulting in powder formations. For that reason, 450 °C has been found as the optimal deposition temperature.

2) **Fast flow rates of the bulk carrier gas**. This decreases the residual time of the precursors in the reactor, which favours a situation where the concentration of the precursors in the reactor remains mostly unchanged. Also, it decreases the boundary layer thickness, as per *Equation* 2. Accordingly, a higher flow rate promotes a surface-kinetic-controlled regime,[54] and *vice versa* in case of lower flow rates.

3) **Low precursor gas flows**. This reduces the risk of homogenous gas-phase reactions and favours the surface reactions to be rate-determining during the deposition process.

4) **Decreasing the pressure**. The diffusion coefficient is inversely proportional to the pressure.[52,54] Therefore, decreasing the pressure increases the diffusion coefficient, which limits the boundary layer thickness and promotes a surface-kinetic-controlled regime.[54] Additionally, a lower pressure causes an increase in the precursors' mean free path, thereby also reducing the boundary layer thickness.

4.2   Instrumentation

A significant part of this thesis work has been devoted to designing and constructing a novel CVD instrument capable of producing oxide-based coatings from metalorganic precursors. The CVD system is schematically illustrated in *Figure 6*. Further details about the system are also provided in the following sections, and its main features are specified in *Table 2*. Moreover, a complete list of used process parameters for the depositions is presented in the results section, *Table 3*, on page 58.
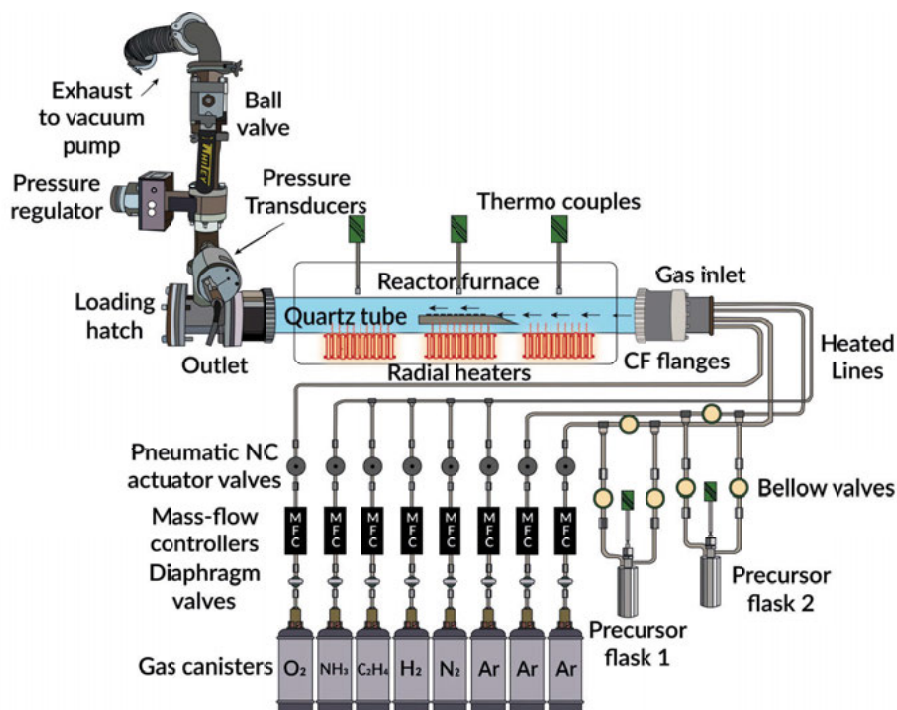
Figure 6. Schematic illustration of the CVD system used during this thesis work, highlighting its main features and components. Further details about the system are provided in the text.

Table 2. List of main specifications of the constructed CVD instrument.

CVD System	
Gas flow state	Open CVD
Activated manner	Thermal
Deposition zones	3-zone
Wall type	Hot-wall
Reactor geometry	Horizontal tube
Reactor material	Quartz
Reactor dimensions	Ø 600 mm (outer), Ø (inner) 580 mm, length: 1600 mm
Temperature range	20 – 1000 °C
Pressure range	1 – 760 Torr
Pressure limit (pump specs.)	23 mTorr
Number of bulk gas sources	6
Number of evaporators	2
Type of bulk gases	O_2, NH_3, C_2H_4, H_2, N_2, Ar
Possible flow rates	10 – 100 sccm (1000 sccm for Ar)
Substrate holder	Graphite-based

4.2.1 General Design Aspects

As previously noted, many possible process parameters may influence a CVD process's outcome. These parameters include, among many others:[51,53]

- Substrate temperature.
- Reactor pressure.
- Partial pressures of precursors.
- Gas flow rates.
- Flow dynamics in the reactor.
- Deposition time.
- Residual time of gases.

These parameters must be considered when designing a CVD instrument, and the foremost design strategy should focus on reaching adequate process control to allow for a reproducible and upscalable CVD process. In essence, the above-listed criteria

can be divided into three separate parts, being emphasised in *Figure 7*, in which the CVD instrument:[51,53]

- ➢ Allows a controllable and continuous delivery of the precursor vapours and any other gaseous species into a reaction zone.
- ➢ Provides sufficient energy to drive any chemical reactions within the reactor zone.
- ➢ Removes and handles any by-products that are formed during the depositions.
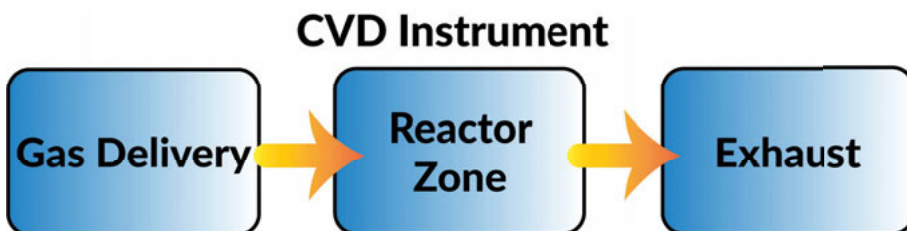
Figure 7. Flowchart emphasising the most significant parts of a CVD system.

4.2.2   Gas Delivery System

The gas delivery system of the constructed CVD system comprises six possible bulk gas sources, listed in *Table 2*, along with two separate evaporator lines for the metalorganic precursors. Oxygen supply occurs through a separate pipeline to avoid contaminations and unwanted reactions with ammonia or hydrogen. All pipework (including the precursor flasks) consists of ¼" 316L stainless steel that is either orbital welded or connected to various valves and parts using Swagelok® vacuum coupling radiation (VCR) fittings. Notably, the two evaporator lines constitute an essential part of the CVD system, enabling various metalorganic precursors to be combined concurrently or sequentially during deposition.

Each gas flow into the system is controlled by several mass-flow control units (MFC, Tylan 2900 series) connected to monitoring PR4000B regulator units (MKS). The MFC measures the flow rate of gasses by monitoring a proportional change in the temperature of a small heating element, which in turn depends on the gas' specific heat capacity.[51] Depending on what type of gas flows through the MFC, a conversion factor needs to be entered in the regulator unit to obtain a correct flow measure. Flow rates are typically given in units of "*sccm*", *i.e.* standard cm^3 per minute, where "standard" denotes 0 ° C and 1 atm. Although the designation "mass-flow" gives the impression that the mass is being measured, it is imperative to note that, in actuality, the MFC measures a volumetric flow.[51]

The CVD system is equipped with two different MFC units, capable of controlling the flow rates in the range of 10–100 sccm for O_2, NH_3, C_2H_4, H_2, and N_2, respectively, and 10–1000 sccm for Ar. Argon is mainly used as a carrier gas during depositions and is supplied both in the precursor and bulk pipelines. Because of the high air and moisture sensitivity of the metalorganic precursors, the carrier gas must be of high purity.[52] For that reason, Air Liquide Alphagaz™ has been used (purity > 99.9999%) in all experiments of this thesis work.[55]

The purpose of the carrier gas is threefold. First, it creates a natural flow by convection for the gases to travel into the reactor, reducing the back-flow of not least the precursor vapours that may otherwise damage or clog the MFC controllers. As a further precaution against this, each MFC line is also equipped with disposable check valves. Secondly, the carrier gas saturates the precursor vapours in the evaporators and reduces the amount of vapours that may condense on the tube walls and fittings on their way to the reactor inlet. Thirdly, the carrier gas dilutes the precursor vapours, reducing the collisions between the precursor gas molecules and hence decreasing the risk of homogenous nucleation in the gas phase. Such events are unwanted because they deplete the precursor and lead to powder formations in the reactor, which could degrade the actual deposition process.

The supply of precursors is mediated from the two precursor flasks, also known as "evaporators" or "bubblers". During operation, a small stream of carrier gas is entered into the bottom of the flask through a separate pipe, saturates the precursor solution[51] and then carries the precursor through the pipework upstream towards the reactor inlet. The amount of precursor entering the reactor is highly dependent on its vapour pressure which, in turn, depends on the solution temperature in the container. Therefore, a good temperature control of the precursor flasks is needed to obtain a steady and controllable precursor flow.[51] For that reason, specially-designed heating jackets are used for the flasks (Hemi Heating), which allows for an accurate temperature determination to a tenth of a degree Celsius. The temperature is monitored using several type K thermocouple units connected to Eurotherm® 3216 PID controller units. In each container, a separate thermocouple is mounted in the cap that goes into the precursor solution. This allows accurate determination of the actual temperature inside each bottle during the depositions.

Recondensation of the precursor in the pipework is a possible yet highly unwanted feature that may deplete or clog the pipework in the CVD reactor. Besides the critical role of the carrier gas, as explained above, such risk can be reduced by heating all the pipework that goes into the reactor.[53] The CVD system uses glass-fibre heating

tapes (Hemi Heating) wrapped around all the pipework to alleviate the risk of re-condensation. This also includes the precursor lines and the other gas lines that are pre-heated to avoid thermal gradients in the system.[51]

4.2.3   Reactor Zone

The reactor zone represents the "heart" of the system, where all the chemical reactions occur. It comprises a 1600 mm long horizontal quartz tube connected to the system through glass-metal ConFlat® (CF) flanges. To ensure adequate vacuum of the system, each CF flange uses three Viton® O-ring seals towards the quartz reactor tube. Gases and precursors are delivered from the inlet through several stainless steel effuser tubes.

The CVD system is a hot-wall and open-type construction, wherein the reactions are activated through thermal heating using three different resistive elements. Hence, the reactor is a 3-zone system. The term "hot-wall" implies that the entire reactor is heated, unlike in "cold-wall". The benefit of such a system is that a larger number of samples can be coated simultaneously, while it also avoids thermal gradients that otherwise could impact the process parameter control.[53] Similarly, the reactor is an open-type, meaning that the gases continuously stream through the system and are pumped away during its operation.[52]

Analogous to the gas delivery, a good and uniform reactor heating is required; therefore, several thermocouples are mounted close to the reactor wall to monitor the temperature of each deposition zone. Nevertheless, the actual temperature inside the reactor usually differs from the measured one.[51] To check this offset, temperature reactor profiles were measured inside the reactor using a 2 m long K-type thermocouple mounted through an O-ring sealed CF-flange at the reactor outlet. Measurements were made at various positions inside the reactor, counted from the loading hatch, using comparable argon gas flows and pressures used for the actual depositions. A typical profile is displayed in *Figure 8*, which can be found on the next page. Essentially, this figure shows that there is no temperature gradient within the main deposition zone of the system (*i.e.* between the 3rd and 2nd thermocouple). However, there is a slight overshoot in the actual temperature within the reactor compared to the target set-point temperature. The temperature offset is in the range of 5 %, which marks the temperature accuracy of the CVD system.

A graphite sample holder with fifteen 2.25 cm^2 sample slots was typically used for depositions.
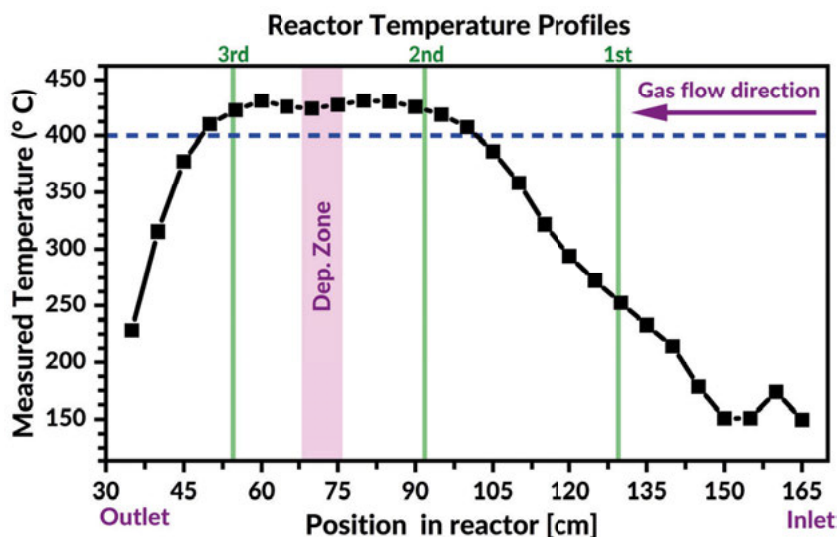
Figure 8. Temperature profile displaying the actual temperature within the reactor. Green lines mark the position of each thermocouple that monitors the temperature of the reactor from outside. The set-points used for each thermocouple during the temperature check were 400 °C (3rd), 400 °C (2nd) and 230 °C (1st). Blue dotted line marks reference (set-point) temperature. The purple-coloured region marks the main deposition zone, where the sample holder is typically placed.

4.2.4 Exhaust and Vacuum System

Controlling the pressure is vital in a CVD process,[51] and most commonly, low-pressure (vacuum) environments are used. Pumping the system to vacuum levels was made using a 2.2 kW dry pump (Edwards QDP40). The pressure was monitored from two separate 10/100 torr Baratron® capacitance manometer units connected to an MKS 651C controller. This unit was also connected to an automatic butterfly check valve, allowing the pressure inside the reactor to be regulated.

4.2.5 Safety Aspects

Safety is a general concern for conventional CVD, where hazardous and corrosive gases are frequently used. The safety concerns in metalorganic CVD are arguably less stringent, owing to the less toxic by-products formed during the depositions. Nonetheless, to avoid exposure to any fumes and gases and verify that there are no leaks in the system, continuous leak-testing was made using a Pfeiffer ASM 340 unit. The CVD reactor is also contained inside a ventilated cabinet.

4.3 Precursors

4.3.1 General Requirements and Aspects

Choosing suitable precursors in a CVD process is essential to obtain the desired composition, phase, structure, morphology, and overall properties of the deposited coating. A wide range of different precursors exists for CVD, comprising almost all the elements in the periodic table and existing in the form of liquids, gases, or sublimable solids.[56,57] Generally, the choice of precursors can be made based on some general criteria:[51,58,59]

- Good volatility and high vapour pressures, allowing a constant and controllable flux of the precursor in its gaseous state.
- Large temperature window for its reactions, allowing the precursor to be readily combined with other types of precursors.
- Sufficient long-term stability without degradation over time.
- Clean and non-toxic reactivity.
- Easy to use, inexpensive, commercially available, and upscalable.

In terms of generating oxides, there are two main groups of precursors to be used:

- Halide-based, which are the most commonly used in conventional CVD.
- Metal-organic and organo-metallic compounds.[‡]

As briefly mentioned in the introduction, halide-based precursors have the disadvantage of producing highly toxic and corrosive byproducts,[59] which may negatively interact with the substrate to be coated or the CVD reactor itself. Moreover, metal halides generally display high thermal stabilities, thus requiring higher deposition temperatures to activate them and reach adequate gaseous volatilities. Not only does this limit the type of substrates that can be coated, but it also affects the possibility of obtaining novel multicomponent phases. The reason is that metal halides, in general, may display a wide range of different vapour pressures, thus making it challenging to find overlapping process windows when two or more of these

---

[‡] The difference between a metal-organic and organo-metallic compound may be understood as follows. A metal-organic compound comprises a metal coordinated to an organic ligand but does not require any direct metal-carbon bond. An organometallic compound, on the other hand, consists of a metal directly coordinated to one or several carbon atoms.[51]

precursors are concurrently used. Contrastingly, metalorganic precursors have the advantage of having higher vapour pressures at lower temperatures. Their volatilities can also be tailored based on the type of ligands bonded to the metal centre.[59–61] This feature, combined with the fact that alkoxides may react with higher purities and through similar mechanisms, also implies that alkoxides can be combined in the same CVD process to yield possible mixed-metal multicomponent coatings. However, this increased versatility comes at the cost of deteriorated long-term storage capabilities and more cumbersome handling of these precursors, as outlined in *Section 4.3.2*.

The metalorganic and organo-metallic compounds typically consist of β-diketones, alkyls, alkoxides, or combinations thereof.[58] The metal centre in β-diketones bonds to an organic ligand via two bridging oxygen atoms, whereas the metal centre in an alkoxide bond to a ligand through a single oxygen.[51] Alkyls lack direct M–O bonds and consist of M–C bond assemblages. The degree of reactivity typically increases in the order β-diketones < Alkoxides < Alkyls. However, the lack of M–O bonds in alkyl-based organometallic compounds means that an additional oxygen supply is required when these are used to convert them into oxides. Furthermore, compounds containing M–C bonds typically result in increased carbon impurities in the growing film,[62] thus making these compounds less appropriate in a CVD process. Likewise, β-diketones' reduced reactivity implies that higher evaporator and substrate temperatures are needed for their depositions, which limits their flexibilities to a certain extent. Accordingly, alkoxides are generally the most versatile group in obtaining various metal oxide phases in CVD,[60,61] which also constitute the key focus for this thesis work.

4.3.2   Properties of Alkoxides

Metal alkoxides, with the general formula $M(OR)_x$, contain one or more metal atoms coordinated to organic ligands by linking oxygen atoms.[61] The ligands typically constitute various alkyl groups. Generally, alkoxides display a strong reactivity to a wide range of chemical compounds. This reactivity stems from the high polarity of the M–O–C bond, caused by oxygen's electronegativity, which entails these compounds' susceptibility to nucleophilic attacks.[57] The most common example involves their reaction with water,[60] a feature exploited in sol-gel and soft-chemistry synthesis approaches to produce ceramic nanomaterials. Nevertheless, this increased reactivity may also negatively impact alkoxides' long-term stability and handling. In fact, most alkoxides are highly hygroscopic, *i.e.*, they can readily adsorb atmospheric moisture, which may cause unwanted reactions and degradations.

Therefore, handling, storing, and preparing the alkoxides for CVD requires working in constant inert atmospheres, which is typically done by using a glove-box.

The two alkoxides used in this thesis are aluminium isopropoxide (AIP) and titanium isopropoxide (TIP), whose structures are displayed in *Figure 9*. Whereas TIP is an amber-coloured volatile liquid at room temperature, AIP is a solid white powder. Consequently, to acquire sufficient volatility for the AIP precursor, it must be melted in its container close to its melting point (*i.e.* 140 °C) before any depositions can be made. Essentially, this procedure leaves the precursor in a supercooled fluid[63,64] with improved volatility. However, it should be noted that this state is not stable over long periods for AIP. Because alkoxides generally tend to expand their coordination spheres,[57] they may form oligomeric structures with time, yielding gradually deteriorating vapour pressures.[61] In terms of AIP, this "ageing behaviour" has been the subject of various studies in the available literature.[64–66] Empirical evaluations during this thesis work have shown that AIP's behaviour remains mostly the same for approximately ten days, after which the evaporator must be refilled to achieve adequate volatility again. While this ageing is a general feature ascribed to many alkoxides,[57,61] it is worth mentioning that similar behaviour has not been observed for TIP, which shows excellent thermal stability over long time periods.
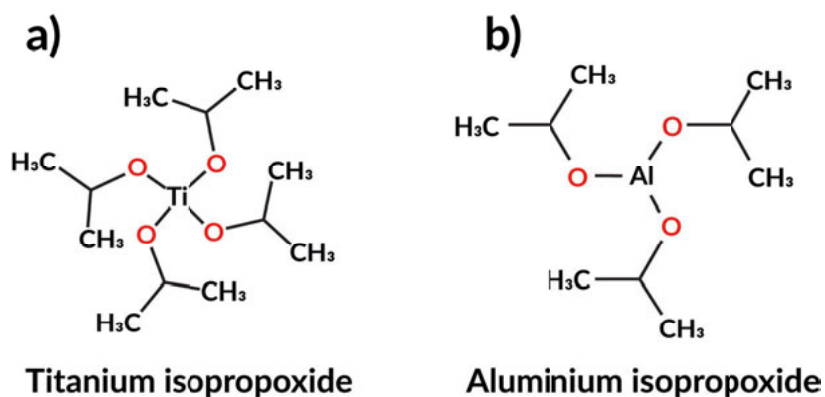
Figure 9. Typical molecular structures of titanium isopropoxide (TIP) and aluminium isopropoxide (AIP), shown in (a) and (b), respectively. Note that AIP may possibly also exist in a tetrameric form just like TIP (For reference, see Folting, K. *et al.*, Characterisation of Aluminium Isopropoxide and Aluminosiloxanes. *Polyhedron* **1991**, *10* (14), 1639–1646, DOI: 10.1016/S0277-5387(00)83775-4).

4.3.3 Reactions of Alkoxides

In terms of CVD, alkoxides are typically transformed into their oxide counterparts through thermal degradation by pyrolysis,[59] *i.e.*, without any external oxygen supply. An external supply of oxygen is seldom required since the alkoxides by themselves usually contain the necessary amount of oxygen to form into an oxide.[61]

In essence, there are predominantly two different reaction pathways that alkoxides may undergo in CVD: cyclic elimination[67] and β-hydride elimination,[51,68–70] which are schematically depicted in *Figure 10*. In both processes, the alkoxide may liberate an alkene group (or similar), thus yielding a hydroxylated intermediate.[51] These hydroxylated intermediates may, in turn, react with each other by condensation reactions, ultimately resulting in homometallic M–O–M bond assemblages through the liberation of water as a product. However, if two or more alkoxides are used concurrently in the process, which also operates under similar decomposition mechanisms and kinetics, it becomes possible to form heterometallic M–O–M* instead. Accordingly, such a strategy provides a chemical route to achieve multicomponent (mixed-metal) oxides by CVD, and forms a central part of synthesising Al_2TiO_5-based coatings, as explained in **Paper I**.
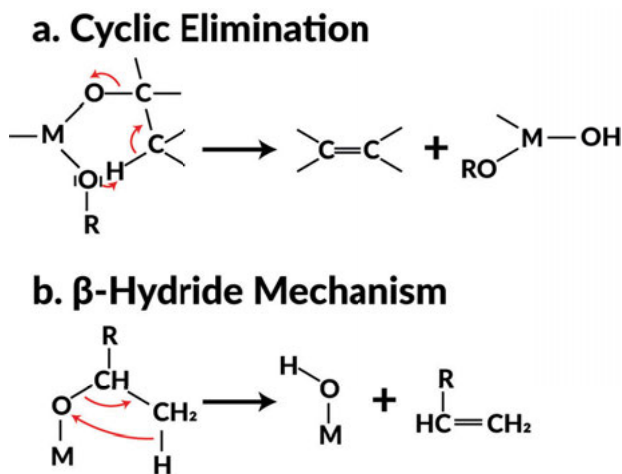
Figure 10. Schematic description of two possible reaction mechanisms for transforming metal alkoxides into their oxide counterparts by forming hydroxylated intermediates. These hydroxylated intermediates may, in turn, react with each other through condensation reactions, thus resulting in the formation of metal-oxygen bonds.

5 Crystallisation

5.1 Classical Nucleation Theory (CNT)

According to CNT, two concurrent and overlapping processes are involved in the transition between the disordered and ordered state: nucleation and growth. Typically, nucleation dominates at the initial stages of crystallisation, whereas growth dominates in the subsequent latter one. Although the changeover between these two domains is seldom sharply defined, it can be roughly estimated based on the sigmoidal-shaped transition curve, shown in *Figure 11*, which most crystallisation processes follow.
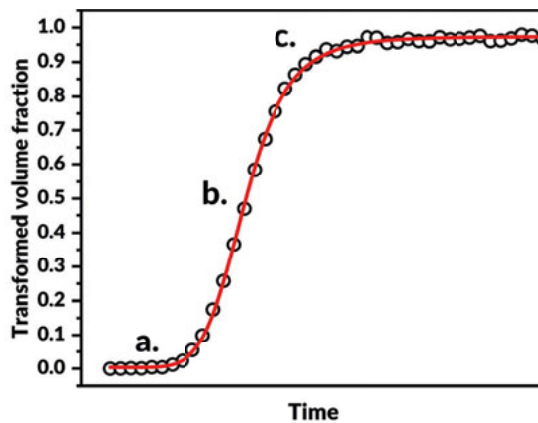
Figure 11. Typical transformation curve explaining the process of crystallisation in most materials. Three different stages can be noticed: in (a.), the nucleation process dominates. In (b.), the" growth zone" of the transition has been entered, where the nucleation rate typically has reached its steady-state value. In (c.), the transformation starts to decline and concludes as the amorphous matrix becomes increasingly exhausted, and the formed nuclei begin to impinge with each other.

5.1.1 Nucleation and Thermodynamic Aspects

In the initial stages of crystallisation, a cooperative set of atoms in the disordered state will arrange to match the crystalline one, thus forming a cluster of elements composing a nucleus.[71,72] CNT commonly regard this event as stochastic (random) induced by any vibrational fluctuations happening in the material.[73] Thus, crystallisation is a thermally activated process governed by the rules set by classical thermodynamics.[74] The total driving force for this process is given by the change in Gibbs free energy between the disordered and crystalline states, herein denoted as ΔG_n. An expression linking ΔG_n with the total change in entropy (ΔS_{cryst}) and enthalpy (ΔH_{cryst}) during crystallisation can then be given as

$$\Delta G_n = \Delta H_{cryst} - T\Delta S_{cryst} \qquad \textbf{(Eq. 3.)}$$

Because these thermodynamic properties all represent individual state functions,[75] ΔG_n can also be divided into its various sub-contributions. For nucleation (ΔG_n), the three most common and significant ones can arithmetically be combined according to

$$\Delta G_n = \Delta G_v + \Delta G_s + \Delta G_\varepsilon \qquad \textbf{(Eq. 4.)}$$

where ΔG_v denotes the volume-free energy of the new-forming crystalline phase, ΔG_s the surface-free energy, and ΔG_ε represents the strain energy contribution caused mainly by variations in densities between the amorphous and crystalline states.[76,77] The latter term may also incorporate elastic strains found particularly within thin films and coatings.[78,79]

Generally, since the crystalline state represents a lower energetic condition than the disordered one,[80,81] ΔG_v adopts negative values, thus acting favourably to the overall thermodynamic driving force.[80,82,83] ΔG_s and ΔG_ε, on the other hand, typically adopts positive values, thereby reducing the total driving force.[80–83] Hence, the competing interests between these three terms translate to nucleation's net driving force.[80,84–86] In this respect, CNT regards a single responsible parameter to determine whether ΔG_n becomes thermodynamically favourable or not, namely, the radius of the nucleus.[77,86] This principle is schematically explained in *Figure 12*. The surface energy reaches its uppermost values for small radii, whereas it diminishes as the radius progressively becomes larger.[76,85,86] Thus, it follows that, for a radius that is below a critical value (r^*), the ΔG_s-term will dominate and yield a positive net ΔG_n-value so that nucleation becomes thermodynamically unfeasible.[80,85,87] In these cases, CNT states that any pre-forming nuclei will dissolve and return to the

disordered state.[80,87] In other words, no stable intermediate states between the amorphous and crystalline states should exist.

However, if the radius of the emerging nucleus will, for any reason, pass the energetic threshold represented in r^* so that ΔG_v dominates instead of ΔG_s or ΔG_ε, the process of nucleation will suddenly become thermodynamically advantageous.[76] In that case, the progression and growth of a stable nucleus will occur.[81] Consequently, CNT states that the radius of the nucleus represents a key parameter dictating the thermodynamic driving force of crystallisation.
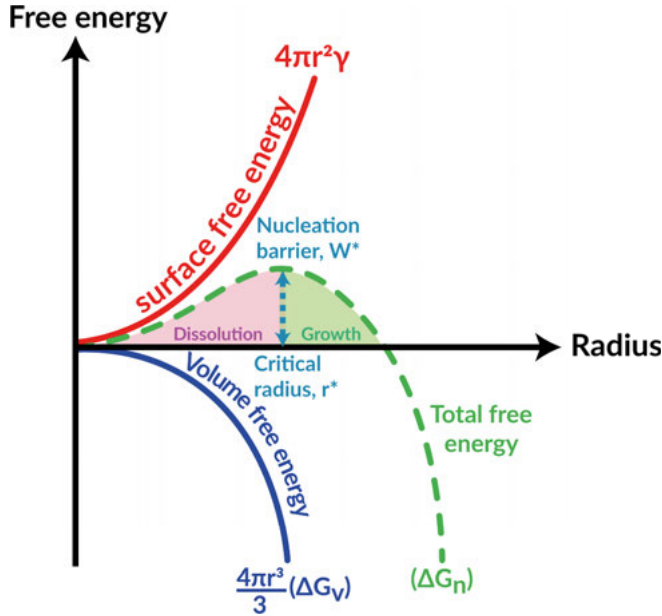
Figure 12. Free energy diagram illustrating the relation between the two energetic contributions, the volume free energy (seen in blue) and the surface-free energy (seen in red), with increasing radius of the forming nucleus. For low radius values, the surface-free energy term will dominate, leading to the dissolution of the forming nuclei back into the amorphous state. However, at a critical radius value r^*, where the volume free energy starts to dominate, a stable nucleus will form, leading to the growth stage and the progression of the crystallisation process.

If the thermodynamic contributions represented in ΔG_ε is embedded into the surface-free energy term, so that ΔG_s and ΔG_v are mainly considered, an expression for the nucleation barrier W* can be given as[76]

$$W^* = \frac{16\pi\gamma^3}{3\Delta G_n^2} \qquad \textbf{(Eq. 5.)}$$

Where γ denotes the crystal-amorphous interfacial energy.[77,79] In the above equation, CNT assumes that the nucleation process proceeds equally in all geometrical directions through the attachment of monomeric units (*i.e.* isotropic growth), resulting in the formation of regularly shaped spheres.[88,89]

Because most of the detrimental impact on the thermodynamic driving force of nucleation stems from the surface-free energy term, it follows that any factor(s) that may reduce this term may also significantly facilitate the overall nucleation process. In this sense, CNT distinguishes two separate mechanisms for nucleation to occur, denoted as either *homogenous* or *heterogenous* nucleation, which is schematically explained in *Figure 13*.[79,86] In the first case, nucleation proceeds spontaneously within the disordered state due to thermal fluctuations, with little or no influence from any foreign elements or surfaces influencing this process.[73] In contrast, the second case denotes a process where nucleation preferentially occurs onto foreign surfaces, interfaces and parent grains, thereby reducing the surface-free energy term. Accordingly, heterogeneous nucleation corresponds to a theoretically less energy-demanding route for nucleation, implying that this mechanism should dominate most crystallisation processes. In reality, homogenous nucleation is also frequently encountered,[90–93] particularly in systems where nucleation is the most favoured process, and a strong resemblance between the disordered and crystalline states exists.[73,94,95]

Homogenous nucleation   Heterogeneous nucleation
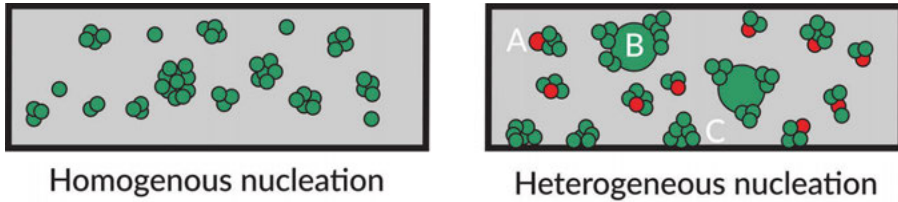
Figure 13. Schematic explanation of the two mechanisms for which nucleation may proceed. In the first homogenous case, nucleation occurs randomly within the amorphous media. In the second case, heterogenous nucleation may occur on, for example, (A) foreign elements or particles, represented in red, (B) parent crystals and (C) the substrate interface (in cases of thin films and coatings).

5.1.2 Growth Stage and Kinetic Aspects

Following the opening steps in forming a stable nucleus, the crystallisation process will proceed into the "growth stage". Once any nucleus enters this stage, it will continue to grow past its critical radius by interacting with the untransformed surrounding (disordered) matrix.[81] Normally, CNT states that this process is controlled by diffusion[76,79] where monomeric units – one by one – adhere and attach to the growing nucleus.[80] The rate at which this process proceeds may be denoted as the nucleation's growth rate. Similarly, the rate at which the numeric population of nuclei with a critical radius r^* appears is also formally known as the nucleation rate. The interplay between these two rates is crucial to consider during the amorphous-to-crystalline transition, as the hampering or enhancing of any of these may drastically affect the microstructural development and hence also the crystallised media's ultimate properties.

In the case of homogenous nucleation, an expression of the steady-state nucleation rate linking the energy barrier of nucleation (W^*) with its kinetic counterpart (ΔG_D) can be expressed as

$$I_{st} = I_0 \cdot \exp\left(-\frac{W^* + \Delta G_D}{K_B T} \right) \qquad \textbf{(Eq. 6.)}$$

where I_0 is a pre-exponential factor, K_B the Boltzmann's constant, and T the annealing temperature. Although crystallisation incorporates two individual kinetic processes, i.e. nucleation and growth, the process is frequently streamlined into a first-order transition within the CNT framework.[71,80,96,97] That is because the nucleation rate is typically much faster than the growth rate. Consequently, most crystallisation processes are treated as a (pseudo) first-order transition[98] where diffusion is primarily impeding the process from a kinetic point of view.[96] Commonly, this leads to the two frequently encountered designations of "diffusion-limited" and "diffusion-controlled" crystallisation, with similar meanings in this regard.[§] The opposite scenario, i.e. a "nucleation-controlled" crystallisation process, is rarely encountered and thus

---

§ From a linguistic perspective, the term "diffusion-limited" is not problem-free and may even be regarded as ambiguous. For example, "diffusion-limited" can both be interpreted such as the crystallisation process is kinetically limited by diffusion, or that the extent of diffusion is limited. Both cases are encountered in the available literature. The alternative term "diffusion-controlled" is arguably less frequently used, even though it should better clarify its meaning in terms of crystallisation, nucleation, and growth.

typically deemed unusual. Nonetheless, the finding of a nucleation-controlled crystallisation process forms the scientific basis of **Paper II** in this thesis.

5.1.3   The JMAK ("Avrami") Equation

The JMAK equation links the transformed crystalline volume fraction with time. It is most commonly used to model crystallisation transformation kinetics and to offer mechanistic insights into the process. The theories of this equation were developed simultaneously by many authors;[89] hence it is denoted by many different acronyms in the literature, KJMA, JMAK, JMA, or simply the "Avrami equation". Typically, the equation is expressed as

$$\alpha = 1 - \exp\left[-Kt^n\right] \qquad \textbf{(Eq. 7.)}$$

where α denotes the volume fraction transformed, and K and n are kinetic constants relating to the overall crystallisation rate and the dimensional expansion of the nuclei, respectively. In order to obtain these parameters, the KJMA equation is typically rewritten into a double-logarithmic function:

$$\ln\left(-\ln(1-\alpha)\right) = \ln K + n \ln t \qquad \textbf{(Eq. 8.)}$$

Allowing K and n to be extracted from a linear plot of $\ln\left(\ln\frac{1}{1-\alpha}\right)$ *vs ln t* in the isokinetic regime,[88,99] where nucleation and growth are regarded as time-invariant parameters. While K relates to the overall crystallisation rate for which crystallisation proceeds, n incorporates both the dimensional expansion (λ) of nucleation and its mechanistic probability (β), so that[100]

$$n = \lambda + \beta \qquad \textbf{(Eq. 9.)}$$

where $0 \leq \beta \leq 1$ and λ is a positive integer. For β, values close to 0 represent instantaneous nucleation, whereas 1 denotes continuous nucleation.[100] Hence, n typically adopts values so that $0 \leq n \leq 4$, though values outside this range can also be encountered.[101] For example, n being greater than four typically signifies a time-dependent (transient) nucleation rate, which has been observed in the crystallisation of several metallic glasses.[102–105] Moreover, similar notions have been observed in studying the crystallisation kinetics of the $Al_xTi_yO_z$ coatings in **Paper II**.

5.1.4   Limitations of CNT and Non-Classical Nucleation Routes

The theories concerning CNT have evolved for more than a century. While significant developments in our understanding have been made during these years, many concepts about nucleation and crystallisation still remain poorly understood. One reason is the many challenges encountered when examining nucleation and growth behaviours, which typically occur in very short time- and length scales, making it hard to reach by most analytical techniques.[95] Arguably, this has also contributed in that many of the original assumptions and ideas governing CNT are still being used and considered as generally applicable. These main assumptions can be summarised as follows:[95,106,107]

    a)   Monomeric addition of single components during growth (also referred to as Szilard's postulate).[108]

    b)   Geometrical optimisation of nuclei formation based on spherical, isotropic growth.

    c)   Infinite planar interface between the untransformed matrix and the forming nuclei (capillarity approximation).

    d)   Neglecting collisions, interactions, and vibrations between neighbouring nuclei during the transformation process.

    e)   No compositional dependency on the nucleation and growth process.

However, many of these postulates have increasingly become questioned, not least due to the development of more advanced *in situ* techniques offering enhanced temporal and spatial acquisition capabilities of the nucleation phenomena. These techniques have revealed that nucleation may be far more complex than what is postulated by CNT alone, leading to many extensions of CNT coherently known as "non-classical" routes.[95] In essence, these routes depart from the one-step kinetic model of CNT, stating that nucleation may occur through a two-step mechanism instead.

6 Analytical Techniques

6.1 X-Ray Diffraction (XRD)

X-ray diffraction represents a non-destructive analytical technique that allows rapid characterisation of materials based on their crystallinity and phase content(s). While the technique is particularly suitable for analysing crystalline materials, it may also reveal the existence of an amorphous phase in the examined sample. Typically, this is indicated by the presence of a large "hump" in the diffractogram, particularly at lower diffraction angles.[109]

In XRD, a target sample is irradiated by a constant flux of electromagnetic radiation, typically X-rays, whose wavelength is similar in range to the interatomic distance of most crystalline materials.[109] The elastic interaction by scattering between the incoming X-rays and the electrons in the material leads to coherent destructive and non-destructive interferences originating from specific planes of atoms.[110,111] By gradually measuring the angle where constructive interference occurs, characteristic diffraction patterns are obtained, consisting of several peaks. These peaks' coherent position provides a fingerprint of the phase(s) present in the studied material, thus allowing for their qualitative characterisation.[111]

The specific angle where diffraction occurs is denoted as the Bragg angle (θ_B), and its relationship with the interplanar distance d_{hkl} is expressed by the well-known Bragg's law:

$$2d_{hkl} \sin \theta_B = n\lambda \qquad \textbf{(Eq. 10.)}$$

Where λ is the wavelength of the incident X-rays and n is an integer, representing a diffraction order.[109]

6.1.1 Structural Refinements

Besides the coherent peak positions in a diffractogram, their overall shapes and intensities also contain valuable information about the diffracting specimens found in the examined sample. Together with the actual diffraction pattern, this additional information allows complete characterisation of the sample based on several structural parameters, such as unit cell size, crystal symmetry, atomic positions and occupancy factors.[112] Thus, considering these parameters allows for a more rigorous depiction of what phases are present in the material, particularly when substantial overlaps between peaks exist in the obtained diffractogram. Typically, this can be done by structural refinements, where the recorded diffraction pattern is iteratively compared from a least-square method to a calculated (simulated) pattern.[112] The most commonly used method for this is arguably the Rietveld method, whose derivations and mathematics have been thoroughly described elsewhere.[113] Notably, in the Rietveld method, the peak intensities are bound to the atomic coordinates from a structure factor F_{hkl}, which can be expressed as[109,112]

$$F_{hkl} = \sum_{n=1}^{N} f_{n,z} \exp\left[2\pi i(hx_n + ky_n + lz_n)\right] \qquad \textbf{(Eq. 11.)}$$

where N is the number of atoms in the unit cell, h_x, k_y, l_z are the atomic coordinates for a given reflection in the form of Miller indices, and $f_{n,z}$ the atomic scattering factor, relating to the number of electrons of an atom with atomic number z.[109] However, in cases where it becomes challenging to identify the exact atomic coordinates of a studied phase, a complete Rietveld refinement cannot easily be made. These cases include, among others:

    I.   Thin films and coatings, where texturing and thickness may influence the obtained intensity values.

    II.   Larger unit cells, for example in cases of intergrowth formations.

    III.   Where significant antisite disordering may exist.

    IV.   Where excessive stacking faults and point defects are found in the material.

In these scenarios, alternative refinement methods are typically required, including the Pawley (or Le Bail) method. Contrary to Rietveld, these methods treat the peak intensities I_{hkl} as refinable parameters and thereby not bound to any atomic coordinates.[114,115] Therefore, in the Pawley method, the diffraction pattern is refined based on the unit cell metrics, peak intensities, d-values, and structure- and cell symmetries.[115,116]

Within this thesis work, the Pawley method has been used in **Paper I** to corroborate the presence of additional $Al_6Ti_2O_{13}$ and $Al_{16}Ti_5O_{34}$ phases in the synthesised coatings. The refinements were made in the software Topas (Bruker AXS).

6.2 X-Ray Photoelectron Spectroscopy (XPS)

X-ray Photoelectron Spectroscopy is a surface-sensitive technique that investigates the electronic configuration of elements, revealing details about their bonding characters and local chemical environments. Thus, its primary purpose is to provide qualitative information about what elements are present, how they are bonded, and what compounds they form. Typically, the technique is called XPS or ESCA (Electron Spectroscopy for Chemical Analysis). The working principle of this technique is based on the photoelectric effect, which describes how electrons are emitted from a material's surface if it becomes irradiated by a flux of electromagnetic radiation with sufficient energy, like X-rays.[117] The emitted electrons originate from characteristic and element-specific energy levels of the material, which can be resolved by using this technique. Consequently, XPS evaluates a photon-electron interaction where the emitted electrons – denoted as photoelectrons – are being measured. By knowing the energy of the incident electromagnetic radiation (hv), and measuring the kinetic energies of the photoelectrons (E_k), information about their binding energies (BE) can be obtained from the formula:[111,117]

$$E_B = hv - E_k - \Phi \qquad \textbf{(Eq. 12.)}$$

where Φ represents the escape energy (*i.e.* work function) required for an electron to leave the irradiated sample's surface. This value depends on the sample material's intrinsic properties and the instrumental features of the used spectrometer.[111] Commonly, the energetic values are given in units of electron volts (eV), where the binding energy BE and the kinetic energy E_k are inversely correlated, *i.e.* high binding energy means low kinetic energy, and *vice versa*.[117]

6.3 Hard X-Ray Photoelectron Spectroscopy (HAXPES)

Synchrotron radiation denotes a highly energetic electromagnetic radiation created when charged particles, travelling at velocities near the speed of light, are accelerating. Whereas a typical electron spectroscopic instrument operates in the kinetic energy range of 0–1400 eV,[117] synchrotron radiation allows photon energies up to several keV to be used (with preserved energy resolution requirements). The use of high energy radiation for XPS is commonly denoted as HAXPES (Hard X-ray Photoelectron Spectroscopy). Compared to XPS, HAXPES allows examining deeper into the material (*i.e.* nanometres instead of Ångströms). Additionally, HAXPES may allow otherwise inaccessible and lower-energetic core levels to be examined. The generation of synchrotron radiation typically requires large-scale research facilities to be used. In this thesis, HAXPES has been carried out at the Soleil synchrotron radiation facility, Saint-Aubin (Paris), using the end station of the Galaxies beamline at the in-vacuum U20 undulator source.

6.4 Raman Spectroscopy

Raman spectroscopy (hereafter referred to as "Raman") is a technique utilised to examine the vibrational response of materials, allowing structural information of the short-range bond arrangement as well as lattice modes to be gathered. The technique has certain resemblances with XRD, such as enabling phase identification based on a coherent peak signature. However, there are some critical differences between these techniques. First, Raman frequently uses electromagnetic radiation with larger wavelengths, from ultraviolet to infrared (*i.e.* ~300–1100 nm). Second, Raman collects the inelastic scattering from materials, whereas XRD focuses solely on the elastic scattering with constructive and destructive interference.[111] And lastly, in contrast to XRD, Raman can be used to examine local defects and phase-identify amorphous materials, which are significant advantages of this technique.

The working principles of Raman are the following. When electromagnetic radiation reaches a sample, it can cause a frequency loss for the outgoing scattered photons if the polarizability changes during the vibration of the samples' atoms. In solid materials, there are numerous ways that the atoms may vibrate, depending on their degrees of freedom which, in turn, depend on their spatial bonding characters. Each type of vibration response can also be grouped into specific modes (also known as Raman shifts/bands) having specific frequencies. By using a diffraction grating, each of these modes can then be separated in a spectrum, allowing characterisation of the material based on its coherent peak signature.[111]

In order for a material to give rise to a vibrational response in the first place, it must be Raman active. Essentially, Raman active means that a certain vibration must induce a disturbance of the electron cloud with a corresponding change in its polarizability. This criterion can mathematically be expressed as[111]

$$\left(\frac{\partial \alpha}{\partial q}\right)_{q=0} \neq 0 \qquad \textbf{(Eq. 13.)}$$

Where a is the polarizability and q is the atomic equilibrium position. Unfortunately, this condition is rarely easy to determine beforehand unless a group theoretical analysis of the symmetries for the expected vibrations is analysed. In a more practical approach, the response of different symmetries can be assessed by measuring reference samples. Without these references, however, it becomes challenging to foresee what type of modes will appear, particularly if symmetry-breaking defects are present in the examined material. Irrespectively, anisotropic bonding characters, weakly polar or non-polar bonds,[118] and covalent bonding characters are all known to typically give rise to strong Raman active signals from a material.[111] This also implies that Raman is exceptionally sensitive to any changes in the local bonding environment that may affect their Raman activities. Accordingly, a Raman spectrum may contain helpful information about subtle structural changes to the local bonding characters, including structural relaxations, lower coordination, and the presence of defects like vacancies and dislocations.

6.5   Microscopic Techniques

6.5.1   *Scanning Electron Microscopy (SEM)*

Scanning electron microscopy is routinely used to examine a sample's morphological and microstructural features, which provides essential information about the deposition process in the case of thin films and coatings. Because electrons have vastly shorter wavelengths than any visible light, the resolution limit of typical optical microscopes can be surpassed, allowing the study of features down to the nanometre-range level.[111] In the technique, a combination of several electromagnetic lenses and apertures focus an electron beam into a narrow beam spot that scans an illuminated surface, creating a rectangular raster image. By varying the settings of the lenses and apertures, combined with the beam's acceleration voltage and current, the size of the beam spot can be adjusted, allowing for an excellent depth of field with this technique. For example, SEM can quickly adapt and generate images between 20× to 100'000× magnification levels. Furthermore, the excellent depth of

field entails that three-dimensional topographical features of the scanned image can be distinguished.[111]

6.5.2 *Transmission Electron Microscopy (TEM)*

Transmission electron microscopy is a versatile technique encompassing several features that allow a deepened microstructural information of a sample to be gathered. The method has many similarities with SEM in the sense that they both use an electron beam to examine a sample. However, there are many critical differences between SEM and TEM. First, unlike SEM, TEM is typically operated with significantly higher acceleration voltages (*i.e.* greater than 100 kV), allowing magnification levels of up to 10^6 times to be reached.[111] Secondly, TEM frequently requires significant sample preparation before any investigations can be carried out. Predominantly, this involves thinning the sample to a thickness of less than 200 nm, which makes the sample electron-transparent and allows the electron beam to pass through to a fluorescent screen, thereby producing an image. Thinning of the sample is made through a combination of mechanical grinding and final microscopic milling by using an SEM instrument equipped with a focused ion beam (FIB). The FIB uses a flux of positively charged gallium ions to bombard and etch a site-specific area of the sample that is about to be studied. Lastly, while there are similarities between SEM and TEM in terms of their instrumental setups, the optical configuration of a TEM instrument is usually far more complex. A TEM instrument may incorporate several condenser-, objective-, intermediate- and projector lenses to control and focus the electron beam in a desired manner.[111]

One of the greatest advantages of TEM is that it allows unprecedented atomic resolution of the material at high magnification levels. This feature enables TEM to produce images where atomic planes and even individual atoms can be distinguished. This type of imaging is typically made by so-called high-resolution transmission electron microscopy (HRTEM), which investigates elastically scattered electrons and their relative phase shifts to produce a sample image.[111]

The inelastically scattered electrons can also be used to produce an image at a higher resolution. Frequently, this is made by using "high-angle annular dark field" imaging (HAADF). This imaging mode is susceptible to differences in atomic number; hence, it allows *z*-contrast on the atomic level of an imaged sample.[119]

6.6 Compositional Evaluations

6.6.1 Energy-Dispersive Spectroscopy (EDS)

Energy-dispersive spectroscopy is a rapid and reliable method to identify what chemical elements are present in a material and quantify their relative amounts. Typically, the technique is performed in an SEM equipped with a separate EDS detector. The electron beam in an SEM not only generates electrons from the sample used for imaging but may also generate characteristic X-rays from the elemental specimens in the sample, which the EDS detector collects. By plotting the relative intensities of these X-rays in a spectrum, characterisation of what elements are present in the sample can be done. Also, since the peak intensities directly relate to the amount of each element, the integrated intensities allow quantitative amounts of each elemental specimen to be obtained.[111]

6.6.2 Ion Beam Analysis (IBA)

Ion beam analyses denote a plethora of techniques that use a flux of ions to investigate the atomic concentrations and allow depth profiling to be made in materials.[120] These techniques go by a wide range of different acronyms; however, in this thesis work, RBS (Rutherford Backscattering Spectrometry), Elastic Backscattering Spectrometry (EBS), and Time-of-Flight Elastic Recoil Detection Analysis (ToF-ERDA) have been used.[121] Jointly, these techniques rely on the coulomb interaction between charged particles, where ions impinge on a target material and interact with its electrons and atomic nuclei, whereupon various charged particles are scattered from the sample.[122] The interaction with the atomic nuclei is typically regarded as totally elastic, preserving both momentum and kinetic energy, whereas the interaction with the electrons is inelastic, thus reducing the incident ion beam energy.[120,122] This energy reduction is known as the electron stopping power, defined by the energy loss per unit length (dE/dx) that occurs when ions travel within a material. In turn, this energy loss is dependent on the elemental-specific cross-section $\varepsilon(x)$, which can be expressed as[122]

$$\varepsilon(x) = -\frac{1}{\rho_a} \cdot \frac{dE}{dx} \qquad \textbf{(Eq. 14.)}$$

where ρ_a designates the atomic density. By knowing the incident ion beam energy and the scattering angle θ, elemental quantification and identification can be made based on kinematics and the so-called kinematic factor K_f:[122]

$$K_f \equiv \frac{E_1}{E_0} \qquad \textbf{(Eq. 15.)}$$

where E_0 and E_1 denote the ion beam energy before and after nuclei collision, respectively. The relation between K_f and the scattering angle is then given by[122]

$$K_f(\theta, M_1, M_2) = \left(\frac{M_1}{M_2 + M_1}\right)^2 \cdot \left(\cos\theta + \sqrt{\left(\frac{M_2}{M_1}\right)^2 - \sin^2\theta}\right)^2 \qquad \textbf{(Eq. 16.)}$$

where M_1 is the mass of the incident ion, and M_2 is the mass on which scattering occurs. Accordingly, by knowing the scattering angle, the energy of the ion beam and the incident ions' masses, the ratio $\left(\frac{M_2}{M_1}\right)$ can be obtained and plotted into an energy spectrum.[121]

The differences in the various types of ion beam techniques available lie in what type of incident ions are being used, their energy range, and what type of scattered particles are being collected. These factors add to the techniques' different strengths and limitations, thereby also influencing their main application areas.

RBS uses incidence ions of lower masses (typically He^+) that impinge on a sample with typical energies up to a few MeV. The technique then collects those ions from the beam that is elastically backscattered from the sample.[121] Because RBS is heavily dependent on the atomic cross sections, which scale with the atomic number of the elements, the technique becomes more suitable for probing elements with higher masses in the sample.[120]

In contrast, ToF-ERDA is more sensitive and suitable for investigating lighter elements in a heavier matrix. Typically, this technique uses incident ions with much higher energies (~100 MeV) and higher masses (*e.g.* O, Cl, I, Ag, Au)[122] than RBS. Also, unlike RBS, ToF-ERDA collects elastically recoiled atoms from the sample itself and does so in the forward direction (rather than backwards as in RBS).[120,123]

Since RBS and ToF-ERDA are based on the same kinematic principles but have different sensitivities for either heavier or lighter elements, the techniques complement each other. Thus, they are frequently employed together in an ion beam investigation. Nonetheless, while ToF-ERDA is typically more suitable for investigating lighter elements, the sensitivity in RBS for lighter elements can sometimes be increased by increasing the beam energy. While this carries a risk that the interaction no longer becomes purely coulumbic,[122] potentially yielding ambiguous results,[120] certain elements may actually have increased elastic resonances at higher beam

energies. For instance, such is the case of oxygen, which has an increased elastic resonance and thus increased sensitivity in RBS at 3.037 MeV incident energy. **Paper III** has exploited this feature to probe the oxygen content of $Al_xTi_yO_z$ coatings before and after annealing. Notably, RBS operating at these energy levels are sometimes referred to as EBS instead of RBS.

6.7 Theoretical Calculations

6.7.1 Density functional theory (DFT)

Density functional theory (DFT) is a computational technique to derive energy values for different structural configurations of materials and molecules. Its foundation is based on quantum mechanics and the Schrödinger equation, stating that a system's energy state can be defined based on the spatial motion of the electrons.[124] However, exact solutions to the Schrödinger equation only exist for a few very simplistic cases. For more complex and multibody systems, the many degrees of freedom for the electrons make the Schrödinger equation difficult, if not impossible, to solve.[125–127] DFT aims to alleviate this problem by reducing the number of variables needed to describe the electrons' positions. Unlike the Schrödinger equation, where the spatial location of the electrons is given by a linear combination of their wavefunctions (*i.e.* $\Psi = \Psi_1(\mathbf{r})\Psi_2(\mathbf{r})... \Psi_N(\mathbf{r})$),[125] DFT treats the electrons as an effective electron density, $n(\mathbf{r})$:

$$n(\mathbf{r}) = 2\sum_i \Psi_i^*(\mathbf{r})\Psi_i(\mathbf{r}) \qquad \textbf{(Eq. 17.)}$$

Where the asterisk indicates a complex conjugate. This approximation reduces the degrees of freedom to describe the system's electrons from 3N variables to 3 (where N denotes the number of electrons).[125]

In order to compare the energies of different configurations, a ground-state energy must first be determined. In DFT, this is made by an iterative calculation process that relies on two fundamental theorems that Kohn and Hohenberg initially developed in the 1960s.[128] These theorems can be stated as:[125]

I.   *"The ground state energy from Schrödinger's Equation is a unique functional of the electron density."*

II.   *"The electron density that minimizes the energy of the overall functional is the true electron density corresponding to the full solution of the Schrödinger Equation."*

The first theorem links a solution of the Schrödinger equation to the behaviour of the electron density, whereas the second one provides a strategy for finding this electron density. In DFT, this is typically done by solving a set of so-called Kohn-Sham equations,[129] consisting of three energy potentials and with the general appearance:[125]

$$\left[\frac{h^2}{2m} \nabla^2 + V(\mathbf{r}) + V_H(\mathbf{r}) + V_{XC}(\mathbf{r}) \right] \Psi_i(\mathbf{r}) = \varepsilon \Psi_i(\mathbf{r}) \qquad \textbf{(Eq. 18.)}$$

where $V(\mathbf{r})$, $V_H(\mathbf{r})$, $V_{XC}(\mathbf{r})$ represent different energy potentials. Notably, a solution to these equations is not easy to find but can be achieved through minimisation to the lowest attainable energy. Here, an iterative process is utilised where a test electron density $n(\mathbf{r})$ is used to calculate a wavefunction, which is then utilised to calculate another set of electron densities to compare with the initial one. If these densities match, then the ground-state electron density is reached, which may, in turn, be used as an energy reference in comparison with other electronic configurations.

In this thesis work, DFT has been used in **Paper III** to derive energies for the cationic antisite exchange disordering that is prominent in Al_2TiO_5 (including $Al_6Ti_2O_{13}$ and $Al_{16}Ti_5O_{34}$). Furthermore, DFT has been used to calculate the migration pathways of oxygen and its related vacancies in Al_2TiO_5, showing that these values are significantly lower than those displayed by the cations.

6.8   *In situ* Studies

In situ is a Latin phrase meaning "in place" and is a common designation used to indicate the studies of reactions or phase transformations "as they happen". Typically, the term is coupled with the experimental possibility of altering the experimental conditions in a controlled manner while still examining the material. Thus, *in situ* allows for capabilities to study dynamic processes and allow enhanced information to be gathered about reactions and phase transitions.

In this thesis work, there are four main techniques where in situ capabilities have been utilised to investigate the crystallisation process of the coatings. These are listed below:

- *In situ* XRD – to extract the crystalline volume fraction as a function of time to gain kinetic insights about the crystallisation of the $Al_xTi_yO_z$ coatings.
  (**Paper II**)

- *In situ* RBS – to investigate any compositional changes in the long-range ordering because of annealing and crystallisation.
  (**Paper III**)

- *In situ* HAXPES – to investigate changes in chemical shifts between the amorphous and crystalline states before and after annealing and crystallisation.
  (**Paper III**)

- *In situ* TEM – To visualise and explore the nucleation and growth processes and the following morphological evolution in real-time.
  (**Paper IV**)

7 Results and Discussion

7.1 Deposition of Al$_2$TiO$_5$ from Metalorganic Precursors

A general prerequisite in the formation of ternary and multicomponent oxides by CVD is the existence of an overlapping process window for the involved reactants, allowing them to interact favourably and synergistically during deposition. In **Paper I**, this feature is demonstrated in cases of metal alkoxides as precursors to achieve the ternary Al$_2$TiO$_5$ rather than any binary constituents during deposition. Also, the higher reactivity and adaptability of these reactants entail that phases, which are otherwise hard to reach by other synthesis approaches, can be fabricated at much-reduced temperatures and shorter timescales. As a general theme for this thesis, it is argued that a critical reason for this achievement is when kinetics – rather than thermodynamics – controls the overall synthesis conditions.

7.1.1 Process Window Optimisations

In order to explore the feasibility of combining metal alkoxides in a CVD process, the initial work was focused on finding optimal process parameters for the individual precursors, *i.e.* AIP and TIP. Since a surface-kinetic reaction regime is typically desired in CVD, which promotes dense and homogenous coatings, low pressures (1-2 Torr) and high carrier gas flow rates (900 sccm) in the reactor were generally adopted. Accordingly, the deposition process was optimised by varying the deposition zone temperatures and the evaporator temperature of the individual precursors.

Depositions using either precursor alone yielded binary oxide formations. Typically, the TIP precursor produced crystalline coatings corresponding to anatase at lower temperatures (400–600 °C), whereas rutile was formed at higher. The precursor demonstrated good volatility and adequate thermal stability during depositions. Reactor temperatures up to 1000 °C were used for this precursor, albeit the deposition zone shifted significantly towards the gas inlet with increasing deposition-zone temperatures.

Contrariwise, the AIP precursor showed much more limited thermal stability. For increasing temperatures, typically above 500 °C, significant homogenous nucleation

in the gas phase was noticed, depleting the precursor, and leading to porous coatings. Also, the coatings demonstrated limited-to-none crystallinity as-deposited, and after annealing *in vacuo* above 700 °C, γ-Al_2O_3 was typically obtained.

Based on initial XPS measurements, a too-low deposition temperature (*i.e.* below 400 °C) in the reactor zone yielded incomplete surface reactions, resulting in partly hydroxylated coatings. Thus, these early findings indicate that an optimum deposition temperature range exists for these precursors' combined usage, lying between 400–500 °C. In hindsight, the observations of hydroxyl entities in the coatings at lower deposition temperatures can be interpreted as a clue indicating that a shared growth mechanism for the used metal-organic precursors exists. As described later, this joint growth mechanism is critical in enabling the growth and formation of the ternary Al_2TiO_5-phase, rather than any binary constituents, when the AIP and TIP precursors are combined within the same deposition process.

7.1.2 Simultaneous Depositions using AIP and TIP

Table 3. List of used deposition parameters.

Pressure Range	1–2 Torr
Deposition Temperature	450 °C
Total Carrier Gas Flow Rates	900 sccm
Deposition time	1 h
Evaporator Temperature, TIP	50–70 °C (varied)
Evaporator Temperature, AIP	110 °C (fixed)

Investigations of the combined usage of AIP and TIP, whose process parameters are summarised in *Table 3* above, revealed that the Al : Ti molar ratio in the coating could be fine-tuned by varying the evaporator temperature – and hence the vapour pressure – of the more volatile TIP precursor. These compositional results, extracted from EDS, are compiled in *Figure 14*. Noticeably, a slight change in the heating temperature of the TIP evaporator leads to a drastic change in the Al : Ti ratio, which follows an exponential relationship. This is marked by the dashed line in the figure. A close-to-ideal (1.88) Al : Ti ratio with respect to the Al_2TiO_5 phase was obtained when the heating temperature of the evaporator was set to 54.7 °C.
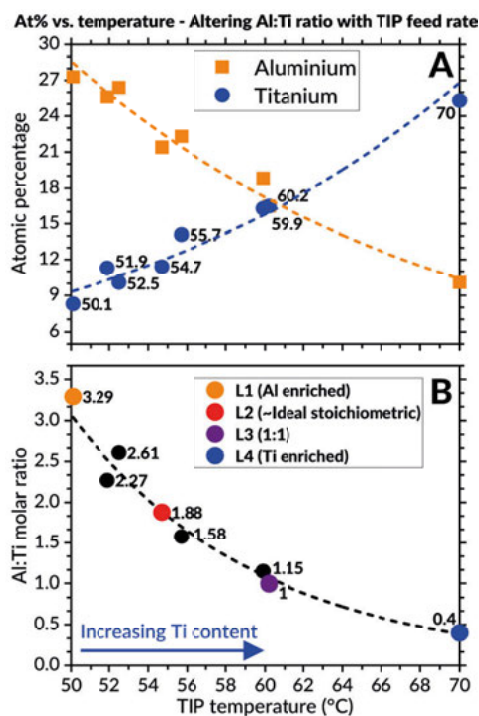
Figure 14. Compilation of EDS compositional data, showing in (A) the variation of aluminium and titanium content and in (B) the corresponding Al : Ti molar ratio in the deposited coating. Both graphs are plotted as a function of the TIP evaporator's heating temperature. Dashed exponential lines added for the guidance of trends.
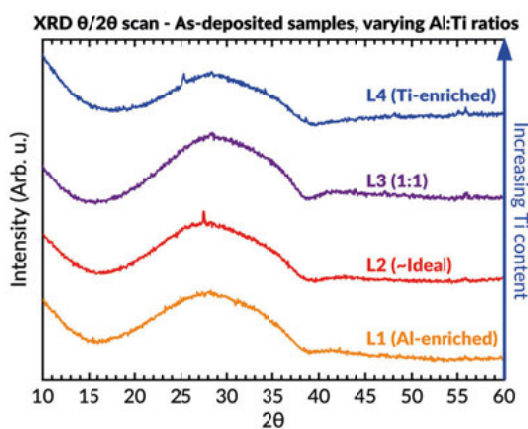
Figure 15. Diffractograms of as-deposited samples with different Al : Ti ratios.

In order to examine the role of composition on any phase formations in **Paper I**, four different sample stoichiometries were selected, which corresponded to Al-enriched, ~ideal stoichiometric, equimolar, and Ti-enriched.

Analyses of the phase contents in the as-grown films by XRD, which are shown in *Figure 15,* yield large asymmetric humps signifying the presence of an amorphous phase. Similarly, microscopic examinations of the coatings by top-view and cross-sectional SEM imaging revealed few deviating morphological features (*Figure 16*). The top-view image demonstrates smaller nano-sized globular domains, while the cross-section indicates dense coatings with no significant contrast fluctuations, which also agrees with TEM investigations (*Figure 17*). Thus, these findings found no deviating features due to compositional variations, and the coherent results indicate that the as-deposited coatings mainly consist of an amorphous phase.
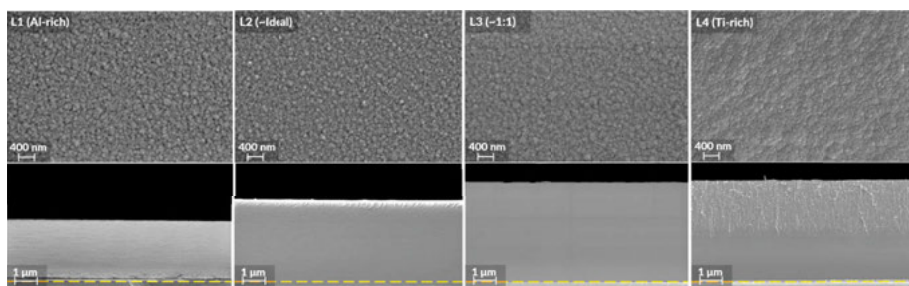
Figure 16. Plan view (top surface) and cross-sectional SEM imaging of the as-deposited coatings having various Al : Ti molar ratios. Yellow dashed line marks the interface to the underlying silicon substrate. Scalebar top row is 400 nm, scalebar bottom row is 1 μm. From left to right: Al-enriched, ~ideal, 1 : 1 and Ti-enriched.

Note: Compared tot the figure in the publication, the contrast and brightness have been increased in this thesis to enhance the visualisation of the surface features.
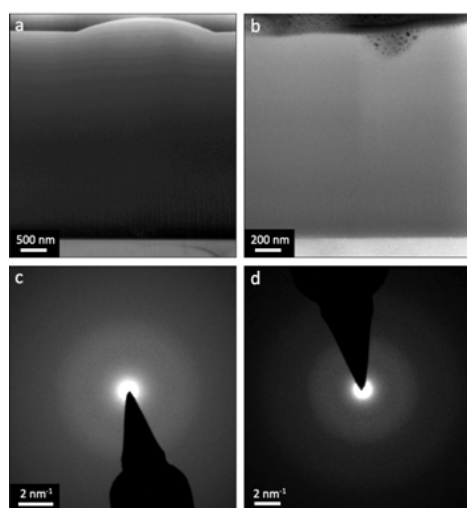
Figure 17. TEM and SAED of the Al-enriched (a)-(c) and ~ideal stoichiometric (b)-(d) samples, showing no diffraction contrast or pattern, indicating that the grown coatings are amorphous as-deposited.

7.1.3 Short-Range Al–O–Ti Bond Formations

Raman spectroscopy was used to further investigate the amorphous coatings' short-range features, whose results are displayed in *Figure 18*. Except for the two intense Raman bands at 520 and 970 cm^{-1} (including the possible shoulder at 1030 cm^{-1}), which originate from the underlying Si-substrate, all coatings displayed characteristic bands around 170; 230-300; 390-433; 615-670 and 793-871 cm^{-1}. The coherent positions of these bands agree to reference spectra for the Al$_2$TiO$_5$ phase.[40,130] Thus, beyond the previous structural notions about these coatings, these results show that
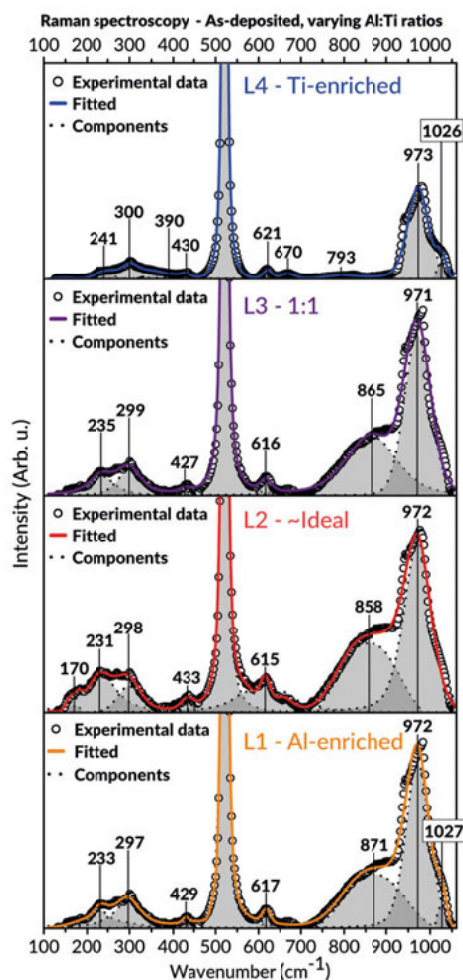
Figure 18. Raman spectra of as-deposited samples with different Al : Ti ratios. Characteristic modes corresponding to Al$_2$TiO$_5$ can be found in all samples. The intense bands at 520.5 cm and 970 cm^{-1} (including the possible shoulder around 1030 cm^{-1}) originate from the underlying Si-substrate. Certain modes are boxed for enhanced visibility.

they contain a high degree of Al–O–Ti bond assemblages on the short-range order, regardless of their overall Al : Ti ratios. In addition, the structural homogeneity of these bonds in the coatings can be further deduced based on the lack of an intense E_g-mode around $140 \, cm^{-1}$, belonging to TiO_2, for the examined compositions. Based on this observation, limited formation of binary constituents seems to occur in these compositional domains as part of the deposition process. However, it is essential to notice that binary phases may still form due to the annealing and crystallisation when the stoichiometry deviates from an ideal composition. As seen in *Figures 19* (XRD) and *20* (Raman), such is the case if the overall stoichiometry of the as-deposited coating is equimolar (1 : 1) or Ti-enriched, where anatase readily forms upon annealing and crystallisation.
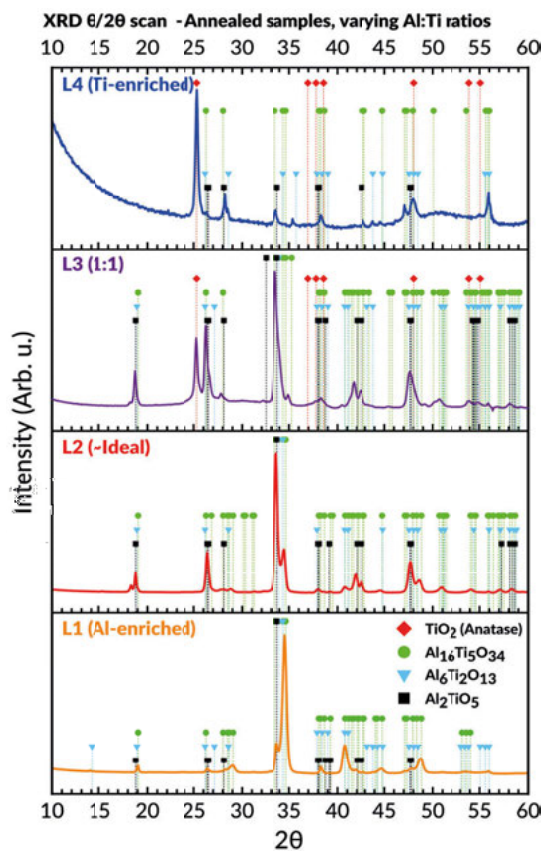
Figure 19. Diffractograms of samples annealed at 700 °C for 3 hours, marking all identifiable phases.
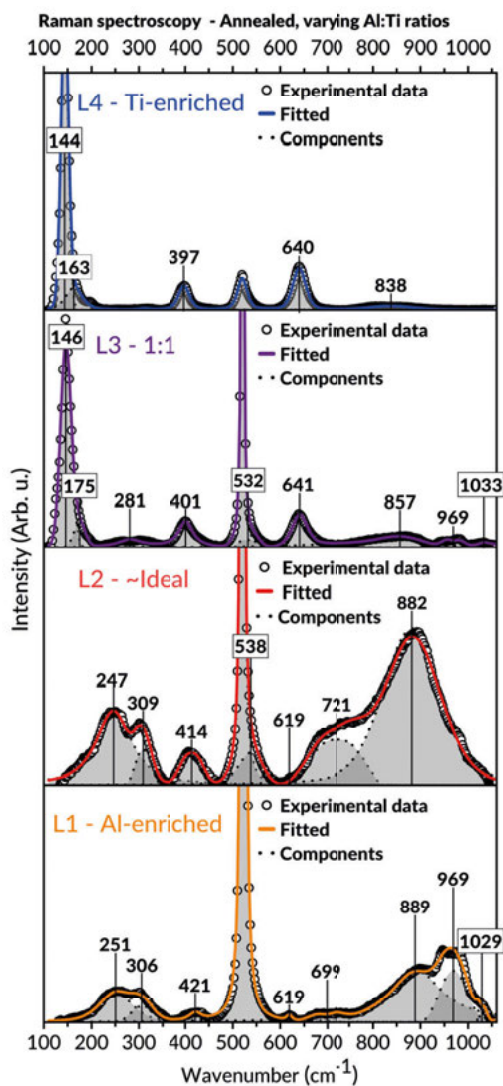
Figure 20. Raman spectra of annealed samples with different Al : Ti molar ratios. Only modes belonging to TiO_2 (anatase) can be distinguished in the Ti-enriched batch. The two bands at $520\,cm^{-1}$ and $970\,cm^{-1}$ (including the possible shoulder at $1030\,cm^{-1}$) originate from the underlying Si-substrate. Certain modes are boxed for enhanced visualisation.

7.1.4 Selective Kinetic Growth

Figure 15 illustrates a strong relationship between the heating temperature of the TIP evaporator and the coating's stoichiometries. Typically, an incremental increase in heating temperature yields increased Ti-contents in the coatings. Contrastingly, the SEM image series seen in *Figure 16* demonstrates that this increased flux from the TIP precursor does not yield a corresponding increase in the coating thickness, as the growth rate seemingly stagnates for higher TIP concentrations. This is apparent from the images representing the 1 : 1 and Ti-enriched stoichiometries. Altogether, these features suggest that the deposition process is not limited by the supply of gaseous precursors (*i.e.* mass-transport-control), but rather by the chemical reactions occurring on the surface. This indicates that the MOCVD process operates in a surface-kinetic-controlled regime, which is likely important to attain the Al_2TiO_5 phase during the growth of the coatings. This is explicated in the following sections, and also in **Paper I**.

To achieve the ternary Al_2TiO_5 phase rather than any binary constituents, the rate-determining steps for the involved reactants should essentially be similar to each other. Otherwise, the faster deposition process will dominate, leading to homogenous bond formations and a loss in stoichiometric film control. Essentially, this inference implies that the involved reactants should share common chemical features, decompose similarly and, above all, possess overlapping process windows. Interestingly, many of these similarities can be traced to AIP and TIP as precursors, not least from their usage in sol-gel[67] and shared decomposition routes from various thin film deposition techniques.[69,70] Moreover, in terms of CVD, it has been found that surface-active hydrolytic reactions typically govern the rate-determining step for these reactants.[131,132] The rate-limiting reaction step has also been ascribed to a second-order mechanism for AIP and TIP, respectively,[131] with similar activation energies (87 ± 7 kJ mol^{-1} for TIP, 76-98 kJ mol^{-1} for AIP)[131,133] in this regard. Consequently, this implies that a kinetic selectivity to obtain the ternary Al_2TiO_5 phase (rather than any binary ones) can be realised if these precursors are simultaneously combined in an MOCVD process.

7.1.5   Suggested Growth Mechanism

In order for TIP and AIP to transform into an oxide, their propyl ligands must first be removed. Given similar process conditions for the reactants during the CVD process, this will likely occur through thermal activation by pyrolysis.[134,135] As previously noted (*Section 4.3.3*, page 38), this route can occur by cyclic elimination and β-hydride elimination, ultimately leading to the formation of hydroxylated intermediates. During growth, these hydroxylated intermediates may, in turn, react with each other through surface-active condensation pathways, resulting in the formation of metal-oxygen bonds and the elimination of water as a by-product. As noted in the previous section, the rate of this process should be similar for the involved reactants, as this will favour *hetero-condensations* and M–O–M* bonds, rather than *homocondensations* and M–O–M bond assemblages. Interestingly, the latter statement implies that it also should, in theory, be possible to combine several alkoxide-based precursors into the same deposition process to obtain multicomponent CVD coatings, provided that the aforementioned criteria for kinetic selectivity can be met. The various steps presumed to be involved in the growth of $Al_xTi_yO_z$ coatings are visually represented in *Figure 21*.

Because each ligand position of the precursors may become hydroxylated and partake in the surface reactions, the proposed growth mechanism favours a large formation of Al–O–Ti bonds on the short-range order, which is supported by the Raman results. The structure of these bonds entails a mixing of the cations, which are also interlinked in a disordered oxygen framework. Thus, the proposed growth mechanism favours the formation of a homogeneous amorphous phase where the ions are likely near preferred lattice positions in a corresponding (ternary) crystalline state.[§§] In other words, only short diffusion distances are likely required to reach a possible crystalline state upon annealing. In terms of Al_2TiO_5, which may display significant cationic disordering in its crystalline structure,[23,24,36] this implies that only slight structural reorganisations, presumably from the oxygen framework, are required to spur nucleation and subsequent crystallisation events. Noteworthy, while this inference was initially presented in **Paper I**, the coherent findings from **Paper II** (nucleation-controlled crystallisation), **Paper III** (role of oxygen) and **Paper IV** (*in situ* TEM) support this view. Furthermore, the short diffusion distances, heterometallic bond assemblages, and strong structural homogeneities on the short-range level, all contribute to enabling the formation and crystallisation of Al_2TiO_5 at significantly reduced temperatures and timescales than comparable solid-state techniques. For instance, as shown in **Paper I**, crystalline coatings of Al_2TiO_5 could be obtained after three hours of annealing at 700 °C (973.15 Kelvin), which is below half the phase's melting point at 1860 °C (2133.15 Kelvin).

[§§] Here, the crystalline state represents a phase whose overall stoichiometry is closest to the amorphous one.

Consequently, these notions emphasise the advantages of the MOCVD technique and the simultaneous usage of alkoxide-based precursors to reach ternary oxide phases, and possibly also multicomponent phases (see further "Conclusions and Future Outlooks", Chapter 8, page 108). Moreover, it is an initial indication of the importance of nucleation – a kinetic phenomenon – to control and enable the crystallisation of such phases at reduced temperatures and timescales than comparable synthesis techniques. This is further explored in **Paper II**.
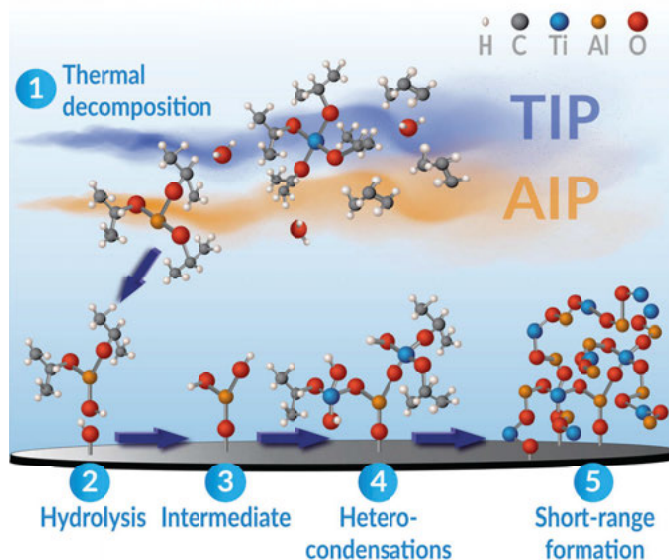
Figure 21. Schematic description of the reaction steps deemed involved for the growth of the Al_2TiO_5 phase, listing five main steps. In (1), the gaseous precursors of TIP and AIP decompose thermally to yield a hydroxylated compound by releasing propene groups. At (2), the hydroxylated compound chemisorbs to a surface, where two hydroxyl groups may react to form an oxy-bridge by releasing water as a byproduct. Hydroxylation and subsequent condensation may occur for all attached ligands (as illustrated from the intermediate in step (3). In (4), hetero-condensation occurs by attaching a hydroxylated TIP molecule to an already chemisorbed AIP molecule (or *vice versa*). Finally, in (5), multiple polycondensation reactions between AIP and TIP lead to the formation of heterometallic Al–O–Ti bonds, resulting in short-range order but a lack of long-range ditto, especially in the formed oxygen framework.

7.1.6 Unconventional Phases in the Al–Ti–O System

Figure 19 demonstrates the crystalline phases formed due to the annealing of the as-deposited amorphous coatings. Annealing was made *in vacuo* for 3 hours at 700 °C. As evident from this figure, all compositions demonstrated peaks assignable to the Al_2TiO_5 phase after crystallisation. The 1 : 1 and Ti-enriched stoichiometries also

demonstrated peaks assignable to TiO_2, indicating that this compositional region is outside the homogeneity range of the main Al_2TiO_5 phase. Along with the formation of Al_2TiO_5 even when the Al : Ti ratio is Al-enriched, these two observations are surprising, given that most pseudo-binary Al_2O_3–TiO_2 phase diagrams represent Al_2TiO_5 as a single line phase.[10] Nevertheless, a homogeneity range can also be induced through the presence of vacancies,[136–139] which constitute one of several scientific incentives explored in **Paper III**.

In addition to the peaks belonging to Al_2TiO_5 and TiO_2, the diffractograms also display peaks that could not be assigned to any expected phases in the Al–Ti–O system. This mainly concerns the Al-enriched and ~ideal sample stoichiometries, but some of these peaks can also be seen in the 1 : 1 stoichiometry.

Following the descriptions made in *Section 3.3*, Hoffmann *et al.* originally made similar observations and assigned these peaks to new phases in the Al–Ti–O system based on structural modelling and XRD refinements.[19,49,50,140] The stoichiometry of these phases was determined to be $Al_6Ti_2O_{13}$ and $Al_{16}Ti_5O_{34}$, where the latter phase is denoted as a structural intergrowth between Al_2TiO_5 and $Al_6Ti_2O_{13}$.[50] Thus, the observations of peaks assignable to these phases suggest that additional and unconventional $Al_xTi_yO_z$ phases are present in the as-deposited CVD coatings, particularly when the overall coating stoichiometry is either ~ideal or Al-enriched.

To corroborate the presence of these phases, whole-pattern refinements were carried out for the Al-enriched and ~ideal samples. For reasons described in *Section 6.1.1* on page 47, a Pawley refinement was used instead of a conventional Rietveld
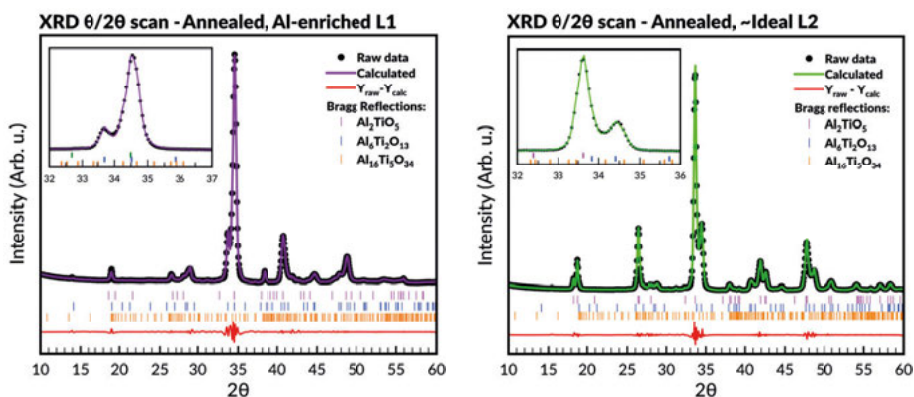
Figure 22. Pawley-refined diffractograms of Al-enriched and ~ideal stoichiometric samples.

refinement. The results are presented in *Figure 22*, which shows that the diffractograms can solely be described based on the presence Al_2TiO_5, $Al_6Ti_2O_{13}$ and $Al_{16}Ti_5O_{34}$. Therefore, these results indicate that several structurally related ternary Al–Ti–O phases crystallise during annealing. Also, they demonstrate that limited formation of binary constituents, like Al_2O_3 or TiO_2, occurs in the Al-enriched or ~ideal stoichiometric domains as part of the crystallisation process. This notion is also supported by the Raman results presented in *Figure 22*.

7.1.7   *The Role of Local Coordination in the Phase Formations*

Oxides are renowned for displaying a vast range of properties depending not solely on the composition but also on any deviations found in their local short-range arrangements.[141,142] Such deviations include, for example, tiltings, rotations and distortions of the polyhedron surrounding any metal cation. Raman spectroscopy is an excellent tool to investigate these features, which may provide clues explaining the co-formation of $Al_6Ti_2O_{13}$ and $Al_{16}Ti_5O_{34}$ after annealing in the samples.

Raman spectra for annealed samples with various Al : Ti ratios are shown in *Figure 20*, page *64*. Several interesting changes can be noticed by comparing the spectral features to the as-deposited amorphous state (*Figure 18* on page *62*). First, a broadening of the bands, accompanied by several peak shifts to higher frequencies, are seen in the annealed samples belonging to the Al-enriched and ~ideal samples. Such changes correlate with a weakened bond strength and an increased isotropic displacement factor. Combined, this suggests an overall reduced symmetry and a higher level of cationic mixing on the local short range after annealing. Presumably, such changes can be induced by rearranging the oxygen framework during crystallisation, leading to changes in the local coordination environments of the crystalline state. Notably, this image agrees with previous examinations made by Skala *et al.*, who demonstrated that structural changes, mainly to the M1 (4c) site, occurred in Al_2TiO_5 after annealing.[23]

Secondly, the characteristic and symmetric Raman band around 850-900 cm^{-1} is a distinguishing feature of tetrahedral coordination environments in aluminates and similar systems.[143–145] Likewise, the vibrational mode for this band has been assigned to Al–O bonds in tetrahedral configurations.[146] Thus, these results suggest that lower coordinating sites are present in the crystallised coatings after annealing, which also agree with the structural description of the $Al_6Ti_2O_{13}$ and $Al_{16}Ti_5O_{34}$ phase.

Coherently, these findings emphasise the role of local coordination in the co-formation of structurally related $Al_6Ti_2O_{13}$ and $Al_{16}Ti_5O_{34}$ phases during crystallisation, particularly within the Al-enriched and ~ideal stoichiometric domains. In hindsight,

the results can also be explained by the involvement and interaction of (oxygen) vacancies during crystallisation, leading to lower coordinating sites. This concept is elaborated in **Paper III**, where it is demonstrated that vacancies seem to be a key reason for the co-formation of the $Al_6Ti_2O_{13}$ and $Al_{16}Ti_5O_{34}$ phases.

7.2   Nucleation-Controlled Crystallisation

Examinations in **Paper I** emphasise the importance of the local short-range ordering in synthesising Al_2TiO_5 and its co-forming $Al_6Ti_2O_{13}/Al_{16}Ti_5O_{34}$ phases during depositions. In **Paper II**, this importance is also extended to the crystallisation behaviour of the coatings. Unlike most crystallisation processes, where diffusion typically limits the process, the coherent findings of this study indicate that the crystallisation process is nucleation-controlled. Although nucleation control does not necessarily mean "diffusionless" but rather that the nucleation process is rate limiting,[73] several factors in **Paper II** speak to diffusion's limited involvement in the crystallisation process. In particular, when the sample composition is close-to-ideal with respect to the main Al_2TiO_5 phase. The inference of a diffusionless transformation is also strengthened by subsequent studies, such as **Paper III**, which illustrates the involvement of oxygen and its vacancies during the crystallisation event.

As outlined in the following sections, a nucleation-controlled crystallisation process can be deduced based on the following observations in **Paper II**:

I.   Strong temperature dependency on the transformation rates, particularly for the initial transformations relating more to nucleation than growth.

II.   Large Avrami parameter n, especially when the stoichiometry is close-to-ideal or Ti-enriched.

III.   Highest apparent activation energies for the initial stages of crystallisation, especially for the ~ideal stoichiometry.

IV.   Strong structural resemblance between the amorphous and crystalline states of Al_2TiO_5, particularly when the stoichiometry is close-to-ideal.

A nucleation-controlled crystallisation process has several implications compared to a diffusion-controlled one. First, it favours the crystallisation of phases with the lowest nucleation barriers and an overall stoichiometry closest to a crystalline state.[72,83] Notably, these phases may not necessarily be the most thermodynamically stable ones.[147,148] Secondly, nucleation-control may open up new possibilities for controlling the microstructural development,[73,94] and hence the structure-property

relationship, for the emerging crystalline phase(s). This notion is explored in **Paper IV**.

7.2.1 Transformation Curves

The kinetics of the amorphous-to-crystalline transition for the coatings were examined in **Paper II** based on their intrinsic stoichiometries and the used annealing temperature. The coatings were annealed *in situ* in an X-ray diffractometer to achieve a time resolution of the crystallisation dynamics. Mechanistic details about the transition were then derived based on the "Avrami equation" (or JMAK-equation, see *Section 5.1.3*), Time-temperature-transformation (T–T–T) diagrams and evaluations of apparent activation energies. During measurement, the crystallisation dynamics were studied by the evolution of the most intense peaks typically appearing from the *ex situ* annealed diffractograms, *i.e.* between 30–36°. Deconvolution and fitting of this peak also revealed that it consists of three different Bragg reflections, each belonging to the Al_2TiO_5, $Al_6Ti_2O_{13}$ and $Al_{16}Ti_5O_{34}$ phases, respectively. By assuming that the adsorption coefficient is negligible in the coatings – which usually is the case for thin films and coatings – and that no significant change in texturing occurs during the phase transformation, the diffracted Bragg intensity I can, at any given time *t*, be treated according to:[149,150]

$$\begin{cases} I(t) \propto V_t & \text{(I)} \\ 0 \leq V_t \leq 1 & \text{(II)} \\ I_t^{norm} \equiv V_t^{norm} & \text{(III)} \end{cases}$$ **(Eq. 19.)**

where V_t denotes the transformed volume fraction of the crystalline phase(s) in the analysed sample. Since V_t is enclosed in $[0, 1]$, unity-based normalisation of the recorded intensity data must be made based on the equation[149]

$$I_t^{norm} = \frac{I_t - I_0}{I_\infty - I_0}$$ **(Eq. 20.)**

Thus, transformation curves for each emerging phase can be made by recording the peak intensity evolution of the Bragg reflections belonging to Al_2TiO_5, $Al_6Ti_2O_{13}$ and $Al_{16}Ti_5O_{34}$. Such transformation curves are compiled in *Figure 23* for various annealing temperatures and sample compositions.

First, in terms of the effect of annealing temperature, a strong temperature dependency is evident from the transformation curves, meaning that an incremental increase in isothermal heating yields drastically shorter times to reach the final crystalline product. The effect is most pronounced when the coating stoichiometry deviates from the ideal composition and is particularly noticeable when the coatings'

Ti-content increases. Notably, a strong temperature dependency on the transformation rates is signifying to a nucleation-controlled crystallisation process.[94]
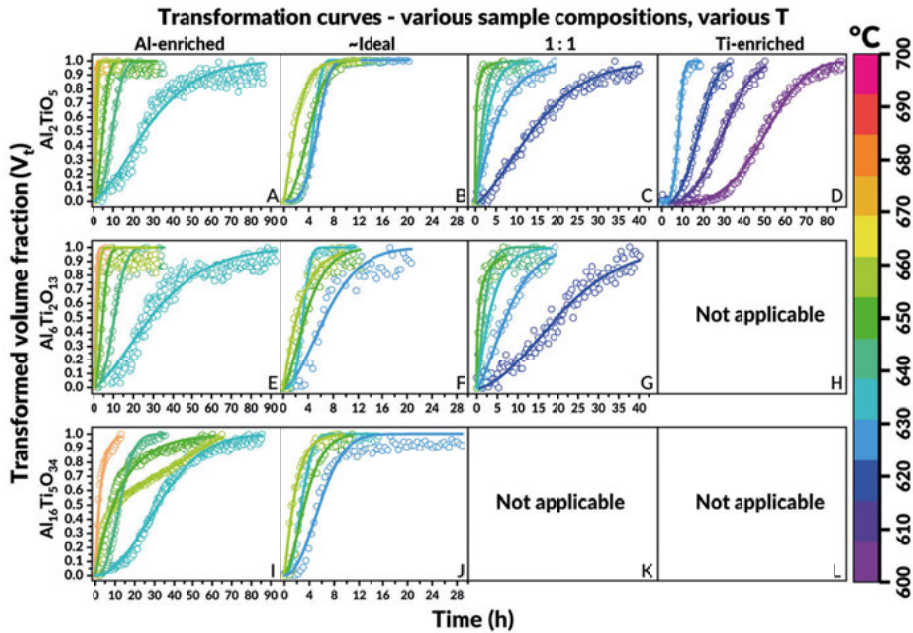
Figure 23. Amorphous-to-crystalline transformation curves, showing the influence of variations in isothermal annealing temperatures and chemical composition (Al–Ti ratios). Each horizontal row represents the crystallisation of the Al_2TiO_5, $Al_6Ti_2O_{13}$, and $Al_{16}Ti_5O_{34}$ phases. "Not applicable" means that any emerging peak assignable to $Al_6Ti_2O_{13}$ or $Al_{16}Ti_5O_{34}$ has too low intensity development to allow extraction of kinetic data in this region. Each transformation curve is fitted according to the Avrami (JMAK) equation.

Secondly, the effect of varying compositions can also be distinguished from *Figure 23*. In general, it is found that the crystallisation process is more sluggish and takes longer times to complete within the Al-enriched domain. Likewise, transformations require higher temperatures to both commence and finish when the aluminium content in the coating increases. In this regard, a continuous trend in the lowest achieved crystallisation temperature is observed when the Ti-content increases, suggesting that nucleation happens more preferentially in Ti-enriched environments. This notion is supported by subsequent observations and elaborated in *Section 7.2.7*.

7.2.2 Phase Fraction Analyses

The effect of temperature and composition on the phase formations can also be evaluated from their relative phase fractions. This is made by comparing each phase's intensity at the end of every annealing period. The results are compiled in the contour plot in *Figure 24*. Here, it is recalled that the equimolar 1 : 1 and Ti-enriched domains, besides any formations of Al_2TiO_5, $Al_6Ti_2O_{13}$, and $Al_{16}Ti_5O_{34}$, also form TiO_2 (anatase).

In the studied temperature range, it is apparent that the isothermal annealing temperature has little to no effect on any preferential phase formation in regard to the main Al_2TiO_5, $Al_6Ti_2O_{13}$ and $Al_{16}Ti_5O_{34}$ phases. This is expressed by the practically vertical contour lines seen in *Figure 24*. In contrast, the sample composition has a pronounced effect on the phase formations, and the $Al_{16}Ti_5O_{34}$ phase is more prevalent in the Al-enriched domain than the Ti-enriched one. Therefore, higher Al-content seems to correlate with the formation of $Al_{16}Ti_5O_{34}$, which agrees with Hoffmann *et al.*'s initial findings.[50]
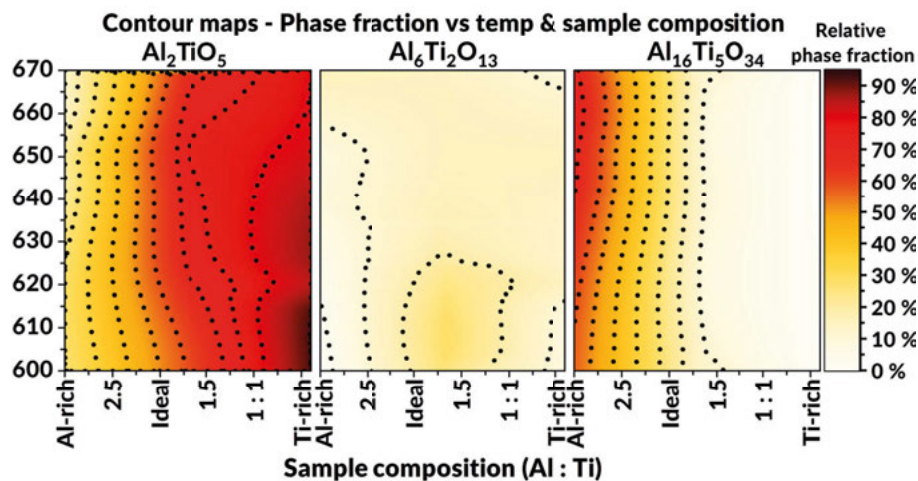
**Figure 24.** Contour maps showing the relative phase fractions (coloured) of the three phases Al_2TiO_5, $Al_6Ti_2O_{13}$, and $Al_{16}Ti_5O_{34}$ with variable isothermal annealing temperature and composition (Al–Ti ratio).

7.2.3 Avrami Parameters and Transient Nucleation Behaviours

Figure 25 compiles the extracted Avrami parameters (*ln K* and *n*) for the various sample compositions and phases. Theoretical descriptions of these parameters and the Avrami equation can be found in Section 5.1.3 on page 44.

As a general trend, an inverse correlation between *ln K* and *n* can be noticed. When the kinetic parameter *n* diminishes, the corresponding value of *ln K* increases. Thus, a lower dimensionality of crystallisation relates to a higher transformation rate and a more heterogenous, confined character of the transformation. Also, similar to the transformation curves, the value of *n* changes strongly with both the annealing temperature and sample composition. The lowest values of *n* are found in the 1 : 1 domain, whereas the ~ideal and Ti-enriched demonstrate the highest, particularly at lower annealing temperatures. Notably, high values of *n* indicate an unconstrained isotropic nucleation behaviour happening homogenously during the amorphous-
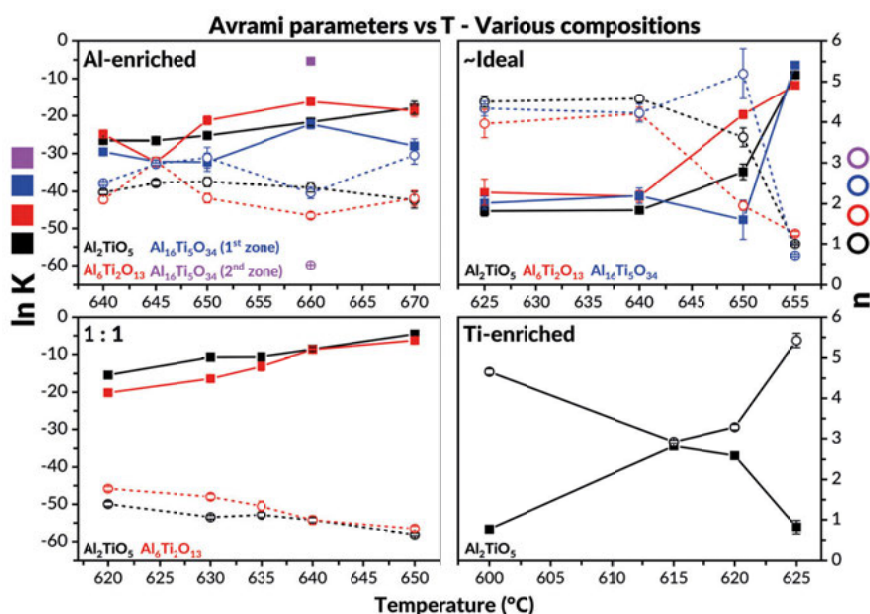
Figure 25. Derived kinetic parameters (ln K and n) for various Al–Ti ratios. Black, red, and blue lines denote values belonging to the Al_2TiO_5, $Al_6Ti_2O_{13}$, and $Al_{16}Ti_5O_{34}$ phases, respectively. The purple colour illustrates kinetic parameters derived from the secondary regime when Al-enriched samples are annealed at 660 °C (see *Section 7.2.8 on page 82* for details). Values of ln K are expressed with a boxed (▪) symbol, and n is expressed with a circular (○) ditto. Certain error bars are found within the plot symbols. The error bars represent the calculated standard deviations for the linear fitting of the corresponding phases' Avrami plots, found in the supplementary material of **Paper II**, *Figures S 13-16*.

to-crystalline transition.[102–105] Moreover, it indicates a time-dependent (transient) nucleation behaviour,[102–105] where nuclei emanate from small sizes.[82,103,151] Thus, this further emphasises nucleation's role during the crystallisation of these coatings. In that regard, it is worth mentioning that a transient nucleation behaviour is also indicated for the ideal stoichiometric coatings in the subsequent *in situ* TEM study made in **Paper IV** (Section 7.4.3 on page 100). In this section, the possible implications of this behaviour are further explained and linked to the results of **Paper III**.

7.2.4   Time-Temperature-Transformation (T–T–T) Diagrams

Based on the transformation curves in *Figure 23*, T–T–T diagrams can be made, shown in *Figure 26*. The three border lines in each window represent the time required to reach 5, 50 and 99 % transformed volume fractions for each sample composition and phase.
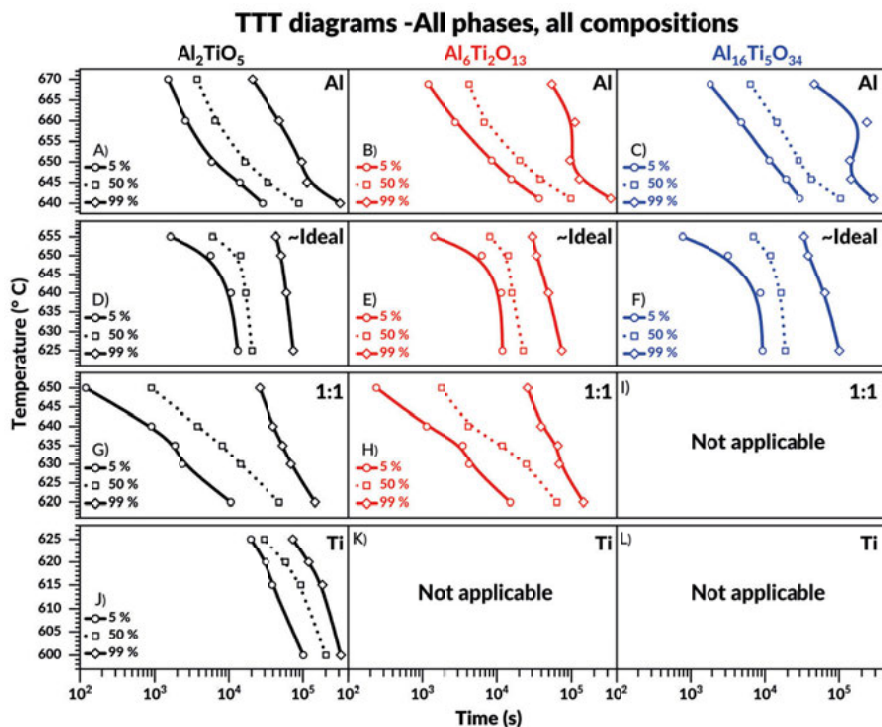
Figure 26. T–T–T diagrams showing the formation of Al_2TiO_5 (black), $Al_6Ti_2O_{13}$ (red), and $Al_{16}Ti_5O_{34}$ (blue) for various Al–Ti stoichiometries. "Not applicable" means that any emerging peak assignable to $Al_6Ti_2O_{13}$ or $Al_{16}Ti_5O_{34}$ has too low intensity development to allow the extraction of kinetic data in this region.

In essence, these diagrams highlight the strong temperature dependency seen on the transformations, particularly in the 5 % borderline where the nucleation process essentially dominates. In contrast, the time to reach the 99 % level remains almost vertical, especially for the ~ideal composition. This implies that the mechanisms controlling the latter stages of transformation are virtually unaffected by the increase in annealing temperature. In consequence, the strong temperature dependency of the transformation can be traced to the initial events of the crystallisation, namely, to the events predominantly relating more to nucleation, rather than growth by diffusion.

7.2.5 *Apparent Activation Energies*

During isothermal crystallisation, the time required to reach a certain volume fraction (t_x) frequently relates to the annealing temperature by an Arrhenius relationship.[152] Mathematically, this can be expressed according to[152,153]

$$t_x = t_0 \cdot \exp \frac{E_a^{app}}{RT} \qquad \textbf{(Eq. 21.)}$$

where t_0 is a pre-exponential constant, R is the universal gas constant and E_a^{app} the apparent activation energy of crystallisation. Hence, a plot of *ln t_x* vs *1/T* typically yields a straight line whose slope relates to the apparent activation energy at different stages of the crystallisation process. Arguably, the term "apparent" is essential to include, meaning that the activation energy equals a weighted average of all the standard-state enthalpies involved during the transition.[154] In terms of crystallisation, nucleation and growth are the main processes involved. Therefore, E_a^{app} incorporates the energetic contribution from both of these processes. However, at the earliest stages of crystallisation, the transformation is predominantly governed by nucleation, so that E_a^{app} relates more to the barrier of nucleation.[155] Similarly, at the end of the crystallisation process, where nucleation typically has ceased, E_a^{app} relates more to the barrier of growth.[155] Accordingly, this treatment of the apparent activation energy allows a formalised decoupling of its energetic contributions at the earliest and latest stages of crystallisation.

Local E_a^{app}-values for different volume fractions belonging to Al_2TiO_5, $Al_6Ti_2O_{13}$ and $Al_{16}Ti_5O_{34}$ are plotted for the four evaluated sample compositions in *Figure 27*. Generally, the equimolar sample composition displayed the highest calculated E_a^{app} values, whereas the ~ideal composition showed the lowest. This notion is further emphasised in *Figure 28*, displaying the average activation energies for the various

phases and sample compositions as a bar diagram. Except for the Al-enriched composition, the highest local E_a^{app}-values are typically found during the beginning of
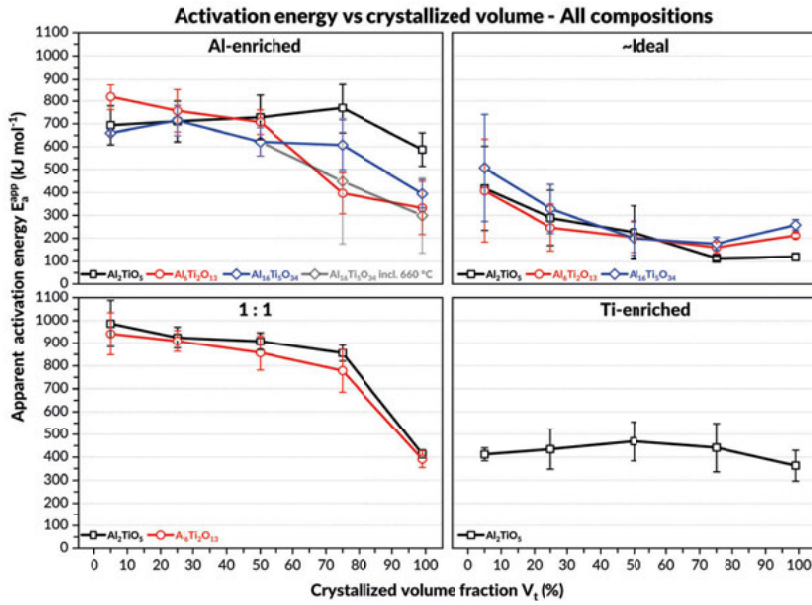
Figure 27. Local apparent activation energies (E_a^{app}) derived at different crystallisation stages and various Al–Ti sample ratios. The grey extension line seen in the Al-enriched domain relates to $Al_{16}Ti_5O_{34}$ peculiar growth behaviour displayed at this temperature, which is further explained in *Section 7.2.8*. The error bars represent the calculated standard deviations for the linear fitting of the corresponding Arrhenius plots, found in the supplementary material of **Paper II**, *Figure S 17*.
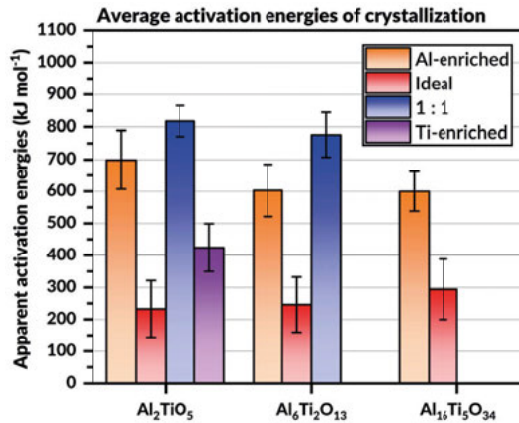
Figure 28. Bar diagrams showing the averaged apparent activation energies of crystallisation for various Al–Ti ratios and emerging phases. Error bars represent the standard deviations for the mean E_a^{app}-values calculated for each phase and composition.

crystallisation, and diminish as the transition proceeds. This effect is most pronounced for the ~ideal stoichiometric case, which showed the lowest general E_a^{app}-values, and also the lowest E_a^{app} overall, which was reached after 75 % volume fraction transformed: $112 \pm 9 \, \text{kJ} \times \text{mol}^{-1}$. Noteworthy, this value is about half the magnitude of typical E_a^{app}-values relating to diffusion in amorphous alloys.[90]

The fact that the E_a^{app}-value is highest at the earliest stages of crystallisation suggest that nucleation is the rate-determining event, thereby also indicating a nucleation-controlled crystallisation process. Similarly, a temperature-dependent nucleation rate can be deduced from the increased uncertainty (and reduced linearity of the Arrhenius plot) for the 5 % level of the ~ideal stoichiometry. Such behaviours have previously been associated with a nucleation-controlled crystallisation process.[71]

7.2.6 The Role of Configurational Entropy in Nucleation-Controlled Crystallisation

Configurational entropy (S_{config}) is a thermodynamic parameter commonly ascribed to Al_2TiO_5 thermal stability at elevated temperatures, typically above 1280 °C.[35] Based on deductive reasoning made in **Paper II**, it can also be demonstrated that configurational entropy plays a vital role in the crystallisation dynamics when the process is nucleation-controlled. Specifically, the term can be used to rationalise the apparent activation energies found in *Figure 28*, as explained in the following paragraphs.

It is observed that the examined amorphous samples, regardless of their intrinsic compositions, crystallise below half the melting temperatures of any crystalline counterpart. At such low temperatures, the level of supercooling is extensive.[90] Therefore, the total driving force for nucleation (ΔG_n) becomes the dominant parameter influencing the crystallisation process from a thermodynamic point of view. Analogous to *Equation 6* in *Section 5.1.2*, this can be accentuated by an expression of the steady-state nucleation rate I_{st}, given as[77,79]

$$I_{st} = I_0 \cdot \exp\left(-\frac{W^* + \Delta G_D}{k_B T}\right) \qquad \textbf{(Eq. 6.)}$$

Where I_0 is a pre-exponential factor, k_B is the Boltzmann's constant, W^* is the barrier of nucleation, whilst ΔG_D is the kinetic ditto. Assuming the formation of a spherical nucleus with a critical radius r^*, W^* can be expressed according to *Equation 5*.[77,79] For the reader's convenience, this equation is reproduced below:

$$W^* = \frac{16\pi\gamma^3}{3\Delta G_n^2} \qquad \textbf{(Eq. 5.)}$$

where γ represents the interfacial energy. Notably, γ is frequently deemed as temperature-independent, not least within the CNT framework.[79] Therefore, the thermodynamic driving force for nucleation increases with decreasing temperature, and a corresponding decrease of W^* can be expected. If the crystallisation process is nucleation-controlled, then any factors that may influence ΔG_n will profoundly affect W^* and thus the overall crystallisation behaviour. Such behaviour is observed by the strong temperature dependence on the crystallisation rate, especially for the earliest transformation stages and the ~ideal composition.

Besides the influence of temperature, the sample composition also has a significant influence on ΔG_n based on its intrinsic entropy term. Since ΔG_n represents the free-energy difference between the crystalline phase and the supercooled (amorphous) state,[79] one can write (*Equation 4*):

$$\Delta G_n = \Delta H_{cryst} - T\Delta S_{cryst} \qquad \textbf{(Eq. 4.)}$$

Where ΔH_{cryst} represents the total enthalpy of crystallisation and ΔS_{cryst} the change in entropy between the amorphous and crystalline states. In this regard, the entropy term also relates to a chemical potential μ_i of the system, which in turn depends on the number of particles N_i present for a particular element i:[156]

$$\mu \equiv -T\left(\frac{\partial S}{\partial N_i}\right)_{U, V} \qquad \textbf{(Eq. 22.)}$$

Per definition, the number of particles N_i relates to the molar composition.[157] Thus, it follows that a corresponding change in Al : Ti molar ratio would influence the entropy term, and hence also ΔG_n and the energies required to drive the amorphous-to-crystalline phase transformation. This is reflected in the E_a^{app}-values viewed in *Figures 27* and *28*.

During an amorphous-to-crystalline transition, there are predominantly two main contributions to the entropy term:[158] vibrational entropy (S_{Vib}) and configurational entropy (S_{config}). The vibrational entropy is generally assumed to increase linearly with temperature, thus favouring nucleation's overall thermodynamic driving force.[158] Therefore, the difference in configuration entropy (ΔS_{config}) between the

amorphous and crystalline states marks a significant part of the excess entropy found in the system. Because the total entropy of the amorphous state can never be less than the crystalline one, ΔS_{config} adopts negative values.[71] This implies that major structural differences between the amorphous and crystalline state yield higher ΔS_{Config}-values and a corresponding decrease of the driving force, as per *Equation 4*. Similarly, a strong structural resemblance between the amorphous and crystalline states would reduce ΔS_{Config},[71] hence favouring the overall thermodynamic driving force. In the case of Al_2TiO_5, $Al_6Ti_2O_{13}$ and $Al_{16}Ti_5O_{34}$, one can generally expect an extensive structural resemblance between these phases and between their amorphous and crystalline states. This inference is based on three central aspects. First, all phases readily display cationic disorder in their crystalline states (as shown by many previous authors[23,24,35,36,49,50]), meaning that few crystallographic constraints are imposed on the cations. Second, they share similar crystal system and space groups, with the main difference being the extension of the *c*-axes for $Al_6Ti_2O_{13}$ and $Al_{16}Ti_5O_{34}$ compared to Al_2TiO_5.[50] Lastly, previous Raman investigations (**Paper I**) show that an extensive short-range ordering of Al–O–Ti exist in the amorphous state, which is a prerequisite for the transition to the crystalline (ternary) counterpart.

In the case of the main Al_2TiO_5 phase, the most substantial structural resemblance between the amorphous and crystalline state is realised when the elemental composition is closest to the ~ideal stoichiometric case. In that scenario, $S_{config}^{crystal}$ and S_{config}^{amorph} becomes the most alike, so that their corresponding ΔS_{config}-value becomes closest to – though not equal to – zero. Essentially, this situation represents a theoretical maximum in the thermodynamic driving force of nucleation, as most of the residual ΔS_{config} then diminishes, and ΔG_n becomes mainly governed by the enthalpy term, ΔH_{cryst}. This inference agrees with the calculated apparent activation energies in *Figure 28*, where the ~ideal stoichiometry demonstrated the lowest averaged values.

Furthermore, because ΔH_{cryst} predominantly relates to the energies needed for breaking and redistributing chemical bonds during crystallisation,[71,148] the entropic condition above implies that only minor readjustments of the local short-range should be required to initialise, and potentially finalise, the overall long-range order. In other words, this speaks to a potential diffusion-less transition during crystallisation, particularly within the ~ideal stoichiometric domain. Although this insight can be inferred from **Papers I** and **II**, the possibility of a diffusion-less transition is also further examined in **Papers III** and **IV**. In these two subsequent studies, a series of

in situ analytical techniques and theoretical calculations also support that the crystallisation process occurs through a displacive (diffusionless) transition. These results are further expounded in *Section 7.3*.

As a final remark, the aforementioned entropy considerations can also be invoked to explain when the lowest thermodynamic driving force of nucleation is reached, resulting in the highest nucleation barrier. As seen in *Figure 28*, this situation occurs within the equimolar 1 : 1 domain. Structurally, this stoichiometry best represents a situation where there is no permutational preference in the cationic configurations, that is, all interstices are treated as symmetrically equivalent.[35,159] In that case, the maximum randomness in possible configurations is achieved,[159,160] resulting in the maximum possible S_{config} for the amorphous state. This translates to the largest excess ΔS_{config} and, thereby, the highest theoretical barrier of nucleation, as per *Equations 4* and *5*.

7.2.7   *Influence of Titanium on the Nucleation Behaviour*

The previous section illustrates how configurational entropy has an important role in the dynamics of nucleation-controlled crystallisations. While the term can be used to rationalise the apparent activation energies when the stoichiometry is ~ideal or equimolar, it cannot unequivocally separate the individual (chemical) contributions from the elements involved. Irrespectively, the coherent results of **Paper II** highlight the elemental influence of titanium on the nucleation process.

Foremost, the obtained E_a^{app} are consistently lower in the Ti-enriched regime compared to the Al-enriched ditto, suggesting that nucleation, from a thermodynamic perspective, is more preferred when the titanium content in the coatings increase. Also, this notion is strengthened by noting that the Ti-enriched samples consistently showed the lowest annealing temperatures required to initiate nucleation. In that regard, it is also interesting to note the similarities between the kinetic behaviour of the Ti-enriched and ~ideal stoichiometries at lower annealing temperatures. Both of these sample stoichiometries demonstrated high dimensional values of their Avrami parameter *n* (see *Section 7.2.3* on page 74), implying a transient nucleation behaviour.[102–105] In turn, this also indicates that nucleation emanates from small nuclei sizes[82,103,151] which, in the framework of CNT, suggest a large driving force of nucleation.[90] Moreover, this observation agrees with the apparent activation energies obtained for the Ti-enriched and ~ideal stoichiometric samples, which were generally found to be the lowest (*Figure 28*). Therefore, these observations suggest that a joint nucleation behaviour may exist where titanium, as an element, plays an essential role in the nucleation of Al_2TiO_5, and possibly $Al_6Ti_2O_{13}$ and $Al_{16}Ti_5O_{34}$ as well.

7.2.8 Secondary Nucleation Effects

Noticeable from the transformation curves in *Figure 23(I)*, a peculiar growth behaviour is observed from the $Al_{16}Ti_5O_{34}$ phase in the Al-enriched domain when the samples are annealed at intermediate temperatures (*i.e.* 660 °C). Initially, the transformation curve follows a similar trend to the other transformations. However, after around 40 % transformed volume fraction, the slope of the transformation curve declined markedly, reaching a linear state. Also, even after prolonged annealing durations of 65 h, the transition of this linear region does not cease. Markedly, such behaviour deviates from the conventional sigmoidal-shape crystallisation curves, where termination effects ensue at the later transition stages due to the exhaustion of the amorphous matrix (and increasing impingements between the formed crystalline domains).[101,161] In light of this, the deviating behaviour at the later transition stages suggests that these effects are either absent or, more likely, lagging.

Deviating features for this particular transition are also expressed throughout the kinetic results presented in **Paper II**. For instance, two linear regions with markedly different slopes were found when extracting the Avrami parameters for the transition of the $Al_{16}Ti_5O_{34}$ phase in the aforementioned case. The subsequent transformation process, represented in the purple colour of *Figure 25*, occurs at a much higher rate (larger *ln K*) and is more confined (low *n*) than the initial process. This indicates that the transformation behaviour changes during crystallisation, and that several mechanisms are likely involved in the amorphous-to-crystalline transition.

The continuous transformation of the Al-enriched sample annealed at 660 °C also leads to increased uncertainty when deriving apparent activation energies. This is particularly the case if the 660 °C transition is included in the primary dataset when calculating these energies, which is represented by the grey extension line in *Figure 27*. Essentially, this interpretation infers that the entire transition can be explained from a single first-order mechanism involving nucleation and growth. However, such an interpretation contradicts the derived Avrami parameters, which suggest that several mechanisms contribute to the crystallisation dynamics. Likewise, if the peculiar linear transition seen at 660 °C is regarded as a subsequent event, hence excluding it from the primary process' dataset, an improved linearity and reduced statistical error of the Arrhenius plot is obtained. This outcome is represented in the blue line in *Figure 25*. Accordingly, this signifies that several mechanisms may be involved in forming $Al_{16}Ti_5O_{34}$, particularly at intermediate annealing temperatures in the Al-enriched domain.

In an effort to understand the causes of these features, a plot of measured *2θ*-values *versus* time was made, which is represented in *Figure 29*. As seen from this figure, the peak positions for the $Al_{16}Ti_5O_{34}$ phase continuously shift to lower values as the crystallisation process progresses. Meanwhile, the peak positions for the $Al_6Ti_2O_{13}$ phase
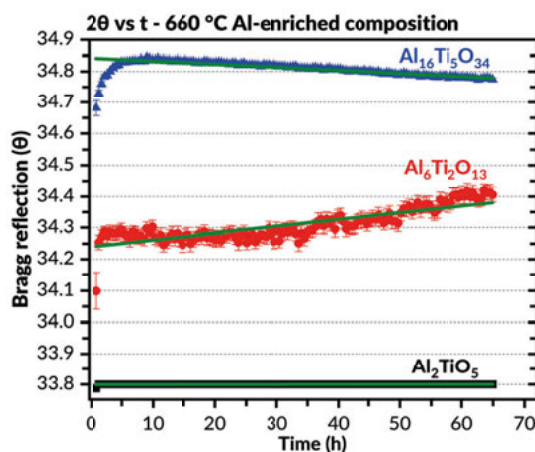
Figure 29. 2θ *vs* time plot illustrating a continuous shift in 2θ-values between $Al_{16}Ti_5O_{34}$ and $Al_6Ti_2O_{13}$ for Al-enriched samples annealed at 660 °C. The green line marks trends in data progression.

continuously shift to higher values, whereas no apparent change occurs for the Al_2TiO_5 phase. Hence, this figure suggests a continuous increase in unit cell parameters for the $Al_{16}Ti_5O_{34}$ phase, while the same values for the $Al_6Ti_2O_{13}$ concurrently diminish. In other words, this observation indicates that an intertwined relationship exists between these two phases, and that the $Al_{16}Ti_5O_{34}$ phase may be forming at the expense of the $Al_6Ti_2O_{13}$ phase.

Considering these findings, it is noted from the literature that conditions of high supersaturations may cause intriguing crystallisation phenomena due to the competing interest of nucleation and growth.[84] This includes, for example, altered microstructural morphologies during the amorphous-to-crystalline transition and novel phase formations, particularly when diffusion is impeded.[73,94] Notably, such crystallisation conditions are found in the Al-enriched samples annealed at intermediate temperatures.

In addition, assuming titanium has a vital role in any nucleation events (as explained in the preceding section), the incorporation of titanium into the formed crystalline domain will slowly deplete the element from the amorphous matrix as the crystallisation front progresses. Ultimately, this will lead to a continuous increase in the amorphous matrix's viscosity, slowing down any possible atomic transport.[77,94] In such scenarios, it also becomes more viable for the crystallisation to progress into other possible and energetically-less demanding routes. This includes structural relaxations, wherein bond angles and distances are shifted to adapt to newly exposed energy landscapes.[71] Notably, such relaxations are known to occur among amorphous materials,[97,162] and the presence of such in the $Al_xTi_yO_z$ samples can be inferred based on the Raman results from **Paper I**. Furthermore, due to the structural

homology between the amorphous and crystalline states, and also between Al_2TiO_5, $Al_6Ti_2O_{13}$ and $Al_{16}Ti_5O_{34}$, such relaxations can induce secondary nucleation events wherein any of these phases may be formed.

It should be noted that the term "secondary nucleation" is an established process exhibited among certain crystallisation events that are distinct from the process of primary nucleation (which may also yield the Al_2TiO_5, $Al_6Ti_2O_{13}$ and $Al_{16}Ti_5O_{34}$ phases). Secondary nucleation bears many similarities with heterogenous nucleation; however, unlike classical heterogeneous nucleation, where a unitary phase forms on itself, secondary nucleation may also lead to new possible structures and phase formations.[84] Consequently, it is hypothesised that the possibilities of structural relaxations and secondary nucleation events may be a reason for the continuous transformation of $Al_{16}Ti_5O_{34}$ in the Al-enriched domain during annealing at intermediate temperatures.

Nevertheless, secondary nucleation cannot wholly explain the continuous development of $Al_{16}Ti_5O_{34}$, rather than any other possible phases, in the Al-enriched domain. In other words, this suggests that additional processes are involved in this phase's formation, a perception that is also supported by *Figure 29*, where $Al_{16}Ti_5O_{34}$ progressively becomes larger while $Al_6Ti_2O_{13}$ simultaneously diminishes. Given the occurrence of secondary nucleation, this observation can be explained by the process of Ostwald ripening. Essentially, Ostwald ripening can be invoked to explain how small nuclei of $Al_6Ti_2O_{13}$ – formed by possibilities of secondary nucleation – may dissolve and become incorporated into surrounding, pre-existing grains of Al_2TiO_5, allowing a continuous growth and formation of the $Al_{16}Ti_5O_{34}$ phase. Markedly, this explanation complies with the structural description of $Al_{16}Ti_5O_{34}$, which is given as a combined (intergrowth) structure of Al_2TiO_5 and $Al_6Ti_2O_{13}$.[50] In addition, such mechanism is supported by the Avrami parameters found from the second regime (*Figure 25*), where the low dimensional values of *n* indicate a surface-mediated and heterogenous transformation.

Consequently, two possible mechanisms can be assigned to the formation of the $Al_{16}Ti_5O_{34}$ phase. One, where the phase nucleates directly from the amorphous matrix through primary nucleation. And two, where the phase is formed through secondary nucleation and Ostwald ripening. Both of these processes are schematically illustrated in *Figure 30*.
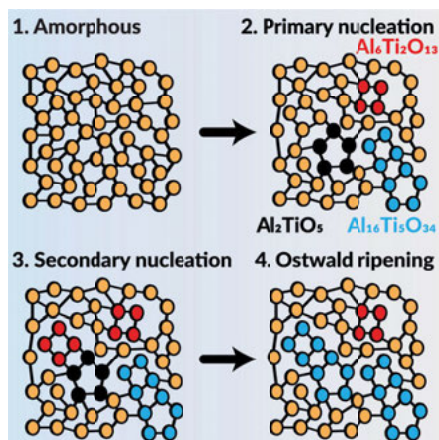
Figure 30. Schematic description of the multiple nucleation pathways deemed involved in the formation of Al_2TiO_5 (black), $Al_6Ti_2O_{13}$ (red) and $Al_{16}Ti_5O_{34}$ (blue) during crystallisation.

In hindsight, it is interesting to note that the combination of secondary nucleation and Ostwald ripening marks a possible non-classical crystallisation pathway for the $Al_{16}Ti_5O_{34}$ phase. Moreover, the findings made in the subsequent **Paper III** can also be invoked to explain this process in more detail.

Essentially, the studies in this paper indicate that the crystallisation process for ~ideal stoichiometric samples is driven by the short-range migration of oxygen and its related vacancies. It is likely, though only surmised, that the same goes when the sample composition is Al-enriched. The theoretical calculations in **Paper III** show that vacancies seem to conglomerate around aluminium, rather than titanium, due to these migrations. It is possible that this process could lead to a cation ordering where aluminium ions solely occupy the formed lower coordinating sites. It is recalled that this would comply with the structural description of the $Al_{16}Ti_5O_{34}$ phase, as given initially by Hoffmann *et al.*[50] Thus, this suggests that the interaction of vacancies could be responsible for the peculiar growth behaviour of the $Al_{16}Ti_5O_{34}$ phase in the Al-enriched domain, although this remains to be verified. In either case, it should be noted that recent findings in the literature have demonstrated that Ostwald ripening can be mediated by the presence and interactions of defects,[163,164] like vacancies.

7.3 The Role of Vacancies in Phase Formation and Crystallisation of $Al_6Ti_2O_{13}$ and $Al_{16}Ti_5O_{34}$

Defects on the local short-range can have a tremendous impact on materials' macroscopic properties, especially for many oxide-based materials by the presence and interaction of vacancies. These vacancies may influence not only the electronic properties of oxide materials but also their crystal structures, surface chemistries and overall microstructures.[165,166] They can induce significant structural distortions and novel oxygen-deficient metastable phases,[167] which are typically challenging to synthesise by conventional synthesis routes relying on thermodynamic control.[141] Intriguingly, the development of more capable *in situ* analytical techniques has also revealed the influence of defects in many chemical processes.[168,169]

When examining oxygen's influence during the crystallisation and co-formation of $Al_6Ti_2O_{13}$ and $Al_{16}Ti_5O_{34}$, an influence from vacancies was also discovered. The combined results of **Paper III** suggest that vacancies are involved in the co-formation of $Al_6Ti_2O_{13}$ and $Al_{16}Ti_5O_{34}$ within the ~ideal stoichiometric domain. Moreover, the results indicate that a link exists between structural relaxations of oxygen and the migration of its vacancies. These mechanisms are deemed responsible for the crystallisation of the $Al_xTi_yO_z$ coatings on an atomistic, fundamental level, and also imply that the amorphous-to-crystalline transition is essentially diffusionless. This claim is supported in **Paper III** by combining theoretical calculations with spectroscopic evaluations.

7.3.1 *What Causes the Formation of $Al_6Ti_2O_{13}$ and $Al_{16}Ti_5O_{34}$?*

Previous examinations led by Hoffmann *et al.* have demonstrated that the formation of $Al_{16}Ti_5O_{34}$, in particular, occurs more preferably in Al-enriched environments.[50] In addition, non-equilibrium conditions such as rapid heating and quenching were required to synthesise this phase from the solid-state route. This indicates that nucleation – rather than diffusion – should be the predominant mechanism responsible for forming these phases, in agreement with the results of **Paper II**. Also, in a broader context, it implies that kinetic effects – rather than thermodynamic ones – play a more significant role in synthesising these phases. Coupled with the results from **Paper I**, one can thus deduce that nucleation and short-range deviations are crucial parameters responsible for giving rise to the $Al_6Ti_2O_{13}$ and $Al_{16}Ti_5O_{34}$ phases. However, besides structural differences due to any changes in coordination polyhedra, neither **Paper I** nor **Paper II** can explicate the origin of these short-range deviations. This marks the central scientific question explored in **Paper III**. Besides coordination changes, structural differences in the local short-range can also be induced by compositional differences, mixed valence states, or the presence of a

homogeneity region. These effects can be elucidated by employing various *in situ* spectroscopic techniques, and the results are summarised in the following paragraphs.

To explore compositional differences during the amorphous-to-crystalline transition, *in situ* RBS/EBS (see *Section 6.6.2* and *6.8* for details) were used with different incident He$^+$ energies before and after crystallisation. A typical energy spectrum is presented in *Figure 31*, demonstrating no detectable spectrum alteration because of the transition. This means that no compositional fluctuation, such as long-range diffusion, elemental segregations or loss or gain of oxygen, occurs as part of the crystallisation. In other words, it implies that the transformation is polymorphic, *i.e.* without compositional changes,[170] and that such effects cannot be ascribed to the co-formation of $Al_6Ti_2O_{13}$ and $Al_{16}Ti_5O_{34}$ on the long-range ordering. Paper IV shows that this notion is also valid in the short-range order based on *in situ* HAADF imaging. Thus, these results essentially exclude compositional effects as the reason for the co-formation of $Al_6Ti_2O_{13}$ and $Al_{16}Ti_5O_{34}$. Furthermore, they experimentally illustrate that features on the local short-range are determinants to the formation of $Al_6Ti_2O_{13}$ and $Al_{16}Ti_5O_{34}$, as initially surmised in **Papers I** and **II**.
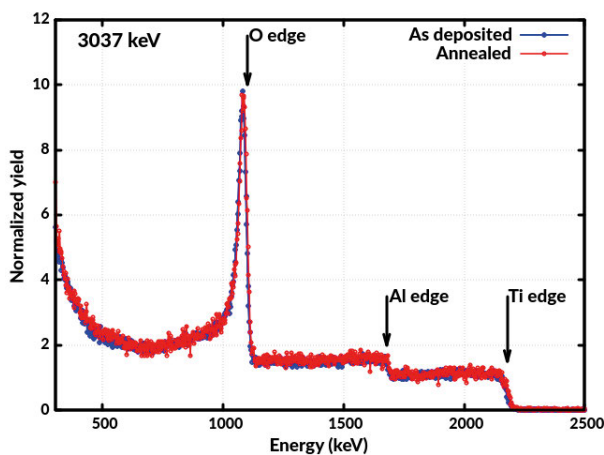
Figure 31. EBS spectra acquired using an incident beam of 3037 keV He$^+$ for as-deposited (blue) and annealed (red) samples with close-to-ideal stoichiometry for the Al_2TiO_5 phase.

Besides composition, another possible reason for these phases' formation is the presence of mixed valence states, especially concerning titanium. Hoffmann *et al.* did not exclude this possibility,[49] although no experimental efforts were made to explore this in their studies. By using XPS, Innocenzi *et al.* showed before Hoffmann *et al.* that Al^{3+} and Ti^{4+} were the only oxidation states found in Al_2TiO_5 after

annealing and crystallisation.[171,172] However, except for anatase co-formation, no additional phase formations (*e.g.* $Al_6Ti_2O_{13}$ or $Al_{16}Ti_5O_{34}$) were mentioned in these works. It should be noted that XPS is a highly surface-sensitive technique, and that these previous examinations do not rule out the possibility of mixed valence states deeper into the bulk of the examined material. In that regard, HAXPES can probe deeper into the material, typically in a couple of nanometres, rather than Ångströms.

Therefore, HAXPES measurements were carried out in **Paper III**, whose main examined core levels (O 1s, Al 2s, Ti 2p) and valence band features (VB) are compiled in *Figure 32*. Additional core levels (Al 1s and Ti 1s), along with a survey scan, can be found in the supplementary material of **Paper III**.
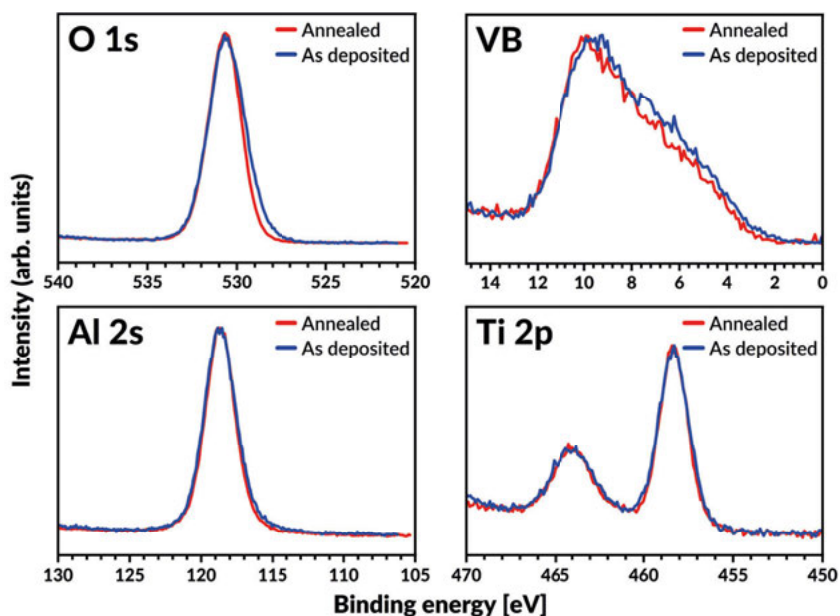
Figure 32. O 1s, Al 2s, Ti 2p core-levels along with valence-band (VB) measurements before and after annealing at 800 °C, using 8000 eV photon energy.

Except for oxygen and the valence band, whose features will be explained later (*Section 7.3.4*), the HAXPES results show no indications of any spectral change in the chemical environments for the cations due to annealing and crystallisation *in vacuo*. The binding energies of the observed peaks agree with those typically found in the literature, corresponding to the presence of Al–Ti–O-containing oxides.[117,172] However, it is important to notice that no straightforward method exists allowing the separation of chemical environments belonging to Al_2TiO_5, $Al_6Ti_2O_{13}$ and

$Al_{16}Ti_5O_{34}$ by merely considering the binding energies and peak shapes of these core levels.

The peak position and shape of the rightmost Ti $2p_{3/2}$ level unambiguously corroborate the sole presence of Ti^{4+} in the coating before and after annealing and crystallisation.[173,174] Since XRD demonstrate the co-formation of $Al_6Ti_2O_{13}$ and $Al_{16}Ti_5O_{34}$, and that no alternate oxidation state is expected for Al^{3+}, these measurements conclude that Ti^{3+} is not a structural entity belonging to either $Al_6Ti_2O_{13}$ or $Al_{16}Ti_5O_{34}$.

By ruling out the possibility of compositional fluctuations and mixed valence states during crystallisation, a final cause essentially remains that could explain the co-formation of $Al_6Ti_2O_{13}$ and $Al_{16}Ti_5O_{34}$ in the ~ideal stoichiometric domain; namely, if the formation of these phases is allowed due to the presence of a homogeneity region. Interestingly, such homogeneity region is not displayed in conventionally available thermodynamic Al–Ti–O phase diagrams, where Al_2TiO_5 is solely represented as a single line phase.[10] Regardless, as mentioned in *Section 7.1.6* on page 67, a homogeneity region can also be induced through structural defects,[136–139] like Schottky-, Frenkel-, and antisite exchange defects. Especially for oxides, a strong relationship may exist between the vacancy concentration and the molar volume of a given compound, resulting in increased chemical expansivities and local lattice variations.[139] This implies that defects, particularly in the form of oxygen vacancies, are involved in the formation of $Al_6Ti_2O_{13}$ and $Al_{16}Ti_5O_{34}$. As explained in *Section 7.3.3*, this notion may also apply to the crystallisation of these phases.

7.3.2   *Antisite Defects Formations*

Based on the HAXPES results in the previous section, the chemical environment for the cations is not altered due to the annealing and crystallisation. To further explore the behaviour, and also examine the potential influence from any defects, first-principle *ab-initio* calculations were carried out by DFT to extract antisite defect exchange energies ($\Delta E_{antisite}$). An antisite defect is a crystallographic defect wherein two or more atoms exchange their mutual positions. Per definition, $\Delta E_{antisite}$ denotes the energy difference between the lowest energetic configuration where an antisite exchange defect exists compared to an ordered (ground state) configuration. This can be expressed as:[175]

$$\Delta E_{antisite} = E_{antisite} - E_{ordered} \qquad \textbf{(Eq. 23.)}$$

Where $E_{antisite}$ and $E_{ordered}$ represent the formation energy of a single-disordered and ordered configuration, respectively. Due to the large unit cell of the $Al_{16}Ti_5O_{34}$ and

the number of atoms it contains, it is difficult to determine this phase's most ordered (ground-state) configuration. Notwithstanding this limitation, $Al_{16}Ti_5O_{34}$ is structurally similar to Al_2TiO_5 and $Al_6Ti_2O_{13}$ on the short-range and long-range orders.[50] Therefore, it is reasonable to assume that the calculated values scale towards $Al_{16}Ti_5O_{34}$ in a similar – albeit not necessarily equal – manner.

Table 4. Calculated antisite exchange defect energies for the Al_2TiO_5 and $Al_6Ti_2O_{13}$ phases.

Antisite exchange defect energies

Phase	Al_2TiO_5 (128 atoms)	$Al_6Ti_2O_{13}$ (168 atoms)
Al1 (eV)	0.29	0.09
Al2 (eV)	0.43	0.16
Al3 (eV)	0.47	0.45

Table 4 summaries the calculated values for Al_2TiO_5 and $Al_6Ti_2O_{13}$ by considering three arbitrary Al site positions within these phases, as noted in *Figure 33*. The calculated values are all positive, indicating that the ordered structure is energetically more stable than the disordered ones. In terms of Al_2TiO_5, this observation agrees with Hoffmann *et al.'s* revised structure model, where a slight site preference was found for titanium in the *4c* (M1) and aluminium in the *8f* (M2) octahedral sites, respectively.[140] That said, the calculated values are all small, suggesting that they can easily be overcome in a Gibbs-free energy model where entropic contributions are included.

Two implications can be drawn based on these results. First, because the calculated antisite energies are similar to those displayed from Al_2TiO_5, a significant cationic disorder can be expected in $Al_6Ti_2O_{13}$, and likely $Al_{16}Ti_5O_{34}$ as well. This agrees with the structural models given for these phases.[19,49,50] Second, the low and similar values found for these phases, and their structural resemblances, infer that minimal diffusion should be required to form any of them. This notion agrees with the HAXPES
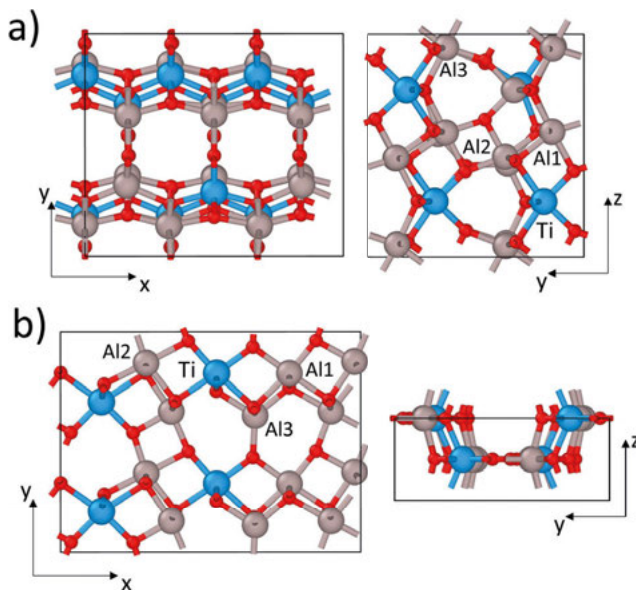
Figure 33. Illustration of the (a) Al_2TiO_5 and (b) $Al_6Ti_2O_{13}$ unit cells with the different sites marked for the antisite defect exchange energies (*cf. Table 4*).

and RBS results in *Figures 31* and *32*. It also supports that structural relaxations and nucleation are the principal reasons for these phases' formations. Since the Raman results of **Paper I** demonstrate a strong presence of short-range Al–O–Ti bond assemblages, it is reasonable to believe such relaxations should primarily involve short-range oxygen displacements. Interestingly, this is also supported by the HAXPES results and further theoretical calculations, as explained in *Section 7.3.4* regarding a diffusionless transformation.

7.3.3 Migration Pathways of Oxygen and its Vacancies During Crystallisation

In addition to the antisite calculations, DFT was also used in **Paper III** to explore the possible short-range migration pathways of oxygen in Al_2TiO_5. Because oxygen displacement is associated with a corresponding formation of an oxygen vacancy, these calculations consider the migration of both entities. Several different possible Al_2TiO_5 configurations were evaluated by DFT, which followed the constraints from the HAXPES results regarding the cations' respective oxidation states. Among the examined configurations, one low-energy configuration was selected, which is presented in *Figure 34*, where the oxygen vacancy is located in a three-coordinated site with only Al^{3+} ions as the nearest neighbours. From this configuration, there are three possible oxygen ion migration pathways to fill the vacancy, namely:

(1) Oxygen moves from a nearby aluminium-bonded (geometry equivalent) position *in the same row* with no change in coordination number. This corresponds to migration pathway 1–0 of *Figure 34*.

(2) Oxygen moves from a nearby position bonded to two aluminium and one titanium ion to only an aluminium-bonded position *in the same row* (pathway 2–0). Again, no change in coordination number occurs.

(3) Oxygen moves from an enclosed position bonded to two aluminium and two titanium ions *between rows* (pathway 3–0). This displacement implies that the oxygen ion reduces its coordination number from 4 to 3.

All migration pathways can be visualised in *Figure 34 (a)-(c)*, with final energy barriers and energies for the forward (E_f) and backward (E_b) pathways stated. The calculated values are also listed in *Table 5* for easier comparison.
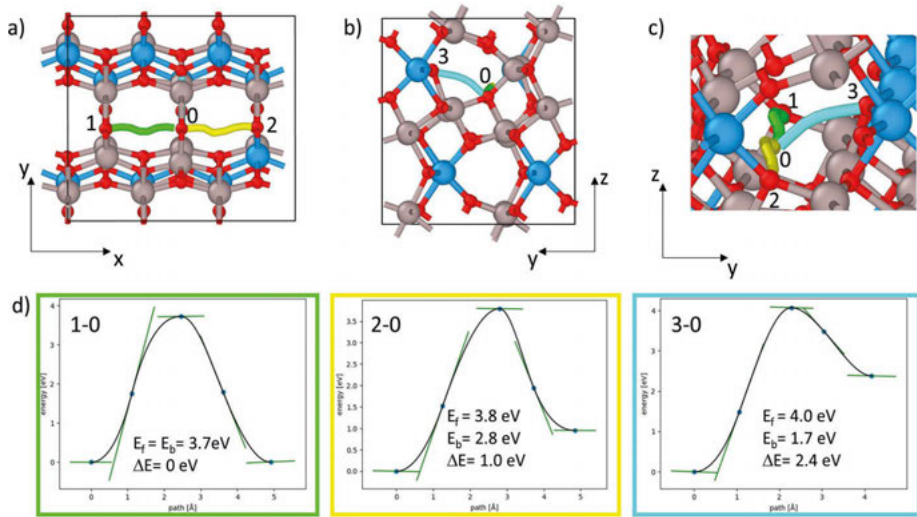
Figure 34. Visualisation of migration pathways for oxygen in Al_2TiO_5, shown by different cell projections in a–c. (d) denotes different forward (E_f) and backward (E_b) barrier energies corresponding to oxygen's movement from positions 1, 2, and 3 to position 0, respectively. Each migration pathway is also listed and described in the text. ΔE denotes the difference in vacancy formation energy between two designated positions.

Table 5. Calculated minimum energy barriers corresponding to the migration of oxygen ions (and its coupled vacancy formation) in Al_2TiO_5. The diffusion paths are shown in *Figure 34*.

Migration Path (*cf. Figure 34*)	E_b (eV)	E_f (eV)	ΔE (eV)
0–1/1–0	3.7	3.7	0
0–2/2–0	2.8	3.8	1.0
0–3/3–0	1.7	4.0	2.4

As emphasised in *Figure 34* and *Table 5*, there are considerable energy penalties for having oxygen vacancies in the vicinity of Ti^{4+}. Similarly, the oxygen ion is most stable in position 3, where it is noted that this position is a four-coordinated site with two Al^{3+} and two Ti^{4+} as nearest neighbours. The energy barriers affect the migration of oxygen, making the calculated values heavily dependent on its possible migration pathways. While the migration of vacancies into the vicinity of Ti^{4+} ions yields steep energy barriers around 4 eV (case 1–0, 2–0, and 3–0 in *Figure 34*), the calculated values for moving oxygen in the opposite direction are significantly smaller. Specifically, moving the vacancy away from the Ti^{4+} ion, expressed by the migration pathways 0–2 and 0–3, gives energy values around 2.8 eV and 1.7 eV, respectively. Interestingly, these latter values are within reach for the typical annealing temperatures where Al_2TiO_5 has been found to crystallise, *i.e.* 1073 Kelvin. For comparison, previous calculations by Grimes and Pilling have shown comparable large values for the cations, 6.10–11.30 eV.[176] Consequently, combined with the previous results in **Paper III**, this indicates that the migration of oxygen and its vacancies are predominantly involved in the crystallisation process.

The computed values for the migration pathways presented herein can be viewed to represent upper energy values. That is because they have been calculated for the crystalline state of Al_2TiO_5, and not any of its possible amorphous configurations. Therefore, the migration barriers of oxygen can be expected to be significantly lower in the amorphous (disordered) state, which favours the perception that short-range displacements of oxygen are involved in the amorphous-to-crystalline transition.

7.3.4   Structural Relaxations and Diffusionless Transformation

Initially deduced in **Paper I**, strengthened by **Paper II**, and experimentally examined in **Paper III** and **IV**, the results of this thesis coherently indicate that the crystallisation process proceeds through a diffusionless (displacive) transformation. In particular, the results of **Paper III** indicate that short-range displacements of oxygen and vacancies are responsible for the transition. Before further expositions are made

on this topic, it is necessary first to clarify the meaning of "diffusionless" on a fundamental level.

With few exceptions, phase transformations may proceed through two different main pathways: (1) reconstructive and (2) displacive (diffusionless) transformations.[177] The first one may involve the breaking and reconstruction of bonds as well as the long-range diffusion of atoms.[177,178] The second one, however, requires only cooperative short-range structural displacements to occur, like coordination changes or altering of bond distances and angles.[177,179] It does not necessitate any random movement of the atoms which,[177] per definition, marks a diffusional process.[180] A classic example of a displacive transformation is the formation of martensite in steel, even though diffusion-less transformations may also occur among other material systems,[179] such as oxides.[181] In addition, as noted by Brent Fultz, because the ions do not move with individual independence, the change in configurational entropy is typically small for a displacive (diffusionless) transformation.[182] Noteworthy, this notion cohere with the inference of a possible diffusionless transformation in cases of nucleation-controlled crystallisation, as explained in *Section 7.2.6*.

Beyond (1) the Raman results, (2) the nucleation-controlled crystallisation pathway, (3) the insignificant compositional fluctuation, (4) the calculated antisite and migration barriers, and (5) the high barriers for migration of the cations, a diffusionless transition can also be inferred based on (6) the HAXPES results in *Figure 32* on page 88. The sharpening of the O 1s level, coupled with corresponding changes in the valence band, indicates structural rearrangements of the oxygen polyhedral surrounding the cations due to annealing and crystallisation. Moreover, the sharpening of the O 1s level indicates more ordered bond configurations after crystallisation, which indicates a diffusionless transition wherein only bond distances and angles are being altered. In hindsight, analogous structural changes can also be inferred from the Raman results in **Paper I**.

The previous notions about a diffusionless transition require that a limited movement of the cations occurs. In other words, oxygen should essentially "adapt" to the cations, and not the other way around. So far, this notion has been deduced in **Papers I** and **II**, and experimentally supported by DFT calculations and HAXPES in **Paper III**. To further corroborate this notion, molecular dynamic simulations (MD) have also been made, whose preliminary results are displayed in *Figure 35*. The figure compiles the results from these simulations, which consider a large supercell of $Al_xTi_yO_z$ and three different simulation cases (1–3), corresponding to successively increasing temperature.
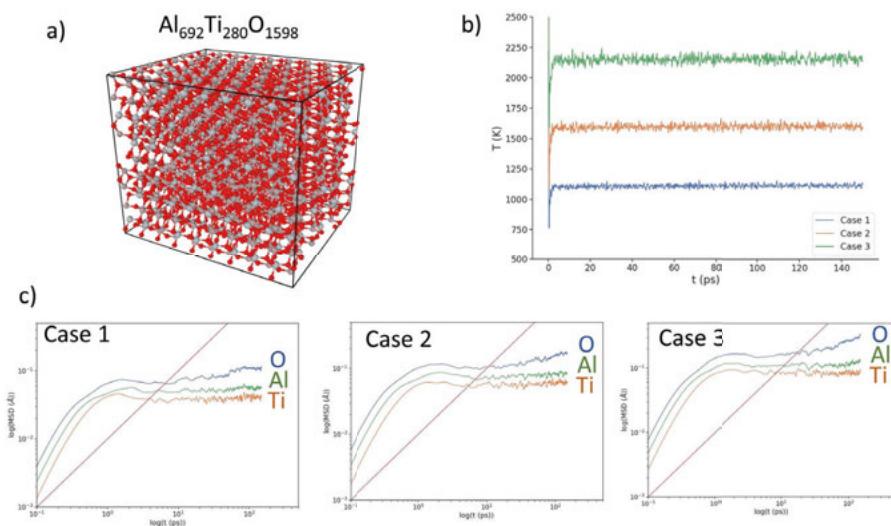
Figure 35. (a) Structural model used in the molecular dynamics simulations, b) T vs t for the three cases (c) log(MSD*) *vs* log(t) for each case in (b). With increasing temperature, the cations do not move while the oxygen is seen to approach a diffusive state (slope=1). *MSD = Mean Squared Displacement. *Note: Unpublished work at the time of publishing the thesis.*

The results show that the cations remain practically stationary for all examined cases. In contrast, the movement of oxygen increases steadily as the temperature increases until the element finally reaches a diffusive state at the highest one. Notably, crystallisation of Al_2TiO_5, $Al_6Ti_2O_{13}$ and $Al_{16}Ti_5O_{34}$ readily occurs at temperatures lower than the three examined cases. Structural relaxation is also a much faster process than diffusion.[71] Consequently, along with the previous results mentioned in this section, this implies that structural relaxations of oxygen are predominantly required to induce the crystallisation of these phases, thereby corresponding to a diffusionless phase transformation.

7.4 Examining the Crystallisation Process by *In Situ* TEM

7.4.1 *General Aspects and Experimental Set-Up.*

The ability to perform analytical examinations *in situ* allows for enhanced information to be gathered about many dynamic processes, including phase transitions and crystallisation. *In situ* approaches provide a leverage in understanding how materials evolve with time and under the influence of different physicochemical environments. It may also provide new information regarding the interplay between thermodynamics and kinetically driven pathways, reveal transitional metastable phase formations, and optimise annealing conditions for crystallisation, phase- and microstructural developments.[183]

Among the various *in situ* techniques available, the ability to "see" chemical processes as they happen has allowed vastly improved mechanistic insights to be obtained. *In situ* TEM is one such modern technique that has, among many other things, contributed to a deepened fundamental understanding of crystallisation phenomena.[184]

In light of these advantages, **Paper IV** explores the crystallisation behaviour of as-deposited $Al_xTi_yO_z$ coatings with a close-to-ideal 2 : 1 Al/Ti ratio when annealed *in situ* in a TEM instrument. The findings of this study corroborate several previous notions about the crystallisation process, especially by showing a diffusionless (displacive) amorphous-to-crystalline transformation and the role of nucleation.

When using *in situ* heating in a TEM, an essential aspect of the experimental set-up is the low thermal inertia of the lamella due to its small thickness and size. This means that very fast heating and cooling rates can be achieved, as exemplified in *Figure 36*. Essentially, this allows one to seamlessly freeze and resume any stages of the crystallisation process by simply switching the heating stage off and on.

In **Paper IV**, five different lamellas were prepared and analysed in the temperature interval 750–900 °C, and their main displayed crystallisation features are listed in *Table 6* as an overview.
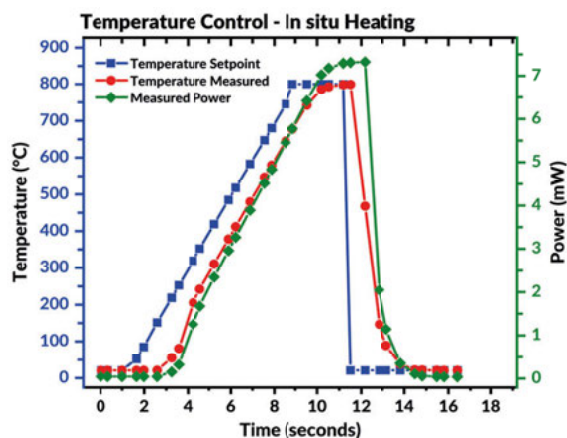
Figure 36. Temperature control for the used *in situ* heating equipment in the TEM. The heating and cooling rate is approximately 100 °C/s and -500 °C/s, respectively.

Table 6. Summary of performed analyses and the main crystallisation features observed.

Chip de-signation	Preparat-ion	Examined T range (° C)	Heating times	Main crystallisation features
1.	Ok	700-800	108 min	30 nm top phase, rest is amor-phous.
2.	Surface Precipita-tes	750-800 800-900	31 min 14 min	Large crystal propagation.
3.	Good	750 900	60 min < 300 ms	Small crystal formation (<10 nm), followed by rapid crystallisation.
4.	Good	800 800	6.5 min 4 min	Multiple crystal formations, fol-lowed by large crystal propaga-tion.
5.	Good	800 780-900	5 min 9 min	Multiple crystal formations, fol-lowed by large crystal propaga-tion.

7.4.2 Initial Crystal Formations

The combined investigations in **Paper IV** show that all lamellas readily crystallise in the temperature regime of 800–900 °C. At 800 °C, numerous smaller crystals with a radius below 10 nm started appearing all over the amorphous matrix, as demonstrated in *Figure 37 (a)*. Their crystallinity was also confirmed using selected area electron diffraction (SAED) in the TEM, seen in *Figure 37 (b)*.
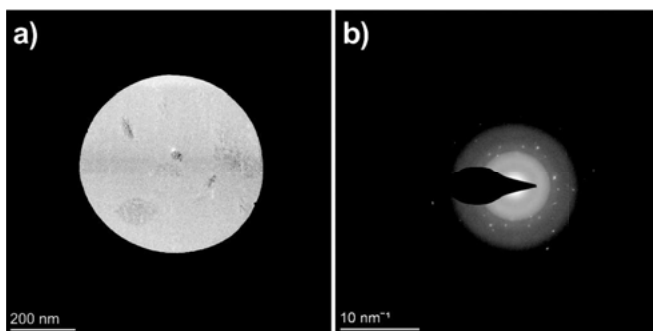
Figure 37. (a) TEM selective aperture image, showing numerous smaller crystals formed at the initial stages of crystallisation and (b) the corresponding electron diffraction pattern. Image was taken at room temperature from Chip 5.

Further analyses were carried out on some larger crystals, as demonstrated in *Figure 38*. The SAED yielded two distinct diffraction patterns, suggesting that the probed crystals either correspond to different (crystalline) phases, or a single phase with different lattice orientations. In order to evaluate this further, indexing of the emerged patterns was made, whose results are given in the supplementary material of **Paper IV**. The goodness of the fit shows that the observed diffraction patterns can be fitted to the phases Al_2TiO_5, $Al_6Ti_2O_{13}$ and $Al_{16}Ti_5O_{34}$. This implies that more than one phase may nucleate simultaneously as part of the crystallisation event, which agrees with previous findings from **Paper II**. However, it is possible to index all three of these phases interchangeably to the emerged diffraction patterns, which is likely because Al_2TiO_5, $Al_6Ti_2O_{13}$ and $Al_{16}Ti_5O_{34}$ are structurally very similar.[19,49,50] Therefore, separating these phases from each other by merely considering the emerged electron diffraction patterns remains challenging, and likely depends on the imaged zone axis.

The fact that the crystals emanate within the amorphous matrix indicates a homogenous nucleation mechanism, which agrees with the kinetic results of **Paper II**. However, it is important to notice that one cannot exclude the possibility that the crystals in the TEM arise at the surface of the lamella.
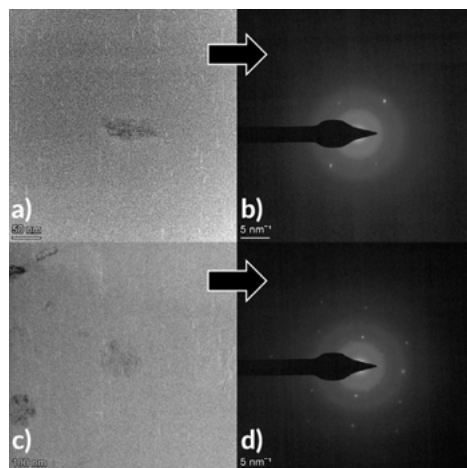
Figure 38. Evaluation of two initially emerged crystals from Chip 4, shown in (a) and (c). Their corresponding SAED patterns are given in (b) and (d). The white stripes seen in the image are present before heating. Images were taken at room temperature after annealing at 800 °C.

The *in situ* RBS results of **Paper III** indicate that no substantial compositional fluctuation occurs as part of the crystallisation event, particularly in terms of the long-range ordering. **Paper IV** shows that similar notions can be made regarding the short-range (nanoscale) ordering. These results are compiled in *Figure 39*, which examines an emerged crystal in the amorphous matrix using dark field imaging in a scanning mode of the TEM (STEM HAADF) and EDS.

While clear diffraction contrast of the crystal can be distinguished from the provided bright-field (BF) and dark-field (DF) images, The STEM HAADF image shows no substantial contrast between the crystalline and amorphous regions. This observation indicates that they comprise the same average atomic weight and that no phase separation occurs during crystallisation. Similarly, the EDS results confirm that no compositional variation exists between the crystalline and amorphous regions. Accordingly, following the RBS results in **Paper III** (*Section 7.3.1*, page 86), these investigations show that the amorphous-to-crystalline phase transformation is predominantly polymorphic, *i.e.* occurs without compositional changes.
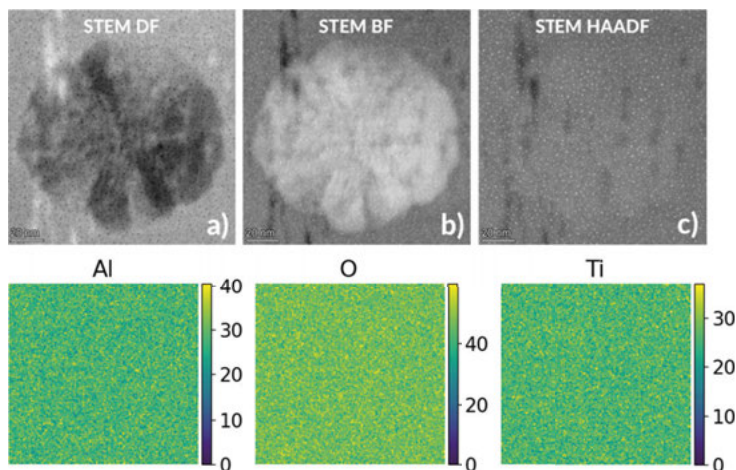
Figure 39. (Top) STEM dark-field image and bright-field images (shown in a and b) coupled with STEM HAADF. Images were taken at room temperature after anneaing at 800 °C for 7 min and originate from Chip 4 (*cf. Table 6*). The white "dots" that are seen in the images are tiny precipitates at the surface of the lamella, which appear in the first minutes of heating in the TEM. Scalebar is 20 nm. **(Bottom)** EDS chemical composition (at%. relative) of the crystal. No compositional difference or gradient between the amorphous and crystalline regions can be detected.

7.4.3   Nucleation Rate and Transient Nucleation Behavior

Continued isothermal annealing at 800 °C yields slow growth of the initially emerged crystals. After an initial annealing period, where numerous smaller crystals form, a rapidly progressing crystalline phase wave suddenly emerges from the side of the lamella. This phase wave progresses with various velocities in different directions, seemingly enveloping any pre-formed crystals without altering their general shape or appearance. This can be seen in the image series in *Figure 40*.

Based on the image series and the emergence of the crystal population, it is possible to estimate an upper nucleation rate (I_t) from manual counting of the crystal population N as a function of time, *i.e.* $I_t = \frac{dN}{dt}$. This is compiled in *Figure 41*, demonstrating an exponentially increasing crystal population characteristic of a time-dependent (transient) nucleation behaviour. Interestingly, a transient nucleation behaviour can also be inferred from the Avrami results in **Paper II** when the coating stoichiometry is close-to-ideal (see *Section 7.2.3* on page 74).
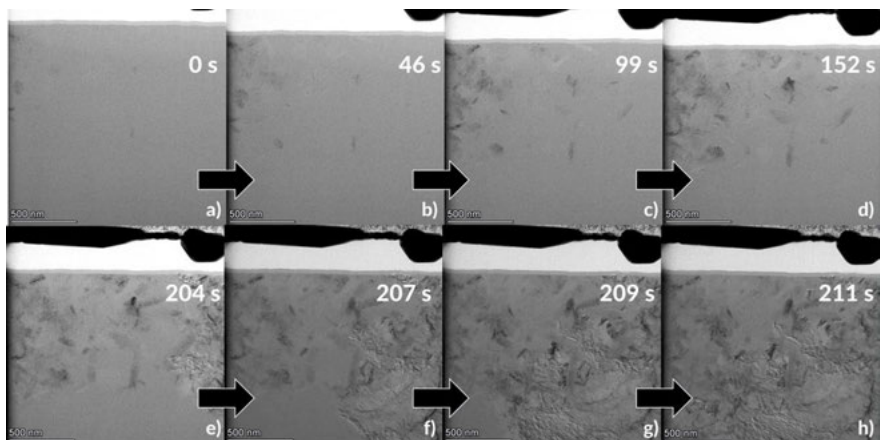
Figure 40. *In situ* image series from Chip 4, showing the nucleation and propagation of the crystal front wave during continuous annealing at 800 °C. Scalebar is 500 nm.
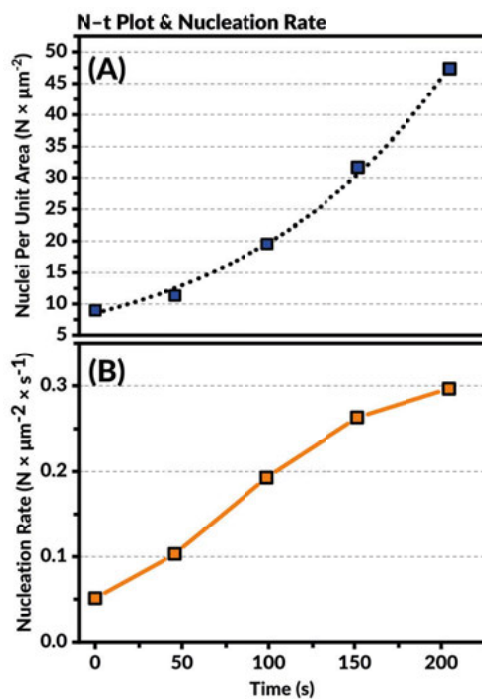
Figure 41. (A) N–t plot demonstrating the evolution of the nucleation population with time. A transient (time-dependent) nucleation behaviour is observed. Exponential trend is emphasised by the black dotted line. (B) Progression of the nucleation rate with time.

The transient nucleation behaviour is interesting from a couple of aspects. Because of the fast nucleation process displayed among most amorphous materials, a time-independent (steady-state) nucleation rate is typically only considered,[150] where the crystallisation process is deemed limited due to the growth by diffusion.[96,105] However, analogous to what is noted in *Section 7.2.3*, a transient nucleation behaviour highlights a process where the nucleation process becomes even more prominent. Specifically, it indicates that no discontinuity exists in cluster formation around the critical radius, meaning nuclei emanate from very small sizes.[82,103,151] In the framework comprising CNT, this also implies that the driving force of nucleation should be high (*i.e.* low barrier of nucleation),[90] resulting in rapid nucleation rates. Despite this, the estimated nucleation rate from *Figure 41* is 0.3 N × μm^{-2} × s^{-1}, which should be regarded as low.

The fact that the nucleation rate is low, even though the thermodynamic driving force of nucleation can be expected to be high, implies that the nucleation process is kinetically impeded. By recalling that an expression of the steady-state homogenous nucleation rate can be given as (*Equation 6*),

$$I_{st} = I_0 \cdot \exp\left(-\frac{W^* + \Delta G_D}{K_B T}\right) \qquad \textbf{(Eq. 6.)}$$

this also suggests that the nucleation process is primarily dependent on either the pre-exponential I_0 factor or ΔG_D – the kinetic barrier of nucleation. Notably, ΔG_D is often described as governed by diffusion.[77,79] However, the results from **Paper III** indicate that limited diffusion is involved in the crystallisation process. Furthermore, a strong structural resemblance exists between the amorphous and crystalline states, favouring short diffusion distances. Therefore, ΔG_D can be assumed to be low as well. Essentially, this implies that the pre-exponential factor I_0 should be the leading factor influencing the overall nucleation rate during the crystallisation of the Al$_x$Ti$_y$O$_z$ coatings.

I_0 represents a kinetic ("attempt") frequency factor relating to the number of interactions between reacting specimens.[76,80] Because **Paper III** shows that the migration barrier for oxygen and its vacancies are relatively low, whereas similar barriers for the cations are high,*** it is plausible that these interactions arise from oxygen and

---

*** See also works by Grimes and Pilling.[176]

vacancy migrations. An increased number of such interactions would thus lead to increased attempts to cross the nucleation barrier, resulting in more rapid nucleation rates. In other words, these inferences point to a possible involvement of vacancies and their migrations in the actual nucleation process, although this can only be surmised at this stage and need further experimental evaluations. Irrespectively, the potential involvement of defects in the nucleation process would mark a possible non-classical crystallisation route in the Al–Ti–O system.

7.4.4 Large Crystal Formations

In one of the examined lamellas (Chip 5), the heating was switched off in the middle of the crystal front wave progression, freezing its current state and allowing it to be thoroughly examined at room temperature. *Figure 42* compiles several observed features, showing that the crystal wave propagates as a needle-like extension.
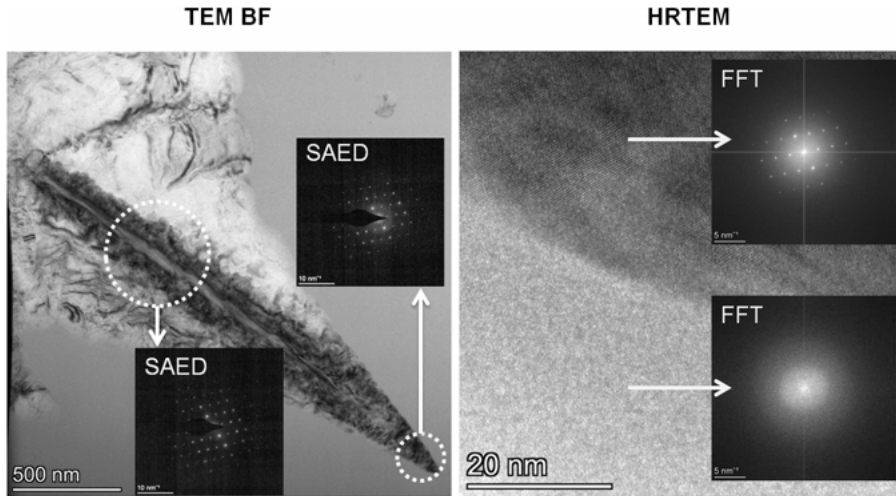
Figure 42. Interrupted crystallisation process showing (A) TEM BF image of the fast-growing needle-like crystal and its associated SAED patterns. The dashed circles indicate the SAED locations. (B) HRTEM image of the tip of the same crystal, with corresponding FFT images from the crystal and the immediate surrounding that is still amorphous and untransformed. FFT calculation regions are shown in the HRTEM image. Images were taken on Chip 5 at room temperature.

Interestingly, when examining the crystal region by SAED, the tip and core of the needle-like domain were found to be the same crystal, as confirmed by the identical electron diffraction patterns. Likewise, a monocrystalline pattern was also detected by using fast-Fourier transform (FFT) calculations, which are seen within the

HRTEM image to the right of *Figure 42.* Indexing of the emerged electron diffraction patterns, given in the supplementary material of **Paper IV**, also demonstrates that the electron diffraction patterns are identical and can be represented from the same zone axis. Thus, these findings support that the crystal front wave mainly grows into one large crystal. In that regard, it is essential to note that no easy separation between the Al_2TiO_5, $Al_6Ti_2O_{13}$ and $Al_{16}Ti_5O_{34}$ phases can be made by the fitting of the diffraction patterns.
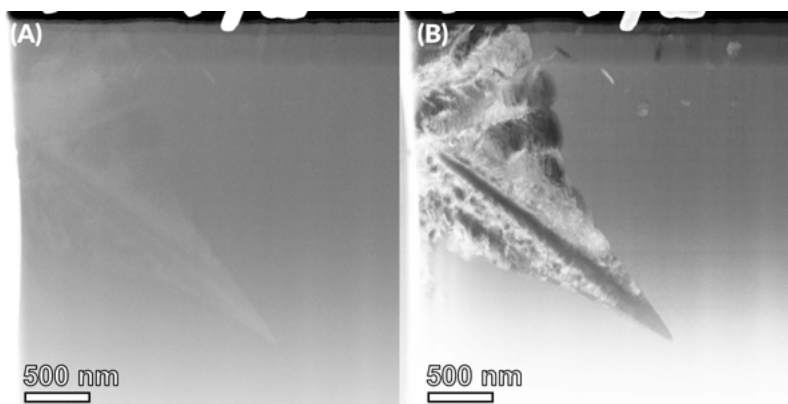
Figure 43. Interrupted crystallisation process, showing (A) a STEM HAADF image with insignificant contrast between the amorphous and crystalline regions and (B) STEM DF image, showing strong diffraction contrast. Images were taken on Chip 5 at room temperature.
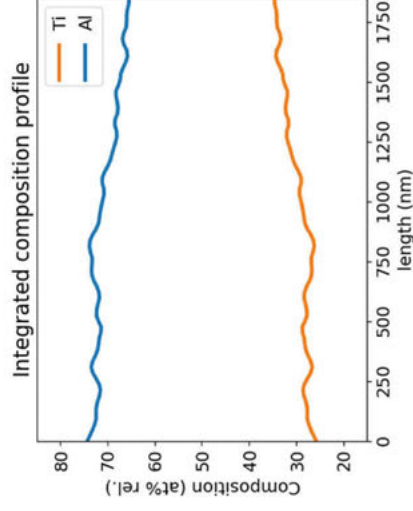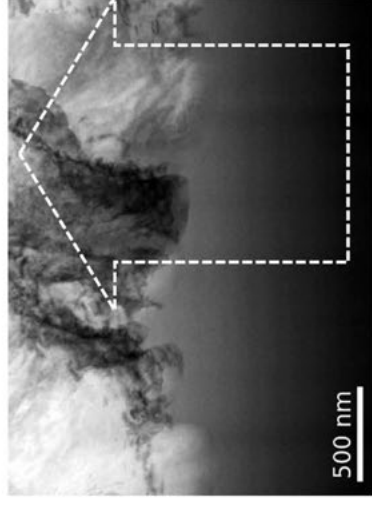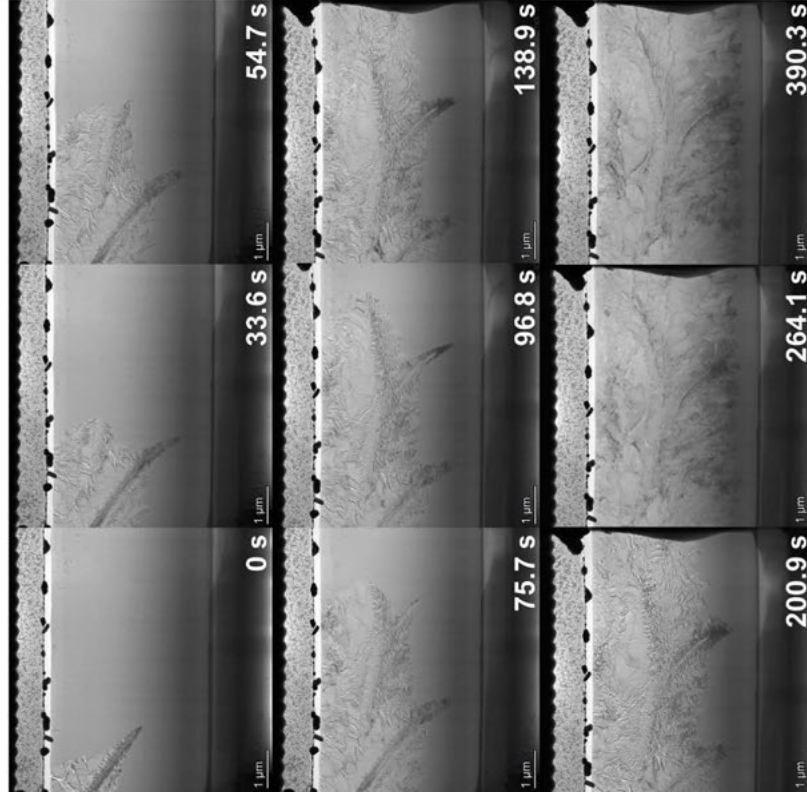
Figure 44. (**Left**) Image series from isothermal annealing of Chip 5 at 800 °C, displaying the progression of the crystal wave with time. Scalebar is 1 µm. (**Right**) Bright-field overview image of the untransformed layer close to the silicon substrate, along with an integrated composition profile starting from the bottom towards the front interface (as marked by the white arrow). Compositional values derived from EDS analysis show the presence of a compositional gradient in the untransformed layer.

7.4.5 Diffusionless Transformation

As seen in the HRTEM image of *Figure 42*, a sharp interface between the amorphous and crystalline regions exists. Coupled with the STEM-HAADF overview image (*Figure 43*), showing insignificant contrast variation, this suggests that only small structural reorganisations are essentially involved in the amorphous-to-crystalline transformation. This is coherent with the results of **Paper III** and acts as a further indication of a diffusionless (displacive) transformation, as explained in *Section 7.3.4* on page *93*.

The rapid progression of the crystallisation front wave, seen from the image series in *Figure 44*, is also indicative of a diffusionless (displacive) transformation. The transformation rate demonstrates a strong temperature dependency and increases significantly when the annealing temperature is raised even further. This is best illustrated by the peculiar transformation behaviour from Chip 3, seen below in *Figure 45*.
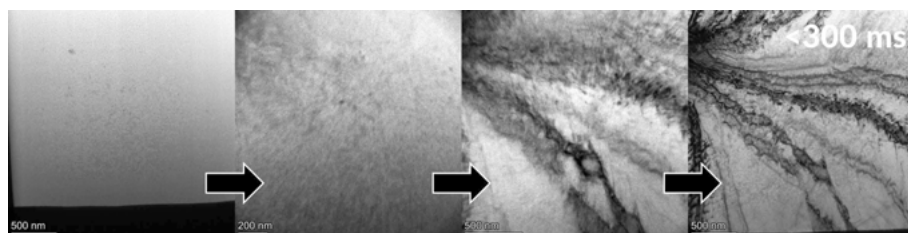
Figure 45 *In situ* image series showing the rapid crystallisation of the amorphous matrix in Chip 3 when the temperature was increased from 750 to 900 °C. The entire lamella crystallises in less than 300 ms.

After an initial annealing period of one hour at 750 °C, the temperature was raised to 900 °C for Chip 3. At this temperature, rapid growth of one crystal occurs until the entire amorphous matrix suddenly collapses and crystallises instantaneously (*i.e.* in less than one image frame, 300 ms). In reality, the duration of the crystallisation process is much shorter since the frame rate was too slow to capture the complete transformation. The reader should also note that a slight radial blur occurs in the image series due to a change in magnification during the rapid transformation.

This particular behaviour does not only point to a nucleation-controlled crystallisation process where the typical slow crystal growth by diffusion is not a rate-limiting step. Because relaxation are a much faster process than any growth by diffusion,[71] it also suggests that the transformation does not require any substantial diffusion to

occur in the first place. Thus, it further demonstrates that the coatings undergo a diffusionless (displacive) amorphous-to-crystalline transformation, in accordance with previous results and inferences from **Papers I**, **II**, and **III**.

7.4.6 *Anisotropic Growth Behaviour and the Influence of Titanium.*

Figure 44 demonstrates that the crystal front wave does not progress similarly in all directions but rather in an anisotropic manner. Specifically, the growth rate diminishes closer to the substrate until the temperature is raised even further. Following the rise in temperature (800 to 900 °C), the growth progresses until it stops again, leaving a bed of untransformed amorphous material close to the silicon substrate.

To better understand this behaviour, the untransformed layer was examined using EDS mapping, whose integrated profile is shown in *Figure 44*. It is shown that a compositional gradient exists in the untransformed layer, which is Al-enriched. The Al-content also decreases in the CVD growth direction. Thus, these results illustrate that crystallisation is impeded in Al-enriched environments and occurs more slowly, which conforms to the results of **Paper II**. Similarly, it also suggests that crystallisation occurs more quickly when the Ti-content increases, which further highlights the elemental influence of titanium in the crystallisation behaviour, as described in *Section 7.2.7* on page 81.

8   Conclusions and Future Outlooks

The coherent results of this thesis emphasise the role of kinetics – rather than thermodynamics – in the synthesis and design of novel ternary oxide coatings by CVD. The simultaneous use of metalorganic precursors, sharing many similarities in terms of their chemical features and reaction routes, enables a selective kinetic targeting of ternary phases that are otherwise difficult to synthesise. Moreover, these precursors' greater flexibility and chemical compatibility allow such phases to be formed at significantly lower processing times and temperatures than comparable techniques. Presumably, these advantages may also scale towards multi-component mixed-metal coatings. It is believed that such coatings can be made in future CVD processing by combining several metalorganic precursors, either simultaneously or sequentially. Therefore, an obvious next step is to attempt to use new precursor combinations and explore different material systems beyond Al–Ti–O.

Metal alkoxides span almost the entire periodic table,[57] and their similar reaction pathways entail, in principle, that various heterometallic bond assemblages can be obtained. Furthermore, the possibilities to adapt and tailor the ligands of these precursors offer an additional dimension to improve their chemical compatibilities during co-depositions. In addition, such approaches can also introduce new functional elements into the coatings. For example, besides alkoxides' ability to readily generate oxides, the introduction of amine-based functional groups into their structures could yield new ways to make oxynitrides. Nevertheless, such routes remain to be explored, and it is unknown from this thesis how the introduction of alternate (heteroleptic) ligands may influence the process control during CVD operations.

Similarly, the propensity of oxygen to act as a bridging ligand between Lewis acids (*e.g.* cations) in alkoxides imply that many so-called heterometallic alkoxides can be synthesised.[51] Compared to their monometallic counterpart, the benefits of these reactants for CVD are not only the fact that they can incorporate a larger amount of metallic elements. In favourable cases, they may even combine these elements in desired ratios, potentially allowing them to be used as efficient single-source

precursors. Such approaches would contribute to streamlining and simplifying the overall MOCVD deposition process.[185]

While the results of this thesis highlight the benefits and future potential of alkoxides, the use of these types of precursors also introduces new kinds of limitations compared to halides. Those limitations must be remedied to allow alkoxides greater usage. Arguably, their cumbersome handling, limited long-term storage capabilities, risk of oligomerisations and (sometimes) time-dependent volatilities, constitute their most limiting factors that must be dealt with in future research. Along with the generally high cost of alkoxides and their limited commercial availabilities, these limiting factors also introduce a "scale-up" problem. Fortunately, it should be possible to overcome many of these factors given that they can provide a more efficient synthesis process; specifically, one that can produce novel material combinations with superior properties.

Such potential material combinations include, for example, high entropy oxides, which incorporate many metal cations in a single-phase crystal structure. These types of oxides have increasingly attracted research interest due to their many favourable properties. In recent years, new classes of perovskites and high entropy pseudobrookite titanate phases have emerged showing, for example, excellent dielectric and solar spectrum absorption properties.[38,186] However, the synthesis of these types of novel phases is challenging. In terms of thin film deposition, they are mostly made with physical vapour deposition (PVD) techniques, and few papers, if any, have so far been published on using CVD to make such phases. Notwithstanding this, as a future prospect, it is suggested that the combined usage of metal alkoxides, particularly heterometallic ones, could potentially allow this.

Based on the findings of this thesis work, many additional interesting research projects can also be done concerning crystallisation and nucleation-control. For example, reducing diffusional constraints may give rise to possible non-classical crystallisation routes, which have attracted significant research interest in recent years. Moreover, such pathways have sometimes been shown to yield intriguing microstructural developments,[187] including large single-crystals and so-called mesocrystal formations.[188–190] The possibilities of such microstructural developments in the Al–Ti–O system, along with a confirmation of non-classical crystallisation routes in the system, remain to be corroborated.

In terms of nucleation-control, an interesting question arises whether this phenomenon is inherent to the phase that is formed or to the CVD technique itself. Indeed, Al_2TiO_5 (and $Al_6Ti_2O_{13}$ and $Al_{16}Ti_5O_{34}$) may display cationic disordering, which is believed to favour a diffusionless crystallisation pathway during their crystallisation. However, nucleation-controlled crystallisation has also been shown to occur within other material systems, and not just oxides.[72,147,148] Therefore, the CVD technique used herein to achieve a nucleation-control crystallisation pathway may also apply to other phases and material systems.

Lastly, this thesis reveals the importance of vacancies and short-range order in forming unconventional phases that are structurally similar to each other. This may have exciting implications for achieving selectivity among polymorphs during the synthesis of oxides, especially if ways to control the vacancy concentration giving rise to such polymorphic structures can be controlled. Knowing that oxygen vacancies are likely responsible for the co-formation of $Al_6Ti_2O_{13}$ and $Al_{16}Ti_5O_{34}$, one can suspect that tailoring the oxygen supply during depositions can be a strategy to either increase or reduce the presence of a particular phase or polymorphic structure. Likewise, the possibilities to design the molecular structure of the metalorganic reactants could also potentially steer the depositions to favour a specific phase or polymorph.[191] These notions are also yet to be explored in the CVD process.

<p style="text-align:center">***</p>

9 Populärvetenskaplig Sammanfattning på Svenska

Upptäckten av nya material har historiskt baserats på experimentella undersökningar och försök där man på förhand inte riktigt vet vad dessa resulterar i. Samtidigt är det svårt att förutbestämma egenskaperna hos nya material baserat på en viss vald syntesväg. Detta gäller inte minst för många oorganiska material som keramer, där det saknas ett unisont syntesramverk som omfattar teoretiska förutsägelser, design och syntes av material med gynnsamma egenskaper. Noterbart är att ett sådant ramverk faktiskt redan finns inom den organiska kemin, vilket möjliggör att nya, komplexa molekyler med önskade egenskaper kan framställas inom exempelvis läkemedelskemin.

Av dessa skäl har det funnits, och fortfarande finns, en stark vetenskaplig drivkraft att utveckla nya syntesvägar som kan möjliggöra bättre kontroll för framställandet av oorganiska material. Samtidigt är det också önskvärt att, som kemist, finna metoder som på ett mer resurseffektivt sätt kan använda de olika slags element som finns i det periodiska systemet, och vars kombinationer utgör möjliga faser med eftertraktade egenskaper. Tunnfilmsteknik, där man på olika sätt deponerar ett mycket tunt ytskikt ovanpå ett annat material, är en sådan syntesväg som har utvecklats. Typiskt är tjockleken av dessa skikt mindre än ett hårstrås tjocklek, varför materialåtgången är mycket låg. Detta är en stor fördel jämfört med många andra tekniker. Till exempel innebär det att man kan utnyttja mer sällsynta element i framställandet av solcellspaneler och liknande.

En annan fördel med tunnfilmsdeponering är att man kan framställa faser som är mycket svåra, eller nära nog omöjliga, att få fram med andra jämförbara tekniker. Detta gäller inte minst syrebaserade (oxid-)föreningar, där små skillnader på atomavstånd kan få avsevärda effekter på materials makroskopiska egenskaper. Kemisk ångdeponering, med dess engelska förkortning CVD ("Chemical Vapour Deposition") är en kapabel tunnfilmsteknik som har många av dessa fördelar. Denna teknik

används inom en rad olika sektorer för att exempelvis framställa halvledare, dioder och hårda, skyddande beläggningar till verktyg.

Ett problem med kemisk ångdeponering är dock att de oftast utnyttjar så kallade halidbaserade reaktanter, som involverar antingen fluor, klor, brom eller jod. Sådana föreningar har ofta relativt begränsade flyktigheter, vilket försvårar möjligheten att kombinera dessa i en process för att få fram önskade faser och föreningar. Som en del av dessa reaktanters reaktioner kan de även generera giftiga och reaktiva biprodukter. Därför finns det ett stort behov av att utveckla nya sorters reaktanter, som både kan reagera renare men som också ger en större valfrihet i framställandet av nya faser och material.

Huvudtemat för denna avhandling är att undersöka användningen av sådana alternativa reaktanter. Specifikt har arbetet fokuserat kring att undersöka fasbildandet mellan aluminium, syre och titan genom att kombinera två sorters molekyler, aluminiumisopropoxid och titanisopropoxid, samtidigt i en CVD-process. För det ändamålet har också en helt ny CVD reaktor byggts upp från grunden.

Sammantaget har de undersökningar som genomförts generat nya, mer effektiva sätt att framställa beläggningar innehållandes aluminiumtitanat (Al_2TiO_5), en fas med värmehållfastbara egenskaper. Detta inkluderar bland annat en mycket hög smälttemperatur (1860 °C), låg termisk ledningsförmåga och bra motståndskraft till snabba temperaturförändringar. Materialet har även en märklig förmåga till att självläkas vid högre temperaturer, och uppvisar en låg-till-negativ termisk utvidningsförmåga. Detta är relativt ovanligt eftersom de allra flesta material expanderar när de uppvärms.

I **Uppsats 1** har experimentella undersökningar genomförts för att bestämma optimala processförhållanden för att framställa aluminiumtitanat via CVD. Genom att öka eller minska halten av titanisopropoxid kan beläggningar med olika aluminiumtill titanförhållanden framställas. Undersökningarna i **Uppsats 1** belyser att de många kemiska likheterna som finns för de använda reaktanterna (aluminium- och titanisopropoxid) är ett skäl till att aluminiumtitanat enklare kan framställas. Dessutom belyser denna uppsats inflytandet av variationer på atomär skala för bildandet av nya, okonventionella faser som benämns $Al_6Ti_2O_{13}$ och $Al_{16}Ti_5O_{34}$.

Alla beläggningar som framställs är helt amorfa, d.v.s. de saknar både en när- och en fjärrordning, och jonerna sitter "huller om buller". När man värmer upp

beläggningar kristalliserar de dock, och jonerna hittar sina "rätta" (ordnade) positioner. Denna process är mycket viktig för många oxider, inte minst bland glas och deras framställningar. **Uppsats 2** undersöker därför denna process genom att värma och mäta samtidigt på beläggningarna med hjälp av s.k. röntgendiffraktion. Detta är en bra teknik för att upptäcka kristallina material med. De sammanlagda resultaten av denna studie visar att kristallisationsprocessen styrs av kärnbildningen, d.v.s. den allra första kemiska processen som sker i övergången mellan det amorfa och kristallina tillståndet. Detta är anmärkningsvärt och relativt ovanligt, då de allra flesta kristallisationsprocesser styrs huvudsakligen av diffusion, d.v.s. den slumpmässiga atomära förflyttningen av element från ett område till ett annat. Resultaten antyder därför att kristallisationsprocessen sker utan diffusion, där endast små omstruktureringar krävs för att få atomerna att hamna "på rätt plats".

För att undersöka detta närmare, och bevisa att det *de facto* är en diffusionsfri kristallisationsprocess, genomfördes ytterligare undersökningar. Dessa utgör resultaten i **Uppsats 3**, där kombinationen av flera avancerade analystekniker användes. Bland annat användes undersökningar med hjälp av synkrotronljus, vilket är en högenergetisk strålning som kan ge information på subatomär nivå. Sådana undersökningar genomfördes utanför Paris på en stor forskningsanläggning vid namn "Soleil". Därutöver användes en tandemaccelerator vid Uppsala universitet, där högenergetiska joner skickas in i provet för att på så vis bestämma deras sammansättningar. Förvånande var att dessa undersökningar inte kunde påvisa några större förändringar mellan det amorfa och kristallina tillståndet. Detta var till en början egendomligt, eftersom resultatet inte kunde ge någon entydig förklaring till det samtidiga bildandet av de okonventionella $Al_6Ti_2O_{13}$ och $Al_{16}Ti_5O_{34}$ faserna som tidigare hade upptäckts.

För att lösa denna gåta söktes extern hjälp där man med hjälp av avancerade teoretiska datorberäkningar och simuleringar kan förstå kemiska processer bättre. Noterbart är att dessa beräkningar utnyttjar nationella datacentrum, bestående av stora datorkluster, där vissa beräkningar kan ta flera veckor att genomföra!

Dessa undersökningar, tillsammans med de tidigare resultaten från **Uppsats 3**, visade på att små förflyttningar av syre troligtvis är ansvariga för kristallisationen. Eftersom syrets förflyttning även är kopplat till bildandet av hålrum (vakanser) i strukturen, illustrerar dessa undersökningar att sådana vakanser också kan förflytta sig i materialet. När en vakans existerar intill en atom så får den en annan kemisk omgivning. Detta fenomen tros vara en förklaring till bildandet av $Al_6Ti_2O_{13}$ och

Al$_{16}$Ti$_5$O$_{34}$. Med andra ord, det är förekomsten av syrevakanser som troligtvis leder till dessa fasers bildande.

Då tidigare undersökningar har visat att kärnbildningen har en central roll i kristallisationsprocessen, undersöktes även denna process med hjälp av ett mycket avancerat mikroskop, kallat för TEM (transmissionselektronmikroskop). Genom att värma provet inuti mikroskopet är det möjligt att visuellt studera kemiska processer ända ner på atomnivå. Detta utgör grunden för **Papper 4**, vars resultat i huvudsak bekräftar tidigare undersökningar, och som visar på att kristallisationen av beläggningarna sker diffusionslöst.

De sammanlagda resultaten av detta doktorsarbete illustrerar hur kinetiken (läran om reaktioners hastigheter) snarare än termodynamiken (läran om energi) styr syntesen av de faser som har framställts. Användningen av nya sorters reaktanter inom CVD tros möjliggöra att fler materialkombinationer och faser kan framställas med denna teknik i framtiden.

Ett kvarstående problem är dock att dessa nya reaktanter fortfarande är dyra, svårtillgängliga och komplicerade att hantera. Detta begränsar för närvarande möjligheterna att skala upp processer där dessa reaktanter används för industriella och kommersiella ändamål. Det är emellertid troligt att många av dessa kan övervinnas om användningen av sådana reaktanter skulle leda till att man uppnår mer effektiva deponeringsprocesser. I synnerhet sådana som kan generera faser samt material med nya, unika och förbättrade egenskaper. Ett exempel på sådana nya faser, som tros kunna genereras i framtiden med hjälp av nya reaktanter, är så kallade högentropioxider. Dessa föreningar innehåller en mix av ett flertal element, vars kombinationer tillsammans ger utökade egenskaper.

De nya vetenskapliga rönen kring kristallisationsförloppet tros också kunna bidra till en ökad förståelse till oxiders kemiska beteenden. Detta kan bidra till att nya oxider och unika strukturer lättare kan framställas. Genom att styra kristallisationsförloppet kan egenskaperna för dessa oxider kontrolleras, beroende på hur dess joner "ordnar sig".

10 Acknowledgements

This work is dedicated to those who have worked patiently,
And persistently,
Not in the background,
But in the foreground,
Who has supported me in my ambitions,
Helped me to succeed,
And reaching my goals,
By putting in a little bit of extra effort,
And thereby yielded an even stronger output.

First, I would like to thank my greatest supporter of all time, my granddad **Kjell Öhman**, for your consistent interest in my school works, constant calls about space and science, and your subscriptions to "Illustrerad Vetenskap". You are missed dearly.

In chronological order. To my elementary school teacher, **Ing-Marie Tirzitis**, for your unlimited support and guidance during my early school years, laying the foundation for my curiosity, eagerness, and willingness to learn.

To **Bo Olsson**, for allowing me access to your library, including *Nationalencyklopedin.*

To my high school teacher and class mentor, **Maria Lindgren**, for your constant questioning, encouragement and teaching me how to analyse.

Likewise, to my second high school teacher and class mentor, **Veronica Jatko Kraft**, for winning the debate and inspiring me to continue within the natural science discipline. Also, for giving an excellent explanation of Bohr's atomic model in the 6th grade, which I still remember to this day.

To my excellent upper-secondary school mentors and teachers in chemistry, **Olof Procopé** and **Peter Möller**, for creating confidence and my interest in chemistry. Your great pedagogics and enthusiasm in the field are why I began to study chemical engineering at Uppsala University.

To **Anders Eriksson**, lecturer in inorganic chemistry at Uppsala University, whose lectures showed me that chemistry involves more than just carbon, oxygen, and hydrogen, and that inorganic chemistry is all (that) matters and rocks.

To **Marianne Collin**, for great collaborations and for showing trust in my work during my master thesis project at Sandvik Coromant.

To **José L. García**, Sandvik Coromant, for encouraging me to pursue a PhD through the most convincing and inspiring talks.

At the department level, I sincerely thank my main supervisors, **Mats Boman** and **Tobias Törndahl**, for all your help, guidance, and support during these years. Also, I would like to thank **Leif Nyholm** and **Erik Lewin**: the two best co-supervisors I never (officially) had.

To **Katalin Böőr**. For not only being the greatest colleague, but also for being a fantastic friend.

To all colleagues, friends, and **Josef Seibt**, whom I met at the coffee table at the Department of Chemistry. You will be missed!

To all my personal friends, including the "cycling gang": **David Berndtsson**, **Olof Ivarsson**, **Patrik Svensson**, **Bella Lagrange**, and **Måns Bergkvist**. For all the laughter and bantering.

To **Hreinn Juliusson**, **Klara Björnander Rahimi**, and their son **Sindri**, for all the support.

Last, but not least.
To my family. Mom and dad, **Yvonne** and **Bengt**, and my sisters, **Fredrika** and **Karolina**. For always believing in my efforts. Even in times, when I did not.

Sebastian, Tuesday, 21 February 2023
Uppsala, Sweden.

11 References

(1)   Gibbs, J. W. On the Equilibrium of Heterogeneous Substances. *Trans. Connect. Acad. Arts Sci.* **1876**, *3*, 108–248; 343–524

(2)   Harada, J. K.; Charles, N.; Poeppelmeier, K. R.; Rondinelli, J. M. Heteroanionic Materials by Design: Progress Toward Targeted Properties. *Adv. Mater.* **2019**, *31* (19), 1805295, DOI: 10.1002/adma.201805295

(3)   Triana, C. A.; Araujo, C. M.; Ahuja, R.; Niklasson, G. A.; Edvinsson, T. Disentangling the Intricate Atomic Short-Range Order and Electronic Properties in Amorphous Transition Metal Oxides. *Sci. Rep.* **2017**, *7* (1), 2044, DOI: 10.1038/s41598-017-01151-2

(4)   Sanchez, C.; Rozes, L.; Ribot, F.; Laberty-Robert, C.; Grosso, D.; Sassoye, C.; Boissiere, C.; Nicole, L. "Chimie Douce": A Land of Opportunities for the Designed Construction of Functional Inorganic and Hybrid Organic-Inorganic Nanomaterials. *Comptes Rendus Chim.* **2010**, *13* (1–2), 3–39, DOI: 10.1016/j.crci.2009.06.001

(5)   Aykol, M.; Montoya, J. H.; Hummelshøj, J. Rational Solid-State Synthesis Routes for Inorganic Materials. *J. Am. Chem. Soc.* **2021**, *143* (24), 9244–9259, DOI: 10.1021/jacs.1c04888

(6)   Jansen, M. A Concept for Synthesis Planning in Solid-State Chemistry. *Angew. Chemie Int. Ed.* **2002**, *41* (20), 3746–3766, DOI: 10.1002/1521-3773(20021018)41:20<3746::AID-ANIE3746>3.0.CO;2-2

(7)   Gopalakrishnan, J.; Bhuvanesh, N. S. P.; Rangan, K. K. Towards Rational Synthesis of Inorganic Solids. *Curr. Opin. Solid State Mater. Sci.* **1996**, *1* (2), 285–294, DOI: 10.1016/S1359-0286(96)80096-9

(8)   Stein, A.; Keller, S. W.; Mallouk, T. E. Turning down the Heat: Design and Mechanism in Solid-State Synthesis. *Science (80-.).* **1993**, *259* (5101), 1558–1564, DOI: 10.1126/science.259.5101.1558

(9)   Panda, S. K.; Jung, I. H. Coupled Experimental Study and Thermodynamic Modeling of the Al2O3–Ti2O3–TiO2 System. *J. Phase Equilibria Diffus.* **2020**, *60*, DOI: 10.1007/s11669-020-00785-6

(10)   Ilatovskaia, M.; Savinykh, G.; Fabrichnaya, O. Thermodynamic Description of the Ti-Al-O System Based on Experimental Data. *J. Phase Equilibria Diffus.* **2017**, *38* (3), 175–184, DOI: 10.1007/s11669-016-0509-4

(11)   Ilatovskaia, M.; Kahrobaee, Z.; Omar, N. A. B.; Palm, M.; Schmitt, L.-Y.; Yang, Y.; Dreval, L. Al-O-Ti Ternary Phase Diagram Evaluation. *MSI Eureka* **2022**, *92*, 10.15250.2.9, DOI: 10.7121/msi-eureka-10.15250.2.9

(12)   Parikh, P. B. Alumina Ceramics: Engineering Applications and Domestic Market Potential. *Trans. Indian Ceram. Soc.* **1995**, *54* (5), 179–184, DOI: 10.1080/0371750X.1995.10804716

(13)   Gyanan; Mondal, S.; Kumar, A. Tunable Dielectric Properties of TiO2 Thin Film Based MOS Systems for Application in Microelectronics. *Superlattices Microstruct.* **2016**, *100*, 876–885, DOI: 10.1016/j.spmi.2016.10.054

(14)   Chugh, B.; Kumar Taraphdar, P.; Biswal, H. J.; Devi, N. R.; Dorothy, R.; Manimaran, N.; Rajendran, S. Corrosion Inhibition by Aluminum Oxide. In *Inorganic Anticorrosive Materials*; Elsevier, 2022; pp 231–249, DOI: 10.1016/B978-0-323-90410-0.00013-1

(15)   Liu, Z.; Welsch, G. Literature Survey on Diffusivities of Oxygen, Aluminum, and Vanadium in Alpha Titanium, Beta Titanium, and in Rutile. *Metall. Trans. A* **1988**, *19* (4), 1121–1125, DOI: 10.1007/BF02628396

(16)   Gunda, N. S. H.; Van der Ven, A. Understanding the Interactions between Interstitial and Substitutional Solutes in Refractory Alloys: The Case of Ti-Al-O. *Acta Mater.* **2020**, *191*, 149–157, DOI: 10.1016/j.actamat.2020.04.017

(17)   Winkler, E. R.; Sarver, J. F.; Cutler, I. B. Solid Solution of Titanium Dioxide in Aluminum Oxide. *J. Am. Ceram. Soc.* **1966**, *49* (12), 634–637, DOI: 10.1111/j.1151-2916.1966.tb13189.x

(18)   Goldberg, D. Contribution to Study of Systems Formed by Alumina and Some Oxides of Trivalent and Tetravalent Metals Especially Titanium Oxide. *Rev. Int. des Hautes Temp. des Refract.* **1968**, *5* (3), 181-., DOI: N/A

(19)   Hoffmann, S.; Norberg, S. T.; Yoshimura, M. Melt Synthesis of Al_2TiO_5 Containing Composites and Reinvestigation of the Phase Diagram Al_2O_3–TiO_2 by Powder X-Ray Diffraction. *J. Electroceramics* **2006**, *16* (4), 327–330, DOI: 10.1007/s10832-006-9873-5

(20)   Navrotsky, A. Thermodynamics of Formation of Some Compounds with the Pseudobrookite Structure and of the $FeTi_2O_5$-Ti_3O_5 Solid Solution Series. *Am. Mineral.* **1975**, *60* (3–4), 249–256

(21)   Pauling, L. VII. The Crystal Structure of Pseudobrookite. *Zeitschrift für Krist. - Cryst. Mater.* **1930**, *73* (1–6), 97–112, DOI: 10.1524/zkri.1930.73.1.97

(22)   Bueno, S.; Baudín, C. Aluminum Titanate, Structure and Properties. In *Encyclopedia of Materials: Technical Ceramics and Glasses*; Elsevier, 2021; Vol. 2–3, pp 76–92, DOI: 10.1016/B978-0-12-818542-1.00068-0

(23)   Skala, R. D.; Li, D.; Low, I. M. Diffraction, Structure and Phase Stability Studies on Aluminium Titanate. *J. Eur. Ceram. Soc.* **2009**, *29* (1), 67–75, DOI: 10.1016/j.jeurceramsoc.2008.05.037

(24)   Morosin, B.; Lynch, R. W. Structure Studies on Al_2TiO_5 at Room Temperature and at 600°C. *Acta Crystallogr. Sect. B Struct. Crystallogr. Cryst. Chem.* **1972**, *28* (4), 1040–1046, DOI: 10.1107/S0567740872003681

(25)   Kim, H. C.; Lee, K. S.; Kweon, O. S.; Aneziris, C. G.; Kim, I. J. Crack Healing, Reopening and Thermal Expansion Behavior of Al_2TiO_5 Ceramics at High Temperature. *J. Eur. Ceram. Soc.* **2007**, *27* (2–3), 1431–1434, DOI: 10.1016/j.jeurceramsoc.2006.04.024

(26)   Nagano, M.; Nagashima, S.; Maeda, H.; Kato, A. Sintering Behavior of Al_2TiO_5 Base Ceramics and Their Thermal Properties. *Ceram. Int.* **1999**, *25* (8), 681–687, DOI: 10.1016/S0272-8842(98)00083-2

(27)   Kim, I. J.; Kwak, H. S. Thermal Shock Resistance and Thermal Expansion Behaviour with Composition and Microstructure of Al_2TiO_5 Ceramics. *Can. Metall. Q.* **2000**, *39* (4), 387–396, DOI: 10.1179/cmq.2000.39.4.387

(28)   Soofi, M.; Binz, L.; W. Anderson, M. Protective Coating Composition For Molten Aluminium and Alkali Metal Environments. U.S. Patent 10233335B2, 2019

(29)   Tian, S.; Sun, K.; Cui, H.; Xie, X.; Wang, X.; Wei, N.; Wang, H.; Wang, W.; Song, X.; Yang, K. Structural Evolution and Electrochemical Corrosion Behavior of Al–Ti–O Amorphous-Nanocrystalline Composite Films Deposited by Magnetron Sputtering. *Thin Solid Films* **2019**, *692*, 137640, DOI: 10.1016/j.tsf.2019.137640

(30)   Lee, H. L.; Jeong, J. Y.; Lee, H. M. Preparation of Al_2TiO_5 from Alkoxides and the Effects of Additives on Its Properties. *J. Mater. Sci.* **1997**, *32* (21), 5687–5695, DOI: 10.1023/A:1018605431120

(31)   Low, I.-M.; Oo, Z. In Situ Diffraction Study of Self-Recovery in Aluminum Titanate. *J. Am. Ceram. Soc.* **2008**, *91* (3), 1027–1029, DOI: 10.1111/j.1551-2916.2007.02199.x

(32)   Freudenberg, B.; Lindner, H. A.; Gugel, E.; Thometzek, P. Thermomechanical Properties of

Aluminium Titanate Ceramic Between 20 and 1000° C. *Euroceramics.* **1989**, *2* (Proc. 1st ECERS Conference), 2.64-2.72, DOI: n/a

(33) Ohya, Y.; Nakagawa, Z.; Hamano, K. Crack Healing and Bending Strength of Aluminum Titanate Ceramics at High Temperature. *J. Am. Ceram. Soc.* **1988**, *71* (5), C-232-C-233, DOI: https://doi.org/10.1111/j.1151-2916.1988.tb05064.x

(34) Low, I. M.; Lawrence, D.; Jones, A.; Smith, R. I. Dynamic Analyses of the Thermal Stability of Aluminium Titanate by Time-Of-Flight Neutron Diffraction; 2008; pp 303–310, DOI: 10.1002/9780470291283.ch32

(35) Ohya, Y.; Kawauchi, Y.; Ban, T. Cation Distribution of Pseudobrookite-Type Titanates and Their Phase Stability. *J. Ceram. Soc. Japan* **2017**, *125* (9), 695–700, DOI: 10.2109/jcersj2.17086

(36) Epicier, T.; Thomas, G.; Wohlfromm, H.; Moya, J. S. High Resolution Electron Microscopy Study of the Cationic Disorder in Al2TiO5. *J. Mater. Res.* **1991**, *6* (1), 138–145, DOI: 10.1557/JMR.1991.0138

(37) Dondi, M.; Lyubenova, T. S.; Carda, J. B.; Ocaña, M. M-Doped Al2TiO5 (M=Cr, Mn, Co) Solid Solutions and Their Use as Ceramic Pigments. *J. Am. Ceram. Soc.* **2009**, *92* (9), 1972–1980, DOI: 10.1111/j.1551-2916.2009.03172.x

(38) Wu, J.; Ma, X.; Hu, X.; Yan, L.; Hou, F.; Liu, J.; Guo, A. New Class of High-Entropy Pseudobrookite Titanate with Excellent Thermal Stability, Low Thermal Expansion Coefficient, and Low Thermal Conductivity. *J. Adv. Ceram.* **2022**, *11* (10), 1654–1670, DOI: 10.1007/s40145-022-0638-7

(39) Freudenberg, B.; Mocellin, A. Aluminum Titanate Formation by Solid-State Reaction of Coarse Al2O3 and TiO2 Powders. *J. Am. Ceram. Soc.* **1988**, *71* (1), 22–28, DOI: 10.1111/j.1151-2916.1988.tb05755.x

(40) Bonhomme-Coury, L.; Lequeux, N.; Mussotte, S.; Boch, P. Preparation of Al2TiO5-ZrO2 Mixed Powders via Sol-Gel Process. *J. Sol-Gel Sci. Technol.* **1994**, *2* (1–3), 371–375, DOI: 10.1007/BF00486273

(41) Andrianainarivelo, M.; Corriu, R. J. P.; Leclercq, D.; Mutin, P. H.; Vioux, A. Nonhydrolytic Sol−Gel Process: Aluminum Titanate Gels. *Chem. Mater.* **1997**, *9* (5), 1098–1102, DOI: 10.1021/cm960405b

(42) Innocenzi, P.; Martucci, A.; Armelao, L.; Licoccia, S.; Di Vona, M. L.; Traversa, E. Sol−Gel Synthesis of β-Al2TiO5 Thin Films at Low Temperature. *Chem. Mater.* **2000**, *12* (2), 517–524, DOI: 10.1021/cm991134i

(43) Leinen, D.; Lassaletta, G.; Fernández, A.; Caballero, A.; González-Elipe, A. R.; Martín, J. M.; Vacher, B. Ion Beam Induced Chemical Vapor Deposition Procedure for the Preparation of Oxide Thin Films. II. Preparation and Characterization of AlxTiyOz Thin Films. *J. Vac. Sci. Technol. A Vacuum, Surfaces, Film.* **1996**, *14* (5), 2842–2848, DOI: 10.1116/1.580233

(44) Buscaglia, V.; Battilana, G.; Leoni, M.; Nanni, P. Decomposition of Al2TiO5-MgTi2O5 Solid Solutions: A Thermodynamic Approach. *J. Mater. Sci.* **1996**, *31* (19), 5009–5016, DOI: 10.1007/BF00355899

(45) Buscaglia, V.; Nanni, P. Decomposition of Al2TiO5 and Al2(1-x)MgxTi(1+x)O5 Ceramics. *J. Am. Ceram. Soc.* **2005**, *81* (10), 2645–2653, DOI: 10.1111/j.1151-2916.1998.tb02672.x

(46) Djambazov, S.; Lepkova, D.; Ivanov, I. A Study of the Stabilization of Aluminium Titanate. *J. Mater. Sci.* **1994**, *29* (9), 2521–2525, DOI: 10.1007/BF00363449

(47) Low, I. M.; Lawrence, D.; Smith, R. I. Factors Controlling the Thermal Stability of Aluminum Titanate Ceramics in Vacuum. *J. Am. Ceram. Soc.* **2005**, *88* (10), 2957–2961, DOI: 10.1111/j.1551-2916.2005.00518.x

(48) Lang, S. M.; Fillmore, C. L.; Maxwell, L. H. The System Beryllia-Alumina-Titania: Phase Relations and General Physical Properties of Three-Component Porcelains. *J. Res. Natl. Bur. Stand. (1934).* **1952**, *48* (4), 298, DOI: 10.6028/jres.048.038

(49)   Norberg, S. T.; Hoffmann, S.; Yoshimura, M.; Ishizawa, N. Al6Ti2O13 , a New Phase in the Al2O3 –TiO2 System. *Acta Crystallogr. Sect. C Cryst. Struct. Commun.* **2005**, *61* (3), i35–i38, DOI: 10.1107/S0108270105002532

(50)   Hoffmann, S.; Norberg, S. T.; Yoshimura, M. Structural Models for Intergrowth Structures in the Phase System Al2O3–TiO2. *J. Solid State Chem.* **2005**, *178* (9), 2897–2906, DOI: 10.1016/j.jssc.2005.07.001

(51)   Ritala, M.; Niinisto, J.; Krumdieck, S.; Chalker, P.; Aspinall, H.; Pemble, M. E.; Gladfelter, W. L.; Leese, B.; Fischer, R. A.; Parala, H.; Kanjolia, R.; Dupuis, R. D.; Alexandrov, S. E.; Irvine, S. J. C.; Palgrave, R.; Parkin, I. P.; Jones, A. C.; Hitchman, M. L. *Chemical Vapour Deposition*; Jones, A. C., Hitchman, M. L., Eds.; Royal Society of Chemistry: Cambridge, 2008, DOI: 10.1039/9781847558794

(52)   O. Pierson, H. *Handbook of Chemical Vapor Deposition (CVD) - Principles, Technology, and Applications*, Second Edi.; William Andrew Publishing, LLC: New York, 1999

(53)   Xu, Y.; Yan, X.-T. *Chemical Vapour Deposition - An Integrated Engineering Design for Advanced Materials*; Engineering Materials and Processes; Springer London: London, 2010, DOI: 10.1007/978-1-84882-894-0

(54)   Dobkin, D. M.; Zuraw, M. K. *Principles of Chemical Vapor Deposition*; Springer Netherlands: Dordrecht, 2003, DOI: 10.1007/978-94-017-0369-7

(55)   Argon ALPHAGAZ™ Specification Sheet - Air Liquide https://specialty.airliquide.co.uk/product/argon-alphagaz-2-50/?category=pures

(56)   O'Brien, P.; Pickett, N. L.; Otway, D. J. Developments in CVD Delivery Systems: A Chemist's Perspective on the Chemical and Physical Interactions Between Precursors. *Chem. Vap. Depos.* **2002**, *8* (6), 237–249, DOI: 10.1002/1521-3862(20021203)8:6<237::AID-CVDE237>3.0.CO;2-O

(57)   Mehrotra, R. C. Synthesis and Reactions of Metal Alkoxides. *J. Non. Cryst. Solids* **1988**, *100* (1–3), 1–15, DOI: 10.1016/0022-3093(88)90003-8

(58)   Kuzminykh, Y.; Dabirian, A.; Reinke, M. High Vacuum Chemical Vapour Deposition of Oxides:: A Review of Technique Development and Precursor Selection. *Surf. Coatings Technol.* **2013**, *230*, 13–21, DOI: 10.1016/J.SURFCOAT.2013.06.059

(59)   Devi, A. "Old Chemistries" for New Applications: Perspectives for Development of Precursors for MOCVD and ALD Applications. *Coord. Chem. Rev.* **2013**, *257* (23–24), 3332–3384, DOI: 10.1016/j.ccr.2013.07.025

(60)   Mishra, S.; Daniele, S. Molecular Engineering of Metal Alkoxides for Solution Phase Synthesis of High-Tech Metal Oxide Nanomaterials. *Chem. – A Eur. J.* **2020**, *26* (42), 9292–9303, DOI: 10.1002/chem.202000534

(61)   Bradley, D. C. Metal Alkoxides as Precursors for Electronic and Ceramic Materials. *Chem. Rev.* **1989**, *89* (6), 1317–1322, DOI: 10.1021/cr00096a004

(62)   Knapp, C. E.; Carmalt, C. J. Solution Based CVD of Main Group Materials. *Chem. Soc. Rev.* **2016**, *45* (4), 1036–1064, DOI: 10.1039/c5cs00651a

(63)   Folting, K.; Streib, W. E.; Caulton, K. G.; Poncelet, O.; Hubert-Pfalzgraf, L. G. Characterization of Aluminium Isopropoxide and Aluminosiloxanes. *Polyhedron* **1991**, *10* (14), 1639–1646, DOI: 10.1016/S0277-5387(00)83775-4

(64)   Turova, N. Y.; Kozunov, V. A.; Yanovskii, A. I.; Bokii, N. G.; Struchkov, Y. T.; Tarnopol'skii, B. L. Physico-Chemical and Structural Investigation of Aluminium Isopropoxide. *J. Inorg. Nucl. Chem.* **1979**, *41* (1), 5–11, DOI: 10.1016/0022-1902(79)80384-X

(65)   Mehrotra, R. C.; Rai, A. K. Aluminium Alkoxides, β-Diketonates and Carboxylates. *Polyhedron* **1991**, *10* (17), 1967–1994, DOI: 10.1016/S0277-5387(00)86025-8

(66)   Sovar, M.-M.; Samélor, D.; Gleizes, A. N.; Vahlas, C. Aluminium Tri-Iso-Propoxide: Shelf Life, Transport Properties, and Decomposition Kinetics for the Low Temperature Processing of Aluminium Oxide-Based Coatings. *Surf. Coatings Technol.* **2007**, *201* (22–23),

9159–9162, DOI: 10.1016/j.surfcoat.2007.04.063

(67)   Vioux, A. Nonhydrolytic Sol-Gel Routes to Oxides. *Chem. Mater.* **1997**, *9* (11), 2292–2299, DOI: 10.1021/cm970322a

(68)   Gellman, A. J.; Dai, Q. Mechanism of β-Hydride Elimination in Adsorbed Alkoxides. *J. Am. Chem. Soc.* **1993**, *115* (2), 714–722, DOI: 10.1021/ja00055a048

(69)   Hofman, R.; Westheim, J. G. F.; Haanappel, V. A. C.; Fransen, T.; Gellings, P. J. The Pyrolytic Decomposition of Metal Alkoxides(Di-Acetoxy-Di-t-Butoxy-Silane, DADBS) during Chemical Vapour Deposition of Thin Oxide Films. *Thermochim. Acta* **1993**, *215* (C), 329–335, DOI: 10.1016/0040-6031(93)80109-N

(70)   Anderson, V. R.; Cavanagh, A. S.; Abdulagatov, A. I.; Gibbs, Z. M.; George, S. M. Waterless TiO2 Atomic Layer Deposition Using Titanium Tetrachloride and Titanium Tetraisopropoxide. *J. Vac. Sci. Technol. A Vacuum, Surfaces, Film.* **2014**, *32* (1), 01A114, DOI: 10.1116/1.4839015

(71)   Hou, F.; Martin, J. D.; Dill, E. D.; Folmer, J. C. W.; Josey, A. A. Transition Zone Theory of Crystal Growth and Viscosity. *Chem. Mater.* **2015**, *27* (9), 115, DOI: 10.1021/acs.chemmater.5b00956

(72)   Oyelaran, O.; Novet, T.; Johnson, C. D.; Johnson, D. C. Controlling Solid-State Reaction Pathways: Composition Dependence in the Nucleation Energy of InSe. *J. Am. Chem. Soc.* **1996**, *118* (10), 2422–2426, DOI: 10.1021/ja953560k

(73)   Perepezko, J. H.; Uttormark, M. J. Nucleation-Controlled Solidification Kinetics. *Metall. Mater. Trans. A* **1996**, *27* (3), 533–547, DOI: 10.1007/BF02648944

(74)   Kalikmanov, V. I. *Nucleation Theory*, 1st ed.; Lecture Notes in Physics; Springer Netherlands: Dordrecht, 2013; Vol. 860, DOI: 10.1007/978-90-481-3643-8

(75)   Engel, T.; Reid, P. *Thermodynamics, Statistical Thermodynamics, and Kinetics*, 3rd Editio.; Pearson, 2019

(76)   Cantor, B. *The Equations of Materials*; Oxford University Press: Oxford, 2020, DOI: 10.1093/oso/9780198851875.001.0001

(77)   Thieme, K.; Avramov, I.; Rüssel, C. The Mechanism of Deceleration of Nucleation and Crystal Growth by the Small Addition of Transition Metals to Lithium Disilicate Glasses. *Sci. Rep.* **2016**, *6* (1), 25451, DOI: 10.1038/srep25451

(78)   Abyzov, A. S.; Fokin, V. M.; Rodrigues, A. M.; Zanotto, E. D.; Schmelzer, J. W. P. The Effect of Elastic Stresses on the Thermodynamic Barrier for Crystal Nucleation. *J. Non. Cryst. Solids* **2016**, *432 B*, 325–333, DOI: 10.1016/j.jnoncrysol.2015.10.029

(79)   Martinková, S.; Shánělová, J.; Barták, J.; Málek, J. Transient Nucleation in Ge-Sb-S Thin Films. *Cryst. Growth Des.* **2018**, *18* (8), 4562–4570, DOI: 10.1021/acs.cgd.8b00555

(80)   Erdemir, D.; Lee, A. Y.; Myerson, A. S. Nucleation of Crystals from Solution: Classical and Two-Step Models. *Acc. Chem. Res.* **2009**, *42* (5), 621–629, DOI: 10.1021/ar800217x

(81)   Graeser, K. A.; Patterson, J. E.; Zeitler, J. A.; Rades, T. The Role of Configurational Entropy in Amorphous Systems. *Pharmaceutics* **2010**, *2* (2), 224–244, DOI: 10.3390/pharmaceutics2020224

(82)   Kelton, K. F.; Greer, A. L.; Thompson, C. V. Transient Nucleation in Condensed Systems. *J. Chem. Phys.* **1983**, *79* (12), 6261–6276, DOI: 10.1063/1.445731

(83)   Breu, J.; Seidl, W.; Huttner, D.; Kraus, F. Nucleation-Controlled Crystallization of a New, Spontaneously Resolved Solvate of [Ru(Bpy)3](PF6)2 and Its Desolvation Reaction. *Chem. - A Eur. J.* **2002**, *8* (19), 4454–4460, DOI: 10.1002/1521-3765(20021004)8:19<4454::AID-CHEM4454>3.0.CO;2-W

(84)   Xu, S.; Hou, Z.; Chuai, X.; Wang, Y. Overview of Secondary Nucleation: From Fundamentals to Application. *Ind. Eng. Chem. Res.* **2020**, *59* (41), 18335–18356, DOI: 10.1021/acs.iecr.0c03304

(85)   Hren, A. G.; Hren, J. J. *Elements of Physical Metallurgy*, Third Edit.; Cohen, M., Ed.; Addison-

Welsey Publishing: Reading, Massachusetts, 1974

(86)   Yu, L.; Reutzel-Edens, S. M. CRYSTALLIZATION | Basic Principles. In *Encyclopedia of Food Sciences and Nutrition*; Caballero, B. B. T.-E. of F. S. and N. (Second E., Ed.; Elsevier: Oxford, 2003; pp 1697–1702, DOI: 10.1016/B0-12-227055-X/00313-8

(87)   Avrami, M. Granulation, Phase Change, and Microstructure Kinetics of Phase Change. III. *J. Chem. Phys.* **1941**, *9* (2), 177–184, DOI: 10.1063/1.1750872

(88)   Avrami, M. Kinetics of Phase Change. I: General Theory. *J. Chem. Phys.* **1939**, *7* (12), 1103–1112, DOI: 10.1063/1.1750380

(89)   Barmak, K. A Commentary on: "Reaction Kinetics in Processes of Nucleation and Growth"*. *Metall. Mater. Trans. B* **2018**, *49* (6), 3616–3680, DOI: 10.1007/s11663-010-9421-1

(90)   Buchwitz, M.; Adlwarth-Dieball, R.; Ryder, P. L. Kinetics of the Crystallization of Amorphous Ti2Ni. *Acta Metall. Mater.* **1993**, *41* (6), 1885–1892, DOI: 10.1016/0956-7151(93)90208-A

(91)   Wang, X.; Vlassak, J. J. Crystallization Kinetics of Amorphous NiTi Shape Memory Alloy Thin Films. *Scr. Mater.* **2006**, *54* (5), 925–930, DOI: 10.1016/j.scriptamat.2005.10.061

(92)   Wang, X.; Rein, M.; Vlassak, J. J. Crystallization Kinetics of Amorphous Equiatomic NiTi Thin Films: Effect of Film Thickness. *J. Appl. Phys.* **2008**, *103* (2), 023501, DOI: 10.1063/1.2829811

(93)   Thompson, C. V.; Spaepen, F. Homogeneous Crystal Nucleation in Binary Metallic Melts. *Acta Metall.* **1983**, *31* (12), 2021–2027, DOI: 10.1016/0001-6160(83)90019-6

(94)   Perepezko, J. H. Nucleation-Controlled Reactions and Metastable Structures. *Prog. Mater. Sci.* **2004**, *49* (3–4), 263–284, DOI: 10.1016/S0079-6425(03)00028-8

(95)   Karthika, S.; Radhakrishnan, T. K.; Kalaichelvi, P. A Review of Classical and Nonclassical Nucleation Theories. *Cryst. Growth Des.* **2016**, *16* (11), 6663–6681, DOI: 10.1021/acs.cgd.6b00794

(96)   Mehta, N.; Kumar, A. Some New Observations on Activation Energy of Crystal Growth for Thermally Activated Crystallization. *J. Phys. Chem. B* **2016**, *120* (6), 1175–1182, DOI: 10.1021/acs.jpcb.5b10441

(97)   Spinella, C.; Lombardo, S.; Priolo, F. Crystal Grain Nucleation in Amorphous Silicon. *J. Appl. Phys.* **1998**, *84* (10), 5383–5414, DOI: 10.1063/1.368873

(98)   Jackson, K. A.; Uhlmann, D. R.; Hunt, J. D. On the Nature of Crystal Growth from the Melt. *J. Cryst. Growth* **1967**, *1* (1), 1–36, DOI: 10.1016/0022-0248(67)90003-6

(99)   Avrami, M. Kinetics of Phase Change. II Transformation-Time Relations for Random Distribution of Nuclei. *J. Chem. Phys.* **1940**, *8* (2), 212–224, DOI: 10.1063/1.1750631

(100)   Dill, E. D.; Folmer, J. C. W.; Martin, J. D. Crystal Growth Simulations to Establish Physically Relevant Kinetic Parameters from the Empirical Kolmogorov-Johnson-Mehl-Avrami Model. *Chem. Mater.* **2013**, *25* (20), 3941–3951, DOI: 10.1021/cm402751x

(101)   Dill, E. D.; Josey, A. A.; Folmer, J. C. W.; Hou, F.; Martin, J. D. Experimental Determination of the Crystallization Phase-Boundary Velocity in the Halozeotype CZX-1. *Chem. Mater.* **2013**, *25* (20), 3932–3940, DOI: 10.1021/cm402745e

(102)   Blank-Bewersdorff, M.; Köster, U. Transient Nucleation in Zirconium-Based Metallic Glasses. *Mater. Sci. Eng.* **1988**, *97*, 313–316, DOI: 10.1016/0025-5416(88)90063-8

(103)   Sinha, I.; Mandal, R. K. Avrami Exponent under Transient and Heterogeneous Nucleation Transformation Conditions. *J. Non. Cryst. Solids* **2011**, *357* (3), 919–925, DOI: 10.1016/j.jnoncrysol.2010.11.005

(104)   Ye, F.; Lu, K. Crystallization Kinetics of Al-La-Ni Amorphous Alloy. *J. Non. Cryst. Solids* **2000**, *262* (1), 228–235, DOI: 10.1016/S0022-3093(99)00660-2

(105)   Vasiliev, S. V.; Tkatch, V. I.; Aronin, A. S.; Kovalenko, O. V.; Rassolov, S. G. Analysis of the Transient Behavior of Nucleation in the Fe40Ni40P14B6 Glass. *J. Alloys Compd.* **2018**, *744*, 141–145, DOI: 10.1016/j.jallcom.2018.02.059

(106)   Fokin, V. M.; Zanotto, E. D. Crystal Nucleation in Silicate Glasses: The Temperature and Size Dependence of Crystal/Liquid Surface Energy. *J. Non. Cryst. Solids* **2000**, *265* (1–2), 105–112, DOI: 10.1016/S0022-3093(99)00877-7

(107)   Lodesani, F.; Tavanti, F.; Menziani, M. C.; Maeda, K.; Takato, Y.; Urata, S.; Pedone, A. Exploring the Crystallization Path of Lithium Disilicate through Metadynamics Simulations. *Phys. Rev. Mater.* **2021**, 5 (7), 075602, DOI: 10.1103/PhysRevMaterials.5.075602

(108)   Anderson, M. W.; Bennett, M.; Cedeno, R.; Cölfen, H.; Cox, S. J.; Cruz-Cabeza, A. J.; De Yoreo, J. J.; Drummond-Brydson, R.; Dudek, M. K.; Fichthorn, K. A.; Finney, A. R.; Ford, I. Understanding Crystal Nucleation Mechanisms: Where Do We Stand? General Discussion. *Faraday Discuss.* **2022**, *235*, 219–272, DOI: 10.1039/D2FD90021A

(109)   Birkholz, M. *Thin Film Analysis by X-Ray Scattering*; 2006, DOI: 10.1002/3527607595

(110)   West, A. R. *Basic Solid State Chemistry*, Second Edi.; John Wiley & Sons, Inc.: Hoboken, NJ, USA, 1999

(111)   Leng, Y. *Materials Characterization: Introduction to Microscopic and Spectroscopic Methods*, First Edit.; Wiley: Singapore, 2009

(112)   Hammond, C. *The Basics of Crystallography and Diffraction*; Oxford University PressOxford, 2015, DOI: 10.1093/acprof:oso/9780198738671.001.0001

(113)   Rietveld, H. M. A Profile Refinement Method for Nuclear and Magnetic Structures. *J. Appl. Crystallogr.* **1969**, *2* (2), 65–71, DOI: 10.1107/S0021889869006558

(114)   Le Bail, A. Whole Powder Pattern Decomposition Methods and Applications: A Retrospection. *Powder Diffr.* **2005**, *20* (4), 316–326, DOI: 10.1154/1.2135315

(115)   Cockcroft, J. K. Whole Pattern Fitting - I. Pawley Method http://pd.chem.ucl.ac.uk/pdnn/solve1/pawley.htm

(116)   Pawley, G. S. Unit-Cell Refinement from Powder Diffraction Scans. *J. Appl. Crystallogr.* **1981**, *14* (6), 357–361, DOI: 10.1107/S0021889881009618

(117)   Moulder, J. F.; Stickle, W. F.; Sobol, P. E.; Bomben, K. D. *Handbook of X-Ray Photoelectron Spectroscopy: A Reference Book of Standard Spectra for Identification and Interpretation of XPS Data*; Jill Chastain, Ed.; Perkin-Elmer Corporation: Minnesota, 1992

(118)   Vandenabeele, P. *Practical Raman Spectroscopy – An Introduction*; John Wiley & Sons, Ltd: Chichester, 2013, DOI: 10.1002/9781119961284

(119)   Fultz, B.; Howe, J. *Transmission Electron Microscopy and Diffractometry of Materials*, Fourth Edi.; Rhodes, W. T., Ed.; Springer International Publishing, 2013

(120)   Nastasi, M.; Mayer, J. W.; Wang, Y. *Ion Beam Analysis - Fundamentals and Applications*, 1st Editio.; CRC Press: Boca Raton, 2015, DOI: 10.1201/b17310

(121)   Jeynes, C.; Colaux, J. L. Thin Film Depth Profiling by Ion Beam Analysis. *Analyst* **2016**, *141* (21), 5944–5985, DOI: 10.1039/C6AN01167E

(122)   Schmidt, B.; Wetzig, K. *Ion Beams in Materials Processing and Analysis*; Springer Vienna: Vienna, 2013; Vol. 192, DOI: 10.1007/978-3-211-99356-9

(123)   Zhou, T.; Hu, J. Mass Production and Photocatalytic Activity of Highly Crystalline Metastable Single-Phase $Bi_{20}TiO_{32}$ Nanosheets. *Environ. Sci. Technol.* **2010**, *44* (22), 8698–8703, DOI: 10.1021/es1019959

(124)   Dixon, D. A. Density Functional Theory; White, W. M., Ed.; Springer International Publishing: Cham, 2016; pp 1–7, DOI: 10.1007/978-3-319-39193-9_17-1

(125)   Sholl, D. S.; Steckel, J. A. *Density Functional Theory*; John Wiley & Sons, Inc.: Hoboken, NJ, USA, 2009, DOI: 10.1002/9780470447710

(126)   Munakata, T. Density Functional Theory of Liquids, Some Extensions and Applications. *J. Mol. Liq.* **2001**, *90* (1–3), 205–214, DOI: 10.1016/S0167-7322(01)00123-4

(127)   von Barth, U. Basic Density-Functional Theory an Overview. *Phys. Scr.* **2004**, *T109* (T109), 9, DOI: 10.1238/Physica.Topical.109a00009

(128)   Hohenberg, P.; Kohn, W. Inhomogeneous Electron Gas. *Phys. Rev.* **1964**, *136* (3B), B864–

B871, DOI: 10.1103/PhysRev.136.B864

(129) Kohn, W.; Sham, L. J. Self-Consistent Equations Including Exchange and Correlation Effects. *Phys. Rev.* **1965**, *140* (4A), A1133–A1138, DOI: 10.1103/PhysRev.140.A1133

(130) Webb, S. .; Alford, N. M.; Penn, S. .; Templeton, A.; Wang, X. The Use of Raman Spectroscopy for Characterisation of Ceramic Dielectrics. *Nondestruct. Test. Eval.* **2001**, *17* (4–5), 205–212, DOI: 10.1080/10589750108953111

(131) Reinke, M.; Kuzminykh, Y.; Hoffmann, P. Surface Kinetics of Titanium Isopropoxide in High Vacuum Chemical Vapor Deposition. *J. Phys. Chem. C* **2015**, *119* (50), 27965–27971, DOI: 10.1021/acs.jpcc.5b07177

(132) Hofman, R.; Morssinkhof, R. W. J.; Fransen, T.; Westheim, J. G. F.; Gellings, P. J. Thin Alumina and Silica Films by Chemical Vapor Deposition (CVD). *Mater. Manuf. Process.* **1993**, *8* (3), 315–329, DOI: 10.1080/10426919308934836

(133) Schmidt, B. W.; Sweet, W. J.; Bierschenk, E. J.; Gren, C. K.; Hanusa, T. P.; Rogers, B. R. Metal-Organic Chemical Vapor Deposition of Aluminum Oxide Thin Films via Pyrolysis of Dimethylaluminum Isopropoxide. *J. Vac. Sci. Technol. A Vacuum, Surfaces, Film.* **2010**, *28* (2), 238–243, DOI: 10.1116/1.3294718

(134) Acosta, S.; Corriu, R. J. P.; Leclercq, D.; Lefèvre, P.; Mutin, P. H.; Vioux, A. Preparation of Alumina Gels by a Non-Hydrolytic Sol-Gel Processing Method. *J. Non. Cryst. Solids* **1994**, *170* (3), 234–242, DOI: 10.1016/0022-3093(94)90052-3

(135) Taylor, C. J.; Gilmer, D. C.; Colombo, D. G.; Wilk, G. D.; Campbell, S. A.; Roberts, J.; Gladfelter, W. L. Does Chemistry Really Matter in the Chemical Vapor Deposition of Titanium Dioxide? Precursor and Kinetic Effects on the Microstructure of Polycrystalline Films. *J. Am. Chem. Soc.* **1999**, *121* (22), 5220–5229, DOI: 10.1021/ja984446f

(136) Joubert, J.-M.; Černý, R.; Latroche, M.; Leroy, E.; Guénée, L.; Percheron-Guégan, A.; Yvon, K. A Structural Study of the Homogeneity Domain of LaNi5. *J. Solid State Chem.* **2002**, *166* (1), 1–6, DOI: 10.1006/jssc.2001.9499

(137) Sizov, F. F.; Plyatsko, S. V. Homogeneity Range and Nonstoichiometric Defects in IV–VI Narrow-Gap Semiconductors. *J. Cryst. Growth* **1988**, *92* (3–4), 571–580, DOI: 10.1016/0022-0248(88)90042-5

(138) Rempel, A. A.; Gusev, A. I. Preparation of Disordered and Ordered Highly Nonstoichiometric Carbides and Evaluation of Their Homogeneity. *Phys. Solid State* **2000**, *42* (7), 1280–1286, DOI: 10.1134/1.1131377

(139) Kim, Y.-M.; He, J.; Biegalski, M. D.; Ambaye, H.; Lauter, V.; Christen, H. M.; Pantelides, S. T.; Pennycook, S. J.; Kalinin, S. V.; Borisevich, A. Y. Probing Oxygen Vacancy Concentration and Homogeneity in Solid-Oxide Fuel-Cell Cathode Materials on the Subunit-Cell Level. *Nat. Mater.* **2012**, *11* (10), 888–894, DOI: 10.1038/nmat3393

(140) Norberg, S. T.; Ishizawa, N.; Hoffmann, S.; Yoshimura, M. Redetermination of β-Al2TiO5 Obtained by Melt Casting. *Acta Crystallogr. Sect. E Struct. Reports Online* **2005**, *61* (8), i160–i162, DOI: 10.1107/S1600536805021331

(141) Martinolich, A. J.; Neilson, J. R. Toward Reaction-by-Design: Achieving Kinetic Control of Solid State Chemistry with Metathesis. *Chem. Mater.* **2017**, *29* (2), 479–489, DOI: 10.1021/acs.chemmater.6b04861

(142) Hu, W.; Li, L.; Li, G.; Liu, Y.; Withers, R. L. Atomic-Scale Control of TiO6 Octahedra through Solution Chemistry towards Giant Dielectric Response. *Sci. Rep.* **2014**, *4*, 1–9, DOI: 10.1038/srep06582

(143) McMillan, P.; Piriou, B.; Navrotsky, A. A Raman Spectroscopic Study of Glasses along the Joins Silica-Calcium Aluminate, Silica-Sodium Aluminate, and Silica-Potassium Aluminate. *Geochim. Cosmochim. Acta* **1982**, *46* (11), 2021–2037, DOI: 10.1016/0016-7037(82)90182-X

(144) McMillan, P.; Piriou, B. Raman Spectroscopic Studies of Silicate and Related Glass

124

Structure: A Review. *Bull. Mineral.* **1983**, *106* (1–2), 57–75, DOI: 10.3406/bulmi.1983.7668

(145) Novikov, A. N.; Neuville, D. R.; Hennet, L.; Gueguen, Y.; Thiaudière, D.; Charpentier, T.; Florian, P. Al and Sr Environment in Tectosilicate Glasses and Melts: Viscosity, Raman and NMR Investigation. *Chem. Geol.* **2017**, *461*, 115–127, DOI: 10.1016/j.chemgeo.2016.11.023

(146) Mysen, B. O.; Virgo, D.; Kushiro, I. The Structural Role of Aluminum in Silicate Melts-a Raman Spectroscopic Study at 1 Atmosphere. *Am. Mineral.* **1981**, *66* (7–8), 678–701, DOI: Unavailable

(147) Noh, M.; Johnson, C. D.; Hornbostel, M. D.; Thiel, J.; Johnson, D. C. Control of Reaction Pathway and the Nanostructure of Final Products through the Design of Modulated Elemental Reactants. *Chem. Mater.* **1996**, *8* (8), 1625–1635, DOI: 10.1021/cm9601087

(148) Novet, T.; Johnson, D. C. New Synthetic Approach to Extended Solids: Selective Synthesis of Iron Silicides via the Amorphous State. *J. Am. Chem. Soc.* **1991**, *113* (9), 3398–3403, DOI: 10.1021/ja00009a027

(149) Sariel, J.; Chen, H.; Jongste, J. F.; Radelaar, S. In Situ X-Ray Diffraction Study of the Formation of TiSi2-C49 Phase from Ti-Si Multilayers on Si(100). *Mater. Chem. Phys.* **1995**, *40* (2), 82–86, DOI: 10.1016/0254-0584(94)01457-R

(150) Zhuang, Y. X.; Jiang, J. Z.; Lin, Z. G.; Mezouar, M.; Crichton, W.; Inoue, A. Evidence of Eutectic Crystallization and Transient Nucleation in Al89La6Ni5 Amorphous Alloy. *Appl. Phys. Lett.* **2001**, *79* (6), 743–745, DOI: 10.1063/1.1389506

(151) Neu, J. C.; Bonilla, L. L.; Carpio, A. Igniting Homogeneous Nucleation. *Phys. Rev. E - Stat. Nonlinear, Soft Matter Phys.* **2005**, *71* (2), DOI: 10.1103/PhysRevE.71.021601

(152) Lu, K.; Wang, J. T. Activation Energies for Crystal Nucleation and Growth in Amorphous Alloys. *Mater. Sci. Eng. A* **1991**, *133* (C), 500–503, DOI: 10.1016/0921-5093(91)90119-8

(153) Mandal, S.; Lee, D. E.; Park, T. Isothermal Crystallization Kinetics of (Cu60Zr25Ti15)99.3Nb0.7 Bulk Metallic Glass. *Sci. Rep.* **2020**, *10* (1), 1–10, DOI: 10.1038/s41598-020-67390-y

(154) Mao, Z.; Campbell, C. T. Apparent Activation Energies in Complex Reaction Mechanisms: A Simple Relationship via Degrees of Rate Control. *ACS Catal.* **2019**, *9* (10), 9465–9473, DOI: 10.1021/acscatal.9b02761

(155) Lu, W.; Yan, B.; Huang, W. H. Complex Primary Crystallization Kinetics of Amorphous Finemet Alloy. *J. Non. Cryst. Solids* **2005**, *351* (40–42), 3320–3324, DOI: 10.1016/j.jnoncrysol.2005.08.018

(156) Schroeder, D. V. *An Introduction to Thermal Physics*; Oxford University Press: Oxford, 2021, DOI: 10.1093/oso/9780192895547.001.0001

(157) Benenson, W.; Harris, J. W.; Stoecker, H.; Lutz, H. *Handbook of Physics*, Corr. 2nd.; Springer-Verlag: New York, 2006

(158) Smith, H. L.; Li, C. W.; Hoff, A.; Garrett, G. R.; Kim, D. S.; Yang, F. C.; Lucas, M. S.; Swan-Wood, T.; Lin, J. Y. Y.; Stone, M. B.; Abernathy, D. L.; Demetriou, M. D.; Fultz, B. Separating the Configurational and Vibrational Entropy Contributions in Metallic Glasses. *Nat. Phys.* **2017**, *13* (9), 900–905, DOI: 10.1038/nphys4142

(159) Kaußler, C.; Kieslich, G. CrystIT : Complexity and Configurational Entropy of Crystal Structures via Information Theory. *J. Appl. Crystallogr.* **2021**, *54* (1), 306–316, DOI: 10.1107/S1600576720016386

(160) Xirouchakis, D. M. Pseudobrookite-Group Oxide Solutions and Basaltic Melts. *Lithos* **2007**, *95* (1–2), 1–9, DOI: 10.1016/j.lithos.2006.07.009

(161) Martin, J. D. Particle Size Is a Primary Determinant for Sigmoidal Kinetics of Nanoparticle Formation: A "Disproof" of the Finke–Watzky (F-W) Nanoparticle Nucleation and Growth Mechanism. *Chem. Mater.* **2020**, *32* (8), 3651–3656, DOI: 10.1021/acs.chemmater.9b02839

(162)   Mattern, N.; Eckert, J.; Seidel, M.; Kühn, U.; Doyle, S.; Bächer, I. Relaxation and Crystallization of Amorphous Zr65Al7.5Cu17.5Ni10. *Mater. Sci. Eng. A* **1997**, *226–228*, 468–473, DOI: 10.1016/S0921-5093(96)10666-3

(163)   Zhang, Q.; Peng, X.; Nie, Y.; Zheng, Q.; Shangguan, J.; Zhu, C.; Bustillo, K. C.; Ercius, P.; Wang, L.; Limmer, D. T.; Zheng, H. Defect-Mediated Ripening of Core-Shell Nanostructures. *Nat. Commun.* **2022**, *13* (1), 2211, DOI: 10.1038/s41467-022-29847-8

(164)   Kwon, H. T.; Jeong, H.-K.; Lee, A. S.; An, H. S.; Lee, T.; Jang, E.; Lee, J. S.; Choi, J. Defect-Induced Ripening of Zeolitic-Imidazolate Framework ZIF-8 and Its Implication to Vapor-Phase Membrane Synthesis. *Chem. Commun.* **2016**, *52* (78), 11669–11672, DOI: 10.1039/C6CC05433A

(165)   Ji, Q.; Bi, L.; Zhang, J.; Cao, H.; Zhao, X. S. The Role of Oxygen Vacancies of ABO3perovskite Oxides in the Oxygen Reduction Reaction. *Energy Environ. Sci.* **2020**, *13* (5), 1408–1428, DOI: 10.1039/d0ee00092b

(166)   Ye, K.; Li, K.; Lu, Y.; Guo, Z.; Ni, N.; Liu, H.; Huang, Y.; Ji, H.; Wang, P. An Overview of Advanced Methods for the Characterization of Oxygen Vacancies in Materials. *TrAC - Trends Anal. Chem.* **2019**, *116*, 102–108, DOI: 10.1016/j.trac.2019.05.002

(167)   Österbacka, N.; Wiktor, J. Influence of Oxygen Vacancies on the Structure of BiVO4. *J. Phys. Chem. C* **2021**, *125* (2), 1200–1207, DOI: 10.1021/acs.jpcc.0c08751

(168)   Jang, J. H.; Kim, Y.-M.; He, Q.; Mishra, R.; Qiao, L.; Biegalski, M. D.; Lupini, A. R.; Pantelides, S. T.; Pennycook, S. J.; Kalinin, S. V.; Borisevich, A. Y. In Situ Observation of Oxygen Vacancy Dynamics and Ordering in the Epitaxial LaCoO 3 System. *ACS Nano* **2017**, *11* (7), 6942–6949, DOI: 10.1021/acsnano.7b02188

(169)   Zhang, H.; May, B. M.; Omenya, F.; Whittingham, M. S.; Cabana, J.; Zhou, G. Layered Oxide Cathodaes for Li-Ion Batteries: Oxygen Loss and Vacancy Evolution. *Chem. Mater.* **2019**, *31* (18), 7790–7798, DOI: 10.1021/acs.chemmater.9b03245

(170)   Polymorphic Transformation. *Oxford Reference*, DOI: 10.1093/oi/authority.20110803100335741

(171)   Armelao, L.; Martucci, A.; Innocenzi, P. Study of β-Al2TiO5 Thin Films by XPS. *Surf. Sci. Spectra* **2001**, *8* (1), 8–13, DOI: 10.1116/11.20001102

(172)   Innocenzi, P.; Martucci, A.; Armelao, L.; Licoccia, S.; Di Vona, M. L.; Traversa, E. Sol–Gel Synthesis of β-Al2TiO5 Thin Films at Low Temperature. *Chem. Mater.* **2000**, *12* (2), 517–524, DOI: 10.1021/cm991134i

(173)   Biesinger, M. C.; Lau, L. W. M.; Gerson, A. R.; Smart, R. S. C. Resolving Surface Chemical States in XPS Analysis of First Row Transition Metals, Oxides and Hydroxides: Sc, Ti, V, Cu and Zn. *Appl. Surf. Sci.* **2010**, *257* (3), 887–898, DOI: 10.1016/j.apsusc.2010.07.086

(174)   Biesinger, M. C.; Payne, B. P.; Hart, B. R.; Grosvenor, A. P.; McIntryre, N. S.; Lau, L. W. M.; Smart, R. S. Quantitative Chemical State XPS Analysis of First Row Transition Metals, Oxides and Hydroxides. *J. Phys. Conf. Ser.* **2008**, *100* (1), 012025, DOI: 10.1088/1742-6596/100/1/012025

(175)   Dey, U.; Chatterjee, S.; Taraphder, A. Antisite-Disorder Engineering in La-Based Oxide Heterostructures via Oxygen Vacancy Control. *Phys. Chem. Chem. Phys.* **2018**, *20* (26), 17871–17880, DOI: 10.1039/C8CP01500G

(176)   Grimes, R. W.; Pilling, J. Defect Formation in β-Al2TiO5 and Its Influence on Structure Stability. *J. Mater. Sci.* **1994**, *29* (8), 2245–2249, DOI: 10.1007/BF01154705

(177)   Zhang, M.-X.; Kelly, P. M. Crystallographic Features of Phase Transformations in Solids. *Prog. Mater. Sci.* **2009**, *54* (8), 1101–1170, DOI: 10.1016/j.pmatsci.2009.06.001

(178)   Classification of Phase Transformations. In *Phase Transformations*; Banerjee, S., Mukhopadhyay, P. B. T.-P. M. S., Eds.; Pergamon, 2007; Vol. 12, pp 87–123, DOI: 10.1016/S1470-1804(07)80055-1

(179)   Duhamel, C.; Venkataraman, S.; Scudino, S.; Eckert, J. Diffusionless Transformations; 2008;

pp 119–145, DOI: 10.1142/9789812790590_0006

(180)   Diffusion. *Encyclopaedia Britannica*

(181)   Shekhtman, V. S.; Smirnova, I. S.; Sedykh, V. D.; Shmyt'ko, I. M.; Afonikova, N. S.; Dubovitskii, A. V. Structural Hierarchy and Transformations in Crystals of the Perovskite Family. *Crystallogr. Reports* **2004**, *49* (1), 40–45, DOI: 10.1134/1.1643962

(182)   Fultz, B. Diffusionless Transformations. In *Phase Transitions in Materials*; Cambridge University Press: Cambridge, 2014; pp 355–382, DOI: 10.1017/CBO9781107589865.019

(183)   Sutter-Fella, C. M. The Value of Watching How Materials Grow: A Multimodal Case Study on Halide Perovskites. *Adv. Energy Mater.* **2021**, *11* (17), 1–7, DOI: 10.1002/aenm.202003534

(184)   Nielsen, M. H.; Aloni, S.; De Yoreo, J. J. In Situ TEM Imaging of CaCO3 Nucleation Reveals Coexistence of Direct and Indirect Pathways. *Science (80-.).* **2014**, *345* (6201), 1158–1162, DOI: 10.1126/science.1254051

(185)   Gleizes, A. N. MOCVD of Chalcogenides, Pnictides, and Heterometallic Compounds from Single-Source Molecule Precursors. *Chem. Vap. Depos.* **2000**, *6* (4), 155–173, DOI: 10.1002/1521-3862(200008)6:4<155::AID-CVDE155>3.0.CO;2-Y

(186)   Jiang, S.; Hu, T.; Gild, J.; Zhou, N.; Nie, J.; Qin, M.; Harrington, T.; Vecchio, K.; Luo, J. A New Class of High-Entropy Perovskite Oxides. *Scr. Mater.* **2018**, *142*, 116–120, DOI: 10.1016/j.scriptamat.2017.08.040

(187)   Schoeppler, V.; Stier, D.; Best, R. J.; Song, C.; Turner, J.; Savitzky, B. H.; Ophus, C.; Marcus, M. A.; Zhao, S.; Bustillo, K.; Zlotnikov, I. Crystallization by Amorphous Particle Attachment: On the Evolution of Texture. *Adv. Mater.* **2021**, *33* (37), DOI: 10.1002/adma.202101358

(188)   Jehannin, M.; Rao, A.; Cölfen, H. New Horizons of Nonclassical Crystallization. *J. Am. Chem. Soc.* **2019**, *141* (26), 10120–10136, DOI: 10.1021/jacs.9b01883

(189)   Cölfen, H.; Antonietti, M. Mesocrystals: Inorganic Superstructures Made by Highly Parallel Crystallization and Controlled Alignment. *Angew. Chemie - Int. Ed.* **2005**, *44* (35), 5576–5591, DOI: 10.1002/anie.200500496

(190)   De Yoreo, J. J.; Gilbert, P. U. P. A.; Sommerdijk, N. A. J. M.; Penn, R. L.; Whitelam, S.; Joester, D.; Zhang, H.; Rimer, J. D.; Navrotsky, A.; Banfield, J. F.; Wallace, A. F.; Michel, F. M.; Meldrum, F. C.; Cölfen, H.; Dove, P. M. Crystallization by Particle Attachment in Synthetic, Biogenic, and Geologic Environments. *Science (80-.).* **2015**, *349* (6247), DOI: 10.1126/science.aaa6760

(191)   Chandler, C. D.; Roger, C.; Hampden-Smith, M. J. Chemical Aspects of Solution Routes to Perovskite-Phase Mixed-Metal Oxides from Metal-Organic Precursors. *Chem. Rev.* **1993**, *93* (3), 1205–1241, DOI: 10.1021/cr00019a015